ISSN 1340-3745

ICRR

ICRR-Report-450-99-8

Observation of Atmospheric Neutrinos in Super-Kamiokande and a Neutrino Oscillation Analysis

Kimihiro Okumura

(March 1999)

Doctor Thesis, University of Tokyo

INSTITUTE FOR COSMIC RAY RESEARCH
UNIVERSITY OF TOKYO
3-2-1 Midori-cho, Tanashi, Tokyo 188-8502, Japan

Observation of Atmospheric Neutrinos in Super-Kamiokande and a Neutrino Oscillation Analysis

Kimihiro Okumura

February 1999

Doctor Thesis, University of Tokyo

Abstract

Experimental study on the atmospheric neutrino flux and a neutrino oscillation analysis have been made for both the sub-GeV and multi-GeV energy region using Super-Kamiokande detector.

Total exposure of the Super-Kamiokande detector amounts to 33.0 ktonyr and 4474 fully-contained (FC) events and 301 partially-contained (PC) events are observed. The μ/e ratio is found to be significantly small compared to the theoretical expectation. The ratio of data to the Monte Carlo prediction, R, is measured to be R = 0.63 $\pm$ 0.03 (stat.) $\pm$ 0.04 (syst.) for sub-GeV and R_{FC+PC} = 0.65 $\pm$ 0.05 (stat.) $\pm$ 0.08 (syst.) for multi-GeV energy region.

Additionally, the significant deficit of the upward-going events is observed for μ-like events. The up/down ratio, U/D, is measured to be U/D = $0.78\ ^{+0.05}_{-0.05}$ (stat.) $\pm$ 0.01 (syst.) for sub-GeV μ-like events and U/D = $0.53\ ^{+0.06}_{-0.05}$ (stat.) $\pm$ 0.01 (syst.) for multi-GeV μ-like events. On the other hand, the up/down ratio for e-like events is consistent with the expectation.

A 3-flavor oscillation analysis assuming one mass scale dominance are carried out and the allowed region for the oscillation parameters (Δm^2, θ_{23}, θ_{13}) is obtained. The relatively large angle for θ_{13} is allowed in the region of $9 \times 10^{-4} < \Delta m^2 < 2.5 \times 10^{-2}$ eV^2, but the pure $\nu_\mu \leftrightarrow \nu_\tau$ oscillation is also consistent with the 3-flavor oscillation within 90% confidence level (C.L.). The pure $\nu_\mu \leftrightarrow \nu_e$ oscillation is excluded with high confidence (more than 99.99% C.L.). The significant deficit of muon neutrino can be explained well by assuming the 3-flavor or pure $\nu_\mu \leftrightarrow \nu_\tau$ neutrino oscillation. We conclude that the present data give evidence for oscillation of muon neutrino.

Acknowledgment

First of all, I would like to express my sincere appreciation to my advisor, Prof. Takaaki Kajita for introducing me to experimental physics. He has supported and encouraged me on many occasion during my graduate course. He also gave me a chance to study the atmospheric neutrino and I have learned much thing under his excellent guidance. This thesis would never be completed without it.

I would like to be thankful to Prof. Y.Totsuka, the leader of the Super-Kamiokande experiment, Prof. Y.Suzuki and Prof. M.Nakahata. They gave me many proper advise about my work on various occasion.

I am grateful especially to the members of the atmospheric neutrino and proton decay analysis group. T.Hayakawa and K.Ishihara gave me many support for my work on the atmospheric neutrino. This thesis is greatly indebted to them. I was also given many useful advise and encouragement from Dr. Y.Itow, Dr. M.Miura, M.Shiozawa, Dr. S.Kasuga, J.Kameda from ICRR, Dr. K.Kaneyuki, Dr. Y.Hayato, Y.Kanaya from TIT, K.Fujita and M.Etoh from Tohoku University, L.Wai and J.George from Washington University, and the other members in U.S..

I also have to thank the other ICRR staff and graduate students, Dr. K.Inoue, Dr. Y.Fukuda, Dr. Y.Takeuchi, Dr. Y.Koshio, H.Ishino, M.Oketa, M.Ohta, N.Sakurai, S.Nakayama, S.Yamada, U.Kobayashi, K.Kobayashi and T.Takeuchi. They were willing to give me their useful knowledge which was necessary for my work and encourage me on many occasion. I am also thankful to all the Super-Kamiokande collaborators and the staff in the Kamioka Observatory for their continuous support and kind consideration.

I gratefully acknowledge the cooperation of Kamioka Mining and Smelting Company. This work was partly supported by the Japan Society of the Promotion Science.

Contents

List of Figures

List of Tables

Chapter 1

Introduction

1.1 Atmospheric neutrinos

Primary cosmic rays, like protons and nuclei, are poured continuously into the atmosphere of the Earth. As they propagate in the atmosphere, they interact with air nuclei and create secondary mesons, mostly pions and kaons. Atmospheric neutrinos are produced via the decays of these secondaries, especially the decays of charged pions and muons are dominant:

$$\begin{array}{rll} \pi^+ \rightarrow & \mu^+ & +\nu_\mu \\ & \downarrow & \\ & \mu^+ & \rightarrow e^+ + \nu_e + \bar{\nu}_\mu \\ \pi^- \rightarrow & \mu^- & +\bar{\nu}_\mu \\ & \downarrow & \\ & \mu^- & \rightarrow e^- + \bar{\nu}_e + \nu_\mu \end{array}$$

In total, two muon neutrinos and one electron neutrino are produced by the decay chain of a charged pion. The flux ratio of $(\nu_\mu + \bar{\nu}_\mu)$ to $(\nu_e + \bar{\nu}_e)$ can be expected to be 2. Actually, this expectation is correct in the energy range of $\lesssim$ 2 GeV. Above which the ratio increases up to $\sim$10 at 100 GeV, because muons arrive at the ground without decaying and the number of electron neutrino decreases. The uncertainty of the ratio is estimated to be $\leq$5 % although there is $\sim$20 % uncertainty in the measurement of primary cosmic-ray flux.

Fig 1.1 shows the energy spectra for $\nu_\mu + \bar{\nu}_\mu$ and $\nu_e + \bar{\nu}_e$, and Fig 1.2 shows the $(\nu_\mu + \bar{\nu}_\mu)/(\nu_e + \bar{\nu}_e)$, $\nu_\mu/\bar{\nu}_\mu$ and $\nu_e/\bar{\nu}_e$ ratios. Both figures show the fluxes expected at the Super-Kamiokande site.

Atmospheric neutrinos transverse the earth easily and come from all directions on the earth because neutrino has no electric charge and interacts with matter via weak interaction only. The flight length of atmospheric neutrino ranges from ~15 km to ~13000 km, and depends on the zenith angle of the arrival direction, as shown in Fig 1.3.

Fig 1.4 shows the neutrino flux $\times$ E_ν^2 as a function of the zenith angle of the neutrino arrival direction. The flux has a slight dependence on the arrival direction. At $E_\nu \lesssim 1$GeV, the neutrino flux is affected by the rigidity cutoff of the primary cosmic rays. The geomagnetic field determines the minimum energy of the primary proton. Therefore the neutrino flux is not up-down symmetric, since the geomagnetic field above Super-Kamiokande is stronger than the average. Above 2 GeV, the geomagnetic effect is negligible. The flux for horizontal direction increases due to the high probability of μ-decay for horizontal directions in the atmosphere.

1.2 Observation of atmospheric neutrinos

Detailed study of atmospheric neutrinos are initiated by the nucleon decay experiments, which aimed to detect the rare proton decay events. They were located in the deep underground to reduce cosmic ray background. But the events of the nucleon decay were supposed to be so rare that the atmospheric neutrino became a possible source of background for the nucleon decay events. Therefore the precise measurement of the atmospheric neutrino was carried out.

The atmospheric neutrino had been observed in the 1980's and early 1990's by the following experiments: Kamiokande, IMB, Soudan 2, Fréjus and Nusex. Kamiokande and IMB were a imaging water Čerenkov detector, which detect Čerenkov radiation of charged particles. The water Čerenkov detector was suited for such massive experiment because it was easy to enlarge the mass of the detector. The other experiments, Soudan 2, Fréjus and Nusex were the tracking detectors which detect the tracks of charged particles.

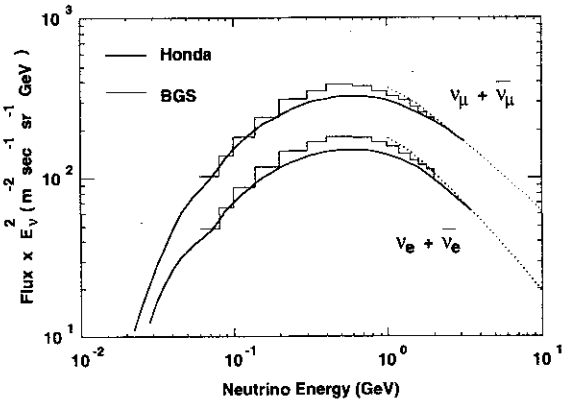

Figure 1.1: Neutrino flux $\times$ E_ν^2 at the Super-Kamiokande site as a function of neutrino energy (from Ref [30]). Honda from Ref [30], BGS from Ref [32].

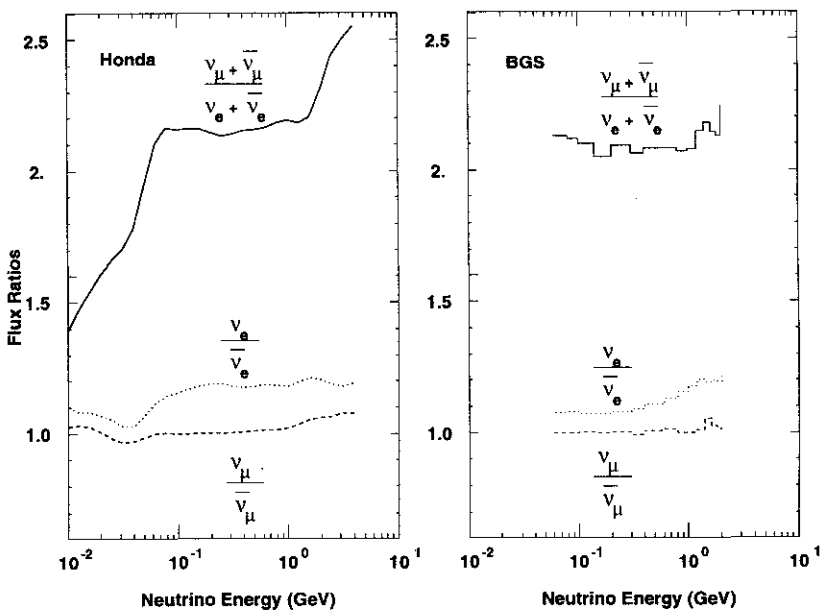

Figure 1.2: Flux ratio of neutrino species calculated for Kamioka (from Ref [30]). Honda from Ref [30], BGS from Ref [32].

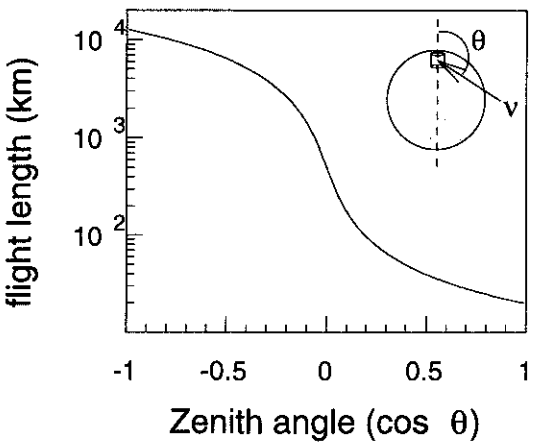

Figure 1.3: Neutrino flight length as a function of zenith angle, $\cos\theta$. The definition of zenith angle is also shown. $\cos\theta = -1$ shows upward-going and $\cos\theta = 1$ shows downward-going.

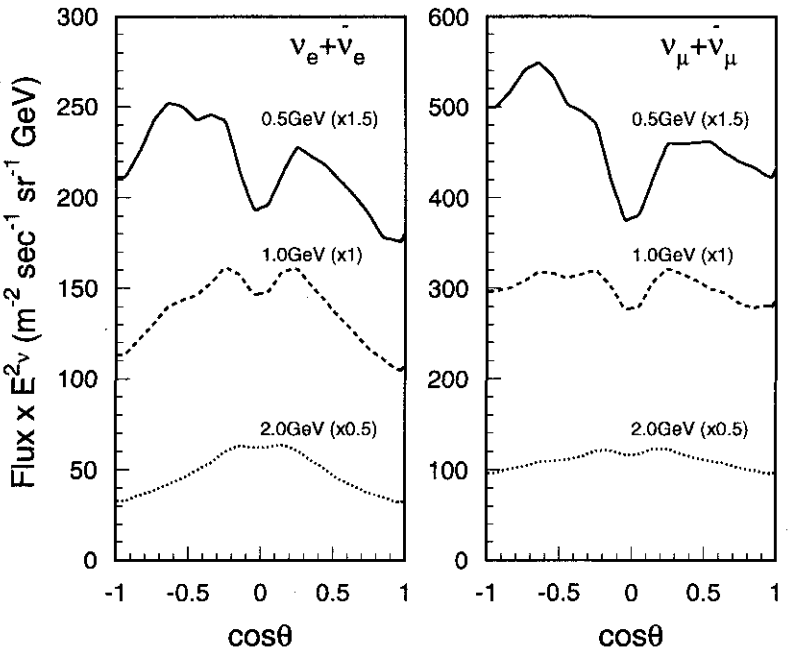

Figure 1.4: Neutrino flux $\times$ E_ν^2 for $\nu_e + \bar{\nu}_e$ and $\nu_\mu + \bar{\nu}_\mu$, at the Super-Kamiokande site. The flux calculation is based on Ref [30]. X-axis shows the zenith angle ($\cos\theta$) of neutrino arrival direction. $\cos\theta = -1$ shows upward-going and $\cos\theta = 1$ shows downward-going.

1.2.1 Kamiokande experiment

Kamiokande was an imaging water Čerenkov detector which was located in the Kamioka mine, Gifu prefecture, Japan. The average rock overburden amounts to 1000 m, which is 2700 m water equivalent (m.w.e.). The detector was the cylindrical tank, 15.5 m in diameter and 16 m in height, and contained 3000 tons of pure water. 948 20-inch photomultiplier tubes (PMTs) were instrumented in all solid angle inside the detector and the photocathod-coverage was about 20 %.

There had been three phases of experiments. Kamiokande-I started at 1983 for the detection of proton decay. From Kamiokande-II, The detector was upgraded to reduce low energy background and observe solar neutrinos. The outer detector covers the inner detector completely with 123 20-inch PMTs. The water purification system was improved to removed radioactive materials, such as ^{222}Rn, in the water. The Kamiokande-II succeeded in pushing analysis threshold down to 7 MeV and observing solar neutrinos [1], and especially it is famous for the first detection of supernova neutrinos when supernova 1987A exploded [2]. At Kamiokande-III, plastic coated aluminum reflectors were attached to all PMTs to enhance light collection and new electronic systems, which was a prototype for the Super-Kamiokande electronics, was installed. The atmospheric neutrinos were observed throughout these three phases. The normal data taking ended at 1996 and the laboratory was inherited to the KAMLAND experiment, which is aiming to detect anti electron neutrinos from nuclear reactors.

There were three types of atmospheric neutrino events observed in Kamiokande, which were fully-contained (FC) events, partially-contained (PC) events and upward-going muon (UPμ) events, as shown in fig 1.5. An event was classified as a FC event if the whole track of charged particles are contained. The particle identification was applied for the 1 Čerenkov ring FC events and tagged as μ-like or e-like, corresponding to ν_μ and ν_e induced events. An events was classified as a PC event if the vertex of event is within the inner detector and the track of a charged particle reaches the outer detector. And for a UPμ event, high energy upward-going muon, which is produced in the rock, enters the detector. These detection techniques were inherited to Super-Kamiokande.

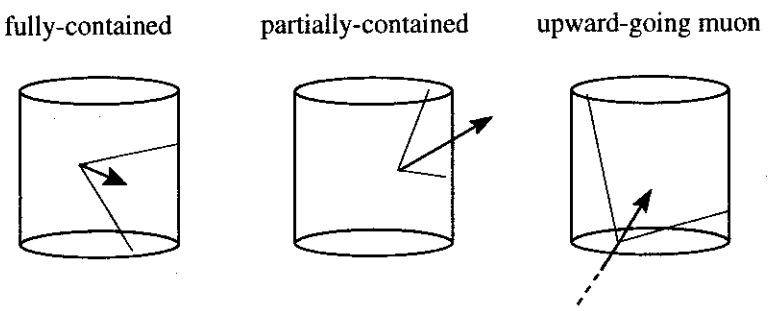

Figure 1.5: Schematic views of the fully-contained, partially-contained and upward-going muon event.

1.2.2 IMB experiment

The "Irvine-Michigan-Brookhaven" (IMB) experiment started at 1982 to detect the nucleon decay events. The detector was located at the depth of 1570 m.w.e. in the Fairport salt mine near Cleveland, Ohio. It was an imaging Čerenkov detector, which consisted of a 23 m × 17 m × 19 m tank, instrumented by 2048 8-inch PMTs facing inward and filled by 8 ktons of pure water. The fiducial volume of the detector was 3.3 kton for the neutrino analysis. IMB had also three experimental phases with upgrading the detector performance and observed supernova neutrinos and atmospheric neutrinos. The experiment ended at 1991, but the 8-inch PMTs and wavelength shifter plates were recycled for the outer detector of Super-Kamiokande.

1.2.3 Soudan 2 experiment

The Soudan 2 experiment is located 710 m underground in the Soudan Underground Mine State Park in Minnesota. The detector is an time projection, tracking calorimeter. It consists of 224 modules each weighting 4.3 tons and having an average density of 1.6 g/cc. About 85% of the mass of the module is provided by 1.6 mm thick sheets of corrugated steel. The sheets are stacked to form a hexagonal "honeycomb" structure. Plastic drift tubes fill the space in the honeycomb. The calorimeter modules are surrounded by an 1700 m^2 active shield of aluminum proportional tubes to identify particles which enter or exit the detector.

The Soudan 2 experiment presents the "contained events" sample which is defined as one in which no primary particle in the event leaves the fiducial volume, defined by a 20 cm depth

cut on all sides of the detector. The events are classified as "track", "shower", "multiprong" or "proton" by event scan.

1.2.4 Fréjus experiment

The Fréjus detector was located near the center of the highway tunnel connecting Modane (France) to Bardonecchia (Italy) under Alps. The average rock overburden amounts to 1720 m (4710 m.w.e.). The detector is a iron calorimeter with the total mass of 900 tons measuring 6 m × 6 m × 12.3 m, and have a sandwich structure consisting of 912 flash chambers and iron planes. 113 planes of Geiger tubes are interspersed and provide the trigger. The data taking started February 1984 with mass of 240 tons, and the size of the detector was gradually increased until the final mass of 900 tons was reached. The experiment ended in September 1988. The events are classified as "contained" or "semicontained" events. An event is classified to be semicontained if a possible primary vertex found inside the detector and at least one track is leaving the apparatus.

1.2.5 Nusex experiment

Nusex (Nucleon Stability Experiment) detector was locate in a highway tunnel under Mont Blanc in the French Alps, with 4800 m.w.e overburden. The detector is an iron calorimeter of a 3.5 m cube, consisting of layered iron slabs and plastic streamer tubes. The total mass is 150 tons, 130 tons of which is used as a fiducial mass.

1.3 Atmospheric neutrino problem

As the investigations of atmospheric neutrino by these experiments were going on, two inconsistent results about the flavor ratio of neutrino had been discussed and caused the atmospheric neutrino problem.

Kamiokande and subsequently IMB reported the anomalous results in the neutrino favor ratio in the sub-GeV region, in which visible energy of a event (E_{vis}) is less than about 1 GeV. They expressed their measurement by the ratio of μ-like to e-like compared to the expectation, $R(\mu/e) = (\mu/e)_{data}/(\mu/e)_{exp}$, and emphasized this ratio to be only about 60% of the expectation [4, 6]. Soudan 2 experiment also investigated the flavor ratio of atmospheric neutrino with

experiment	R(μ/e)
Kamiokande sub-GeV	$0.60^{+0.06}_{-0.05} \pm 0.05$ [5]
multi-GeV	$0.57^{+0.08}_{-0.07} \pm 0.07$ [5]
IMB-3 sub-GeV	$0.54 \pm 0.05 \pm 0.012$ [6]
multi-GeV	$1.4^{+0.4}_{-0.3} \pm 0.3$ [7]
Soudan 2	$0.72 \pm 0.19^{+0.05}_{-0.07}$ [8]
Fréjus	$1.00 \pm 0.15 \pm 0.08$ [9]
Nusex	$0.96^{+0.32}_{-0.28}$ [10]

Table 1.1: Summary of the measured R(μ/e) value before Super-Kamiokande. The first error shows statistical error and the second shows systematic error.

tracking detector and supported their results [8]. Table 1.1 shows the world summary of the flavor ratio, $R(\mu/e)$, reported before Super-Kamiokande.

Furthermore, Kamiokande published a very impressive report about the zenith angle dependence of $R(\mu/e)$ in the multi-GeV energy region ($E_{vis} > 1.33$ GeV) [5], as shown in Fig 1.6. These results were explained by the neutrino oscillation, which is caused by the finite mass of neutrino. Neutrino oscillation is a flavor transition phenomenon caused by the mixing between mass eigenstate and flavor eigenstate and the transition probability depends on the neutrino energy and propagation length. The oscillation mode was considered to be either $\nu_\mu \leftrightarrow \nu_e$ or $\nu_\mu \leftrightarrow \nu_\tau$, with the difference of neutrino mass square (Δm^2) being $\sim 10^{-2}$ eV^2, as shown in Fig 1.7.

However, Fréjus and Nusex experiments offered the different results on atmospheric neutrino measurement from those of Kamiokande and IMB. They presented $R(\mu/e)$ value which agreed with the expectation and asserted that no evidence for neutrino oscillation had been found in the atmospheric neutrino sample [9, 10]. But the statistical errors of their measurement were large compared with Kamiokande and IMB.

Several hypotheses to solve the problem were discussed actively. One of them was the suspicion of performance of particle identification in water Čerenkov detectors. In order to verify the performance of the Kamiokande detector, a prototype 1000 ton detector of Kamiokande was constructed at KEK in Japan, and a beam test was carried out using it. The electron and muon beams in the momentum range of 100~1000 MeV/c were injected into various positions of the

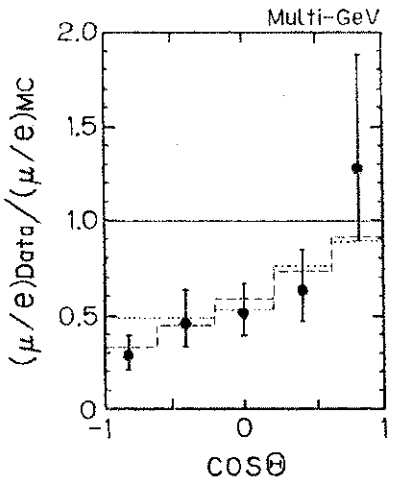

Figure 1.6: Zenith angle distribution of R(μ/e) for multi-GeV energy range in Kamiokande [5]. Histograms show the Monte Carlo prediction with neutrino oscillations for parameter sets (Δm^2,$\sin^2\theta$) corresponding to $\nu_\mu \leftrightarrow \nu_e$ ($(1.8\times10^{-2}$,1.0),dashes) and $\nu_\mu \leftrightarrow \nu_\tau$ ($(1.6\times10^{-2}$,1.0),dots) oscillation.

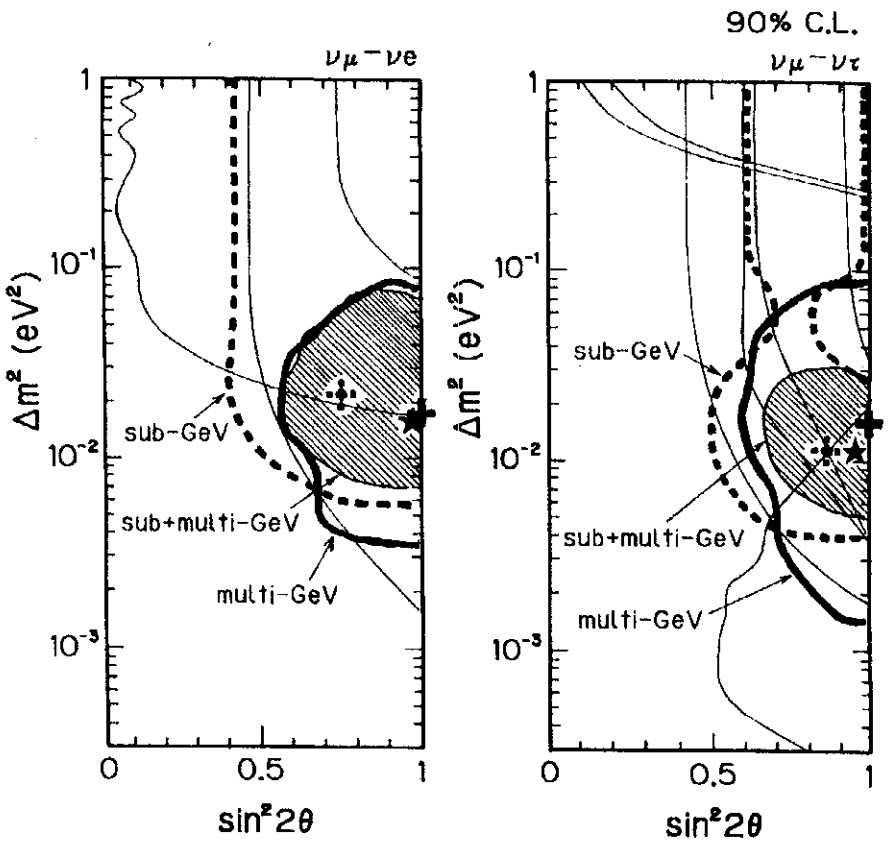

Figure 1.7: 90 % C.L. allowed oscillation parameters ($\sin^2 2\theta$,Δm^2) for $\nu_\mu \leftrightarrow \nu_e$ (left) and $\nu_\mu \leftrightarrow \nu_\tau$ (right) oscillations. Shaded regions shows the allowed region by Kamiokande sub-GeV and multi-GeV data.

tank, and the vertex resolution, energy resolution and particle identification performance were investigated extensively [11]. The misidentification probabilities for electron and muon events were estimated to be less than $\sim$ 3%. The agreement of data and Monte Carlo simulation was confirmed.

The possible background of neutrons produced in the rock was also suggested as follows [12]: When the isolated neutron, which is produced by the hadronic shower induced by high energy cosmic ray muon, comes into the underground detector, a neutral pion (π^0) can be created inside the fiducial volume without any hits in the outer detector and can be a background for e-like event due to the overlapping of two gammas caused by the π^0 decay.

Kamiokande studied the contribution of the neutron background using π^0-like events [13], which was identified by the two Čerenkov rings of e-like and the cut of reconstructed invariant mass corresponding to the π^0 mass. The distribution of the distance from the detector wall was examined because an excess should appear near the detector wall due to the inelastic interactions of neutron in water (attenuation length is about $\sim$60 cm). No clear excess was found and the background level for the sub-GeV e-like events was estimated to be less than 1.2 % at 90 % confidence level (C.L.). And for multi-GeV e-like the background contamination was also estimated less than 14 % at 90 % C.L.. These results excluded the neutron background hypothesis.

1.4 Neutrino oscillation

If neutrinos have a finite mass, the flavor changing phenomena, called neutrino oscillation, can occur. Neutrinos interact via the weak interaction in the flavor eigenstates $|\nu_\alpha\rangle$ ($\alpha = e, \mu, \tau$). However, if neutrinos have a finite mass, the mass eigenstates $|\nu_i\rangle$ ($i = 1, 2, 3$) exist and can be different from the flavor eigenstates. In this case, the flavor neutrino states can be expressed by the superpositions of the mass eigenstates as follows:

$$|\nu_\alpha\rangle = \sum_i U_{\alpha i} \, |\nu_i\rangle \tag{1.1}$$

where U is a unitary mixing matrix between flavor eigenstates and mass eigenstates of neutrino ($UU^* = U^*U = 1$). In the following, we will consider the flavor indices $\alpha, \beta = e, \mu, \tau$ and the mass indices $i, j = 1, 2, 3$. The mixing matrix for three neutrinos is usually expressed as follows,

analogously to the Cabibbo-Kobayashi-Masukawa (CKM) quark mixing matrix.

$$U = \begin{pmatrix} c_{12}c_{13} & s_{12}c_{13} & s_{13}e^{-i\delta} \\ -s_{12}c_{23} - c_{12}s_{23}s_{13}e^{i\delta} & c_{12}c_{23} - s_{12}s_{23}s_{13}e^{i\delta} & s_{23}c_{13} \\ s_{12}s_{23} - c_{12}c_{23}s_{13}e^{i\delta} & -c_{12}s_{23} - s_{12}c_{23}s_{13}e^{i\delta} & c_{23}c_{13} \end{pmatrix} \tag{1.2}$$

where s_{ij} and c_{ij} $(i,j{=}1,2,3)$ show $\sin\theta_{ij}$ and $\cos\theta_{ij}$, respectively and θ_{ij} is the mixing angle of two mass eigenstate, ν_i and ν_j. δ is the CP violation term.

In the two mixing case, the mixing matrix is given by the following 2 by 2 matrix with θ being the only one mixing angle:

$$U = \begin{pmatrix} \cos\theta & \sin\theta \\ -\sin\theta & \cos\theta \end{pmatrix} \tag{1.3}$$

1.4.1 Neutrino oscillation in vacuum

The mass eigenstate $|\nu_i\rangle$ with a finite mass m_i, momentum p and energy $E_i = \sqrt{p^2 + m_i^2}$ satisfies the following energy eigenvalue equation:

$$\mathcal{H}_0 \, |\nu_i\rangle = E_i \, |\nu_i\rangle \tag{1.4}$$

where $\mathcal{H}_0$ is the free neutrino Hamiltonian. The time evolution of the neutrino state is expressed by the Schrödinger equation.

$$\begin{aligned} i\frac{d}{dt} \, |\nu_\alpha(t)\rangle &= \mathcal{H}_0 \, |\nu_\alpha(t)\rangle \\ &= \sum_i U_{\alpha i} E_i \, |\nu_i(t)\rangle \\ &= \sum_{i,\beta} U_{\alpha i} E_i U^*_{\beta i} \, |\nu_\beta(t)\rangle \\ &= \sum_{i,\beta} U_{\alpha i} \, \frac{m_i^2}{2p} \, U^*_{\beta i} \, |\nu_\beta(t)\rangle \end{aligned} \tag{1.5}$$

The relativistic approximation $E_i \simeq p + m_i^2/2p$ is used in (1.5). The $|\nu_\alpha(t)\rangle$ can be obtained by solving this equation analytically.

$$
\begin{aligned}
|\nu_\alpha(t)\rangle &= \sum_{i,\beta} U_{\alpha i} \exp\left(-i\frac{m_i^2}{2p}t\right) U^*_{\beta i} |\nu_\beta(0)\rangle \\
&= \sum_\beta A_{\alpha\beta} |\nu_\beta(0)\rangle \qquad (1.6)
\end{aligned}
$$

where $A_{\alpha\beta}$ shows the transition amplitude from ν_β to ν_α and the oscillation probability can be obtained by squaring it.

$$
\begin{aligned}
P(\nu_\beta \to \nu_\alpha) &= |A_{\alpha\beta}|^2 \\
&= \mathrm{Re}\sum_{j,k} U_{\alpha j} U^*_{\beta j} U^*_{\alpha k} U_{\beta k} \exp\left(-i\frac{\Delta m^2_{jk} L}{2p}\right) \\
&= \delta_{\alpha\beta} - \mathrm{Re}\sum_{j,k} U_{\alpha j} U^*_{\beta j} U^*_{\alpha k} U_{\beta k} \left\{1 - \exp\left(-i\frac{\Delta m^2_{jk} L}{2p}\right)\right\} \qquad (1.7) \\
&= \delta_{\alpha\beta} - 4\sum_{j<k} U_{\alpha j} U^*_{\beta j} U^*_{\alpha k} U_{\beta k} \sin^2\left(\frac{\Delta m^2_{jk} L}{4p}\right) \qquad (1.8)
\end{aligned}
$$

The unitarity condition

$$
\sum_j U_{\alpha j} U^*_{\beta j} = \delta_{\alpha\beta} \qquad (1.9)
$$

is used in (1.7). $\Delta m^2_{jk} \equiv m^2_j - m^2_k$ is the difference of mass square. The time t is equal to the neutrino propagation length L in natural unit. In the 2-flavor mixing case, the mixing matrix is given by (1.3) and the oscillation probability (1.8) is given in a much simple form:

$$
\begin{aligned}
P(\nu_\beta \to \nu_\alpha) &= \sin^2 2\theta \sin^2\left(\frac{\Delta m^2 L}{4p}\right) \qquad (\alpha \neq \beta) \qquad (1.10) \\
P(\nu_\alpha \to \nu_\alpha) &= 1 - \sin^2 2\theta \sin^2\left(\frac{\Delta m^2 L}{4p}\right) \qquad (1.11)
\end{aligned}
$$

(1.10) shows the transition probability from ν_β to ν_α and (1.11) shows the survival probability of ν_α.

According to (1.10) and (1.11), the oscillation length in vacuum, L_v, is determined by momentum p and Δm^2 and given by

$$L_v = \frac{4\pi p}{|\Delta m^2|} = 2.48 \left(\frac{p}{\mathrm{GeV/c}}\right) \left(\frac{|\Delta m^2|}{\mathrm{eV}^2}\right)^{-1} \mathrm{km} \quad (1.12)$$

In the case of $L \gg L_v$, the survival probability approaches to $1 - 1/2 \sin^2 2\theta$, where $1/2$ appears because the value of $\sin^2\left(\frac{\Delta m^2 L}{4p}\right)$ averages out there. The neutrino oscillation can be observed in the condition of $\frac{\Delta m^2 L}{4p} \gtrsim 1$, therefore the region of $10^{-4} \lesssim \Delta m^2 \lesssim 10^{-1}$ can be detected with the atmospheric neutrinos whose typical energy is about 1 GeV and propagation length is $15 \sim 13000$ km.

1.4.2 Neutrino oscillation in matter

When neutrinos propagate through matter, neutrinos fell potentials which are caused by the forward scattering with matter. In this case, the contribution from the neutral current and charged current should be considered. ν_e, ν_μ and ν_τ interact with electrons, protons and neutrons via neutral current, but only ν_e interacts with electrons via charged current. This effect modifies the behavior of the neutrino oscillation significantly. The potential for ν_e by charged current is given as follows:

$$V_e = \sqrt{2} G_F N_e = 7.63 \times 10^{-14} \left(\frac{N_e}{N_A cm^{-3}}\right) \mathrm{eV} \quad (1.13)$$

where G_F is the Fermi constant, N_e is the electron number densities in the medium and N_A is Avogadro number. For electron anti-neutrino $\bar{\nu_e}$, the sign of this potential is opposite ($\bar{V_e} = -V_e$).

Including the effect of the potential, the equation (1.5) is modified as follows:

$$i\frac{d}{dt} |\nu_\alpha(t)\rangle = \frac{1}{2p} \left(\sum_{i,\beta} U_{\alpha i}\, m_i^2\, U^*_{\beta i} + A\delta_{\alpha e}\delta_{\beta e} \right) |\nu_\beta(t)\rangle \quad (1.14)$$

$$= \frac{1}{2p} M^2 |\nu_\beta(t)\rangle \quad (1.15)$$

where $A = 2V_e p = 2\sqrt{2} G_F N_e p$.

It is difficult to solve this evolution equation exactly for neutrinos propagating in matter where the electron density is not constant. But in the case of constant density medium, one can diagonalize the matrix M^2 and obtain its eigenvalue and eigenfunction.

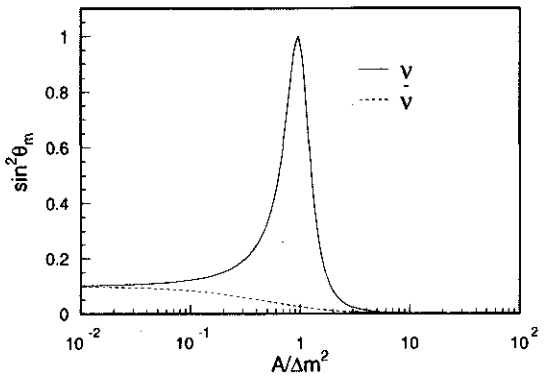

Figure 1.8: $\sin^2 2\theta_m$ as a function of $A/\Delta m^2$ for $\sin^2 2\theta = 0.1$. The solid line shows the case of neutrino and the dashed line shows the case of anti-neutrino.

In the case of 2-flavor mixing, the eigenvalue $M^2_{1,2}$ of the mass matrix M^2 is obtained by the following equation:

$$U^*_m \, M^2 \, U_m = \begin{pmatrix} M^2_1 & 0 \\ 0 & M^2_2 \end{pmatrix} \tag{1.16}$$

where

$$U_m = \begin{pmatrix} \cos\theta_m & \sin\theta_m \\ -\sin\theta_m & \cos\theta_m \end{pmatrix}$$

and θ_m correspond to the mixing matrix and mixing angle in matter, respectively. $M^2_{1,2}$ corresponds to the square of neutrino mass in matter. The matter oscillation is described by replacing Δm^2 and θ with ΔM^2 and θ_m, respectively. The mass square difference $\Delta M^2_{12} = M^2_2 - M^1_1$ and $\sin^2 2\theta_m$ are calculated from (1.16) as follows:

$$\Delta M^2 = \Delta m^2 \sqrt{(A/\Delta m^2 - \cos 2\theta)^2 + \sin^2 2\theta} \tag{1.17}$$

$$\sin^2 2\theta_m = \frac{\sin^2 2\theta}{(A/\Delta m^2 - \cos 2\theta)^2 + \sin^2 2\theta} \tag{1.18}$$

When A goes to 0, ΔM^2 and $\sin^2 2\theta_m$ become those of vacuum oscillation. The oscillation probability in matter is expressed by (1.10) and (1.11) with the replacement of $\Delta m^2 \to \Delta M^2$ and $\theta \to \theta_m$. For three neutrino mixing, the eigenvalue of the mass matrix M^2 is also analytically solved [14, 15].

One of the interesting feature in the matter oscillation is the enhancement of $\sin^2 2\theta_m$. If a condition $A = \Delta m^2 \cos 2\theta$ is satisfied, the $\sin^2 2\theta_m$ becomes maximal (=1) even though the mixing angle θ is small.

Fig 1.8 shows $\sin^2 2\theta_m$ as a function of $A/\Delta m^2$ in the case of $\sin^2 2\theta = 0.1$. It is seen that the resonance occurs around $A/\Delta m^2 \sim 1$. However, the oscillation is suppressed for anti-neutrino due to $A \to -A$. Furthermore in $A \gg \Delta m^2$ region, the oscillation is always suppressed by the factor $\sim (\Delta m^2/A)^2$ for both neutrinos and anti-neutrinos.

This theory was first suggested by Wolfenstein [16] and later by Mikheyev and Smirnov and named as MSW effect after them. It was applied for the enhancement of solar neutrino oscillations inside the Sun [17].

1.4.3 3-flavor oscillation with one mass scale

The behavior of the 3-flavor mixing oscillation is much more complicated than that of the 2-flavor mixing. In the case of the vacuum oscillations, the oscillation probability is expressed by the superpositions of three wave components, whose oscillation lengths are $4\pi p/|\Delta m^2_{21}|$, $4\pi p/|\Delta m^2_{32}|$ and $4\pi p/|\Delta m^2_{31}|$, therefore the physical implications are far from transparent. But if m_3^2 is largely separated from m_1^2 and m_2^2, the oscillation behavior becomes much simple [18, 19]. In this case, two mass states (ν_1,ν_2) are assumed to be degenerate in mass and

$$m_3^2 - m_{1,2}^2 = \Delta m^2$$

becomes the dominant mass square difference in the neutrino oscillation (one mass scale dominance).

The Δm^2 can be fulfilled with either $m_3 > m_{1,2}$ or $m_3 < m_{1,2}$. These two cases are not entirely equivalent when neutrinos oscillate in matter. But in quarks and charged leptons, mass of the lower generation is lighter than that of the higher generation, therefore the hypothesis of the mass hierarchy

$$m_1 < m_2 < m_3$$

can be assumed and Δm^2 is taken to be positive in this thesis.

In the case of the one mass scale dominance, the generic oscillation probability in vacuum (1.8) is modified with $\Delta m^2_{32,31} \to \Delta m^2$ and $\Delta m^2_{21} \to 0$.

$$P(\nu_\beta \to \nu_\alpha) = \delta_{\alpha\beta} - 4(U_{\alpha 1}U^*_{\beta 1} + U^*_{\alpha 2}U_{\beta 2})U_{\alpha 3}U^*_{\beta 3}\sin^2\left(\frac{\Delta m^2 L}{4p}\right)$$
$$= \delta_{\alpha\beta} - 4(\delta_{\alpha\beta} - U_{\alpha 3}U^*_{\beta 3})U_{\alpha 3}U^*_{\beta 3}\sin^2\left(\frac{\Delta m^2 L}{4p}\right) \quad (1.19)$$

After the unitarity condition (1.9) is applied in (1.19), the transition and survival probabilities are expressed by

$$P(\nu_\beta \to \nu_\alpha) = 4|U_{\alpha 3}|^2|U_{\beta 3}|^2\sin^2\left(\frac{\Delta m^2 L}{4p}\right) \qquad (\alpha \neq \beta) \quad (1.20)$$

$$P(\nu_\alpha \to \nu_\alpha) = 1 - 4|U_{\alpha 3}|^2(1 - |U_{\alpha 3}|^2)\sin^2\left(\frac{\Delta m^2 L}{4p}\right) \quad (1.21)$$

The following features of oscillation probabilities are considered in this oscillation scheme:

- Δm^2, $|U_{e3}|^2$, $|U_{\mu 3}|^2$ and $|U_{\tau 3}|^2$ are seen in the oscillation probabilities, further $|U_{\tau 3}|^2$ is determined to be $1 - |U_{e3}|^2 - |U_{\mu 3}|^2$ according to the unitarity condition (1.9). $|U_{e3}|^2$ and $|U_{\mu 3}|^2$ is expressed to be

  $$|U_{e3}|^2 = \sin^2\theta_{13}, \qquad |U_{\mu 3}|^2 = \cos^2\theta_{13}\sin^2\theta_{23}$$

  As a result, the oscillation probabilities are determined by only three parameters, $(\Delta m^2, \theta_{23}, \theta_{13})$, and does not depend on the mixing angle, θ_{12}, and the CP violating phase, δ. It remains valid for the oscillations in matter [19].

- All oscillation channels ($\nu_e \leftrightarrow \nu_\mu$, $\nu_\mu \leftrightarrow \nu_\tau$, $\nu_e \leftrightarrow \nu_\tau$) are open and have the same oscillation length $L_v = 4\pi p/|\Delta m^2|$. Pure 2-flavor oscillations are also available by the following parameterization:

  $\theta_{13} = 0$ pure $\nu_\mu \leftrightarrow \nu_\tau$
  $\theta_{23} = \pi/2$ pure $\nu_e \leftrightarrow \nu_\mu$
  $\theta_{23} = 0$ pure $\nu_e \leftrightarrow \nu_\tau$

- The expressions (1.20) and (1.21) have the same form as those of the two flavor mixing with the replacement

$$\sin^2 2\theta_{\alpha\beta} = 4|U_{\alpha 3}|^2|U_{\beta 3}|^2 \tag{1.22}$$

$$\sin^2 2\theta_{\alpha\alpha} = 4|U_{\alpha 3}|^2(1-|U_{\alpha 3}|^2) \tag{1.23}$$

These equalities are useful in comparing the 3-flavor oscillation result with the experimental results which were analyzed by 2-flavor mixing scheme.

Furthermore, we can consider about the 3-flavor matter oscillation with one mass scale dominance [19]. Assuming that neutrinos propagate in the matter of constant density, the effective mass squares are induced in the matter oscillation and expressed as follows:

$$\begin{aligned} M^2_{1,3} &= \Delta m^2 \left\{ \frac{1+A/\Delta m^2}{2} \mp \frac{1}{2}\sqrt{(A/\Delta m^2 - \cos 2\theta_{13})^2 + \sin^2 2\theta_{13}} \right\} \\ M^2_2 &= 0 \end{aligned}$$

And the effective mixing angle in matter θ^m_{13} is given by

$$\sin^2 \theta^m_{13} = \frac{\sin^2 2\theta_{13}}{(A/\Delta m^2 - \cos 2\theta_{13})^2 + \sin^2 2\theta_{13}} \tag{1.24}$$

This equation is similar to that of the 2-flavor matter oscillation, and the resonance also occurs at the condition $A = \Delta m^2 \cos 2\theta_{13}$.

With these variables, the transition and survival probabilities are given analogously to that of the vacuum oscillation

$$P(\nu_e \to \nu_e) = 1 - \sin^2 2\theta^m_{ee} \sin\left(\frac{\Delta M^2_{31} L}{4p}\right) \tag{1.25}$$

$$P(\nu_e \to \nu_\mu) = \sin^2 2\theta^m_{e\mu} \sin\left(\frac{\Delta M^2_{31} L}{4p}\right) \tag{1.26}$$

$$P(\nu_\mu \to \nu_\mu) = 1 - \sin^2 2\theta^m_{\mu\mu} \sin\left(\frac{\Delta M^2_{31} L}{4p}\right)$$

$$
\begin{aligned}
&- \sin^2 2\theta_{23} \sin^2 \theta_{13}^m \sin^2 \left(\frac{M_1 L}{4p}\right) \\
&- \sin^2 2\theta_{23} \cos^2 \theta_{13}^m \left\{ \sin^2 \left(\frac{M_3 L}{4p}\right) - \sin^2 \left(\frac{\Delta M_{13} L}{4p}\right) \right\}
\end{aligned} \tag{1.27}
$$

where $\Delta M_{31}^2 = M_3^2 - M_1^2$ and

$$\sin^2 2\theta_{ee}^m = \sin^2 2\theta_{13}^m \tag{1.28}$$

$$\sin^2 2\theta_{e\mu}^m = \sin^2 \theta_{23} \sin^2 2\theta_{13}^m \tag{1.29}$$

$$\sin^2 2\theta_{\mu\mu}^m = \sin^4 \theta_{23} \sin^2 2\theta_{13}^m + \sin^2 2\theta_{23} \cos^2 \theta_{13}^m \tag{1.30}$$

For $\nu_e \to \nu_e$ and $\nu_e \to \nu_\mu$ oscillation, the oscillation probabilities are realized by only replacing $\theta_{13} \to \theta_{13}^m$ and $\Delta m^2 \to \Delta M_{31}^2$, and they depend only on one oscillation length

$$L_m^{31} = \frac{4\pi p}{\Delta M_{31}^2} \tag{1.31}$$

However, the oscillation probability of $\nu_\mu \to \nu_\mu$ is much complicated and has three different oscillation length, L_m^{31}, L_m^3, L_m^1, which are given by

$$L_m^3 = \frac{4\pi p}{M_3^2}, \qquad L_m^1 = \frac{4\pi p}{M_1^2} \tag{1.32}$$

It had been pointed that the presence of L_m^1 component in $\nu_\mu \to \nu_\mu$ transition probability produces the negligible matter effect in the case of $\Delta m^2 \gg A$ [19, 20]. In this region, the oscillation lengths in matter are approximated by

$$L_m^{31} \simeq L_m^3 \simeq \frac{4\pi p}{\Delta m^2} \equiv L_m^{short}, \qquad L_m^1 \simeq \frac{4\pi}{V_e(1 + \cos 2\theta_{13})} \equiv L_m^{long} \tag{1.33}$$

where V_e is the potential for ν_e by charged current, expressed by Eq 1.13. The short oscillation length L_m^{short} corresponds to the oscillation length in vacuum, but L_m^{long} is due to the matter effect and as a function of the electron density in matter, N_e. In the case of $N_e = 3\ N_A \mathrm{cm}^{-3}$, which is the average density in the Earth, L_m^{long} is about 1000 km. In the case of $\Delta m^2 \gg A$, the probabilities due to L_m^{short} can be averaged:

$$\langle P(\nu_e \to \nu_e) \rangle = 1 - \frac{1}{2} \sin^2 2\theta_{ee}^m \tag{1.34}$$

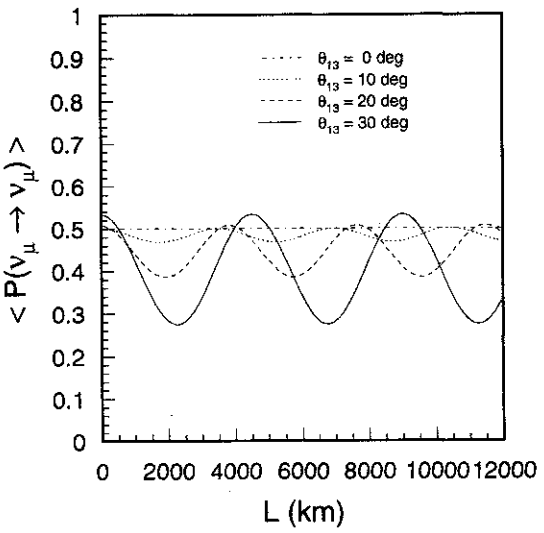

Figure 1.9: Averaged survival probability of $\nu_\mu \to \nu_\mu$, in 3-flavor matter oscillation. $\nu_\mu \to \nu_\mu$ transition is suppressed due to the matter effect in $\Delta m^2 \gg A$ region. Parameters are set to be $\Delta m^2 = 10^{-2}$ eV^2, N$_e$ = 3 N$_A$cm^{-3} and $\theta_{23} = \pi/4$.

$$\langle P(\nu_e \to \nu_\mu) \rangle = \frac{1}{2} \sin^2 2\theta^m_{e\mu} \tag{1.35}$$

$$\langle P(\nu_\mu \to \nu_\mu) \rangle = 1 - \frac{1}{2} \sin^2 2\theta^m_{\mu\mu} - \sin^2 2\theta_{23} \sin^2 \theta^m_{13} \sin^2 \left(\frac{L}{L^{long}_m} \right) \tag{1.36}$$

The averaged probabilities of the electron neutrino are constant and very close to the corresponding averaged probabilities in vacuum. On the other hand, there is a additional term depending on L^{long}_m for the survival probability of muon neutrino and it suppresses the $\nu_\mu \to \nu_\mu$ transition in the condition of $\Delta m^2 \gg A$ region. The large θ_{23} and θ_{13} tend to enhance the suppression because the degree of the suppression is proportional to $\sin^2 2\theta_{23} \sin^2 \theta^m_{13}$.

Fig 1.9 shows the averaged $\nu_\mu \to \nu_\mu$ survival probability as a function of the neutrino propagation length at $\Delta m^2 = 10^{-2}$ eV^2, N$_e$ = 3 N$_A$cm^{-3} and $\theta_{23} = \pi/4$. Changing θ_{13} largely, the survival probability is more suppressed and it is possible to lower the averaged probability less than 0.5 according to the observed position.

1.5 Motivation of this thesis

Atmospheric neutrino problem may not be solved by any hypothesis except neutrino oscillation. In order to conclude this problem, the large statistics of the atmospheric neutrino data is necessary. Super-Kamiokande detector has the 22.5 kton fiducial volume, which is more than 20 times larger than that of Kamiokande, and about 3000 events are expected per year. Such a large

amount of data should give evidence for the neutrino oscillation and show us which neutrino oscillation of $\nu_\mu \leftrightarrow \nu_e$ or $\nu_\mu \leftrightarrow \nu_\tau$ mainly occurs for the atmospheric neutrinos. Furthermore, it may be possible that two mixing angles and matter effect are related to the atmospheric neutrino problem (i.e., the 3-flavor neutrino oscillation effect).

Based on these motivations, we analyze 33.0 ktonyr of the atmospheric neutrino data observed in Super-Kamiokande. Details on the μ/e ratio, momentum distribution and zenith angle distribution are discussed. The 2-flavor oscillation analysis and the 3-flavor oscillation analysis with one mass scale dominance, which was described in the previous section, are performed.

Chapter 2

Detector

Super-Kamiokande detector is located at the Kamioka Observatory of Institute for Cosmic Ray Research, in the Kamioka mine of Gifu Prefecture, Japan. The latitude and longitude are 36° 25'N and 137° 18'E, respectively. It lies at a mean overburden of the 1000 m thickness of rock, which is equivalent to 2700m of water, below the peak of Mt. Ikenoyama, and the detector site is about 2km away horizontally from the entrance of the mine. There is rich natural water flowing near the detector site and it is used as the bases of pure water filled in the Super-kamiokande detector. The temperature in the mine is about 10 ℃, and stable all throughout the season. The main purpose of this experiment is to observe several types of neutrinos (atmospheric neutrinos, solar neutrinos and supernova neutrinos) preciously and prove nucleon decay which is predicted by the Grand Unified Theories (GUTs). The Super-Kamiokande experiment started taking data on April 1 1996 and continued taking data up to now without any serious trouble.

2.1 Detection method

Super-Kamiokande is an imaging water Čerenkov detector. It detects Čerenkov light generated by charged particles which propagate in water. Čerenkov light can be emitted when the velocity of charged particles exceeds the light velocity in the medium (c/n), where n is the refractive index of the medium, for water, it's about 1.33. The threshold momenta for the Čerenkov radiation are 0.58, 120, 153 MeV/c for electrons, muons, pions, respectively.

The Čerenkov light is emitted in a cone of half angle θ toward the direction of the particle track. This θ is called Čerenkov angle and determined as follows:

$$\cos\theta = \frac{1}{n\beta} \tag{2.1}$$

where $\beta = v/c$ and θ is about 42° for $\beta = 1.0$ in water. The spectrum of the Čerenkov light as a function of the wavelength λ is expressed as follows:

$$\frac{dN}{d\lambda dx} = \frac{2\pi\alpha}{c}\left(1 - \frac{1}{n^2\beta^2}\right)\frac{1}{\lambda} \tag{2.2}$$

where α is fine structure constant and x is the length of charged particle trajectory. About 390 photons are emitted per 1cm of pass length in water in the wavelength region 300nm $\sim$ 700nm, where the photo multiplier tubes are sensitive.

2.2 Detector features

Super-Kamiokande detector is a cylindrical water tank whose size is 41.4 m in height and 39.3 m in diameter, instrumented with photomultiplier tubes (PMT), electronics and online data acquisition systems and a water purification system. The water tank is made of stainless steel and contains 50000 tons of pure water. The detector has two PMT layers, called as the inner detector (ID) and outer detector (OD), and the outer detector surrounds the inner detector completely.

The diameter, height and volume of the inner detector are 33.8 m, 36.2 m, and 32 kton, respectively. 11460 20-inch PMTs are used for the inner detector. 7650 PMTs are attached to side wall and the rest are top and bottom walls. The PMTs are placed at intervals of 70 cm grid and the gaps are lined with black polyethylene terephthalate sheets, which are called as "black sheet". The photocathod coverage is about 40%.

The outer detector surrounds the inner detector completely and its thickness is 2.0 m for the side and 2.2 m for the top and bottom. It is instrumented with 1885 8-inch PMTs and each PMT is fitted with a 60cm square plate of wavelength shifter to maximize the light collection efficiency. Tyvek sheets which are known as a reflective material are covered to enhance light collection further. The outer detector has a important role of reducing backgrounds. It is used as a veto-counter which identifies cosmic-ray muons and it is easy to identify them because the entrance and exit points of muons can be detected with it. Also the water of 2 m thickness in the outer detector shields against gamma ray and neutron backgrounds from the rock.

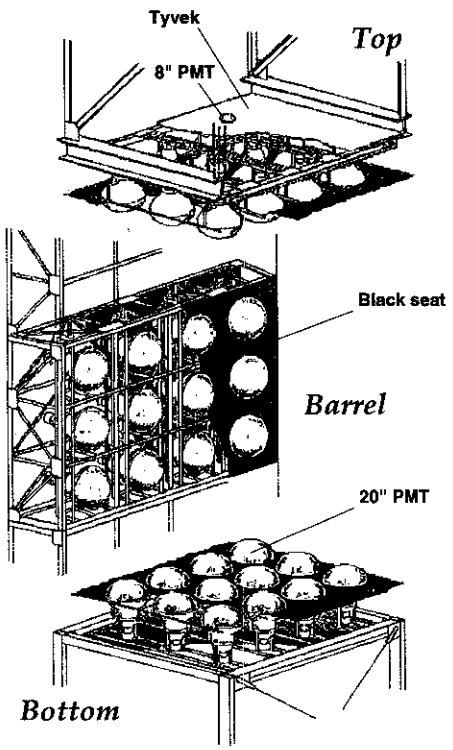

Figure 2.1: Schematic view of the frame which supports PMTs

These two detector volumes are optically isolated from each other by black sheet and Tyvek sheet as shown in Fig. 2.1.

2.3 Photomultiplier tube

The photomultiplier tubes (PMTs) with 20-inch in diameter were originally developed by Hamamatsu Photonics K.K. in cooperation with members of Kamiokande [21]. The 20-inch PMTs used in Super-Kamiokande have some improvements over those used in Kamiokande. The size and shape of this PMT is shown in Fig 2.2. The photo-cathode is made of bialkali (Sb-K-Cs) that is suited for the collection of Čerenkov light. The quantum efficiency is shown in Fig 2.3 and its value is 21 % at the wave length $\lambda = 400$nm, which is the typical wave length of Čerenkov light.

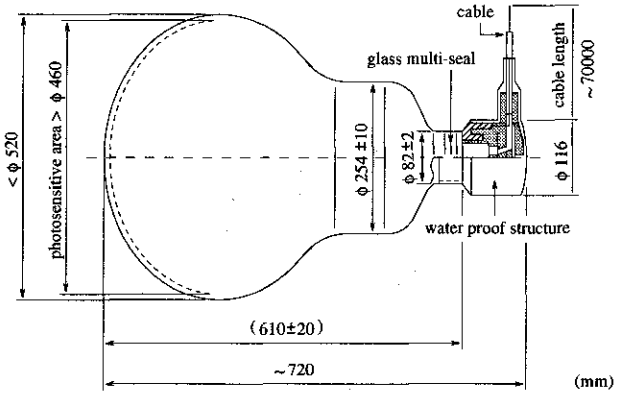

Figure 2.2: Schematic view of 20-inch PMT used in the inner detector.

A Venetian-blind type dynode is used and the bleeder-chain is optimized in order to achieve good timing response and collection efficiency of photoelectrons. The average collection efficiency is more than 70%. The one photoelectron peak can be seen clearly as shown in Fig 2.4. The transit time spread is about 2.2nsec [22]. The PMT have a uniform response under the condition that the geomagnetic field is less than 100 mG. The geomagnetic field inside the tank is kept less than 100 mG based on the field compensation by 26 sets of Helmholtz coils which surround the detector. The average rate of dark noise is about 3.1 kHz and gain of PMT is about 10^7 when 2000 Volt is supplied.

The PMT used in the outer detector is 8-inch Hamamatsu R1408 PMT, which is recycled from the IMB experiment. The size of wavelength shifter which is fitted the outer PMT is 60cm on each side and 1.3cm thick. It absorbs light in ultraviolet and re-radiates blue light where the PMT are the most sensitive. Consequently, the light collection efficiency increases by 60% [23]. The timing resolution of the PMT is about 11 nsec, and after fitting wavelength shifter, it degrades to more than 15 nsec. Nevertheless it is enough for tagging the events.

2.4 Electronics for inner detector

Fig 2.5 shows the electronics system used in the inner detector. The system has two types of modules, TKO(TRISTAN/KEK Online) module [24] and VME module. These are 48 TKO and

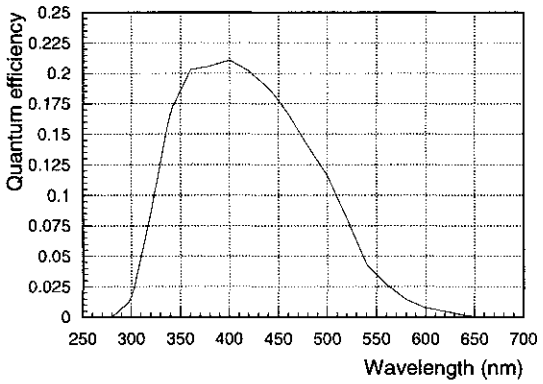

Figure 2.3: Quantum efficiency of 20-inch PMT as a function of wavelength of photon

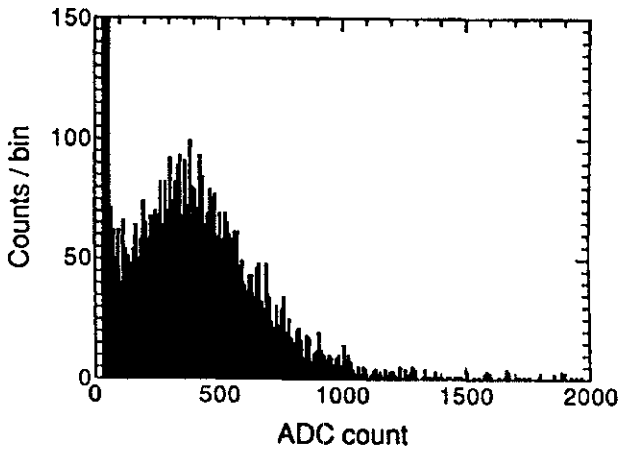

Figure 2.4: One photoelectron distribution measured by 20-inch PMT

8 VME creates in total and they are distributed in 4 electronics huts. Additionally one VME module for the global trigger (TRG module) is located in the central hut.

Initial process of the PMT signals is done by the TKO modules. This system consists of up to 20 Analog Timing Modules (ATMs) [25], one Go/NoGo (GONG) trigger module and one Super-Controller Header bus interface (SCH) module.

934 ATMs are used for the inner detector and each ATM has 12 PMT input channels. The ATM provides a 1.2 μsec full range with 0.3 nsec resolution in time and a 550 pC full range with 0.2 pC resolution. Each channel has a pair of switching time-to-analog converters (TAC) and charge-to-analog converters (QAC) to measure the time and charge of an input pulse. These pair of switching channel is called "A" and "B" respectively and they realize the continuous, dead-time free data acquisition, for example, for a stopped muon and a decay electron accompanied to it.

Each channel in the ATM has an amplifier with a gain of 100 and a dicriminator. The threshold is set to 100mV which is equivalent to about 0.32 p.e., and when input signal exceeds this threshold, a rectangular pulse (200 nsec width and 11mV height), is generated. The rectangular pulses from the all hit PMTs are added ("HITSUM" signal) and sent to the global trigger module in the central hut and simultaneously a gate window of 900 nsec width is opened to start time measurement in TAC and charge accumulation in QAC. QAC accumulates charge in 400 nsec time window and keeps it until the global trigger arrives. If the global trigger does not arrive within 1.3 μsec , the storages in TAC and QAC are cleared. On the contrary, when the global trigger arrives, charge and timing information are digitized by ADC and sent via SCH to the memory (SMP) in the VME module.

Pedestals of ATMs are measured at an interval of 30 minutes. Only 1/8 of all the ATM are measured at once in order not to fail supernova events.

2.5 Electronics for outer detector

The electronics system used in the outer detector is constructed by the collaborators of U.S. universities and systematized independently with that of the inner detector. Fig 2.6 shows the font-end modules for the quadrant electronics system. It consists of 40 paddle cards, 10 charge-to-timing converters (QTCs) modules , 5 time-to-digital converters (TDCs) and one FASTBUS

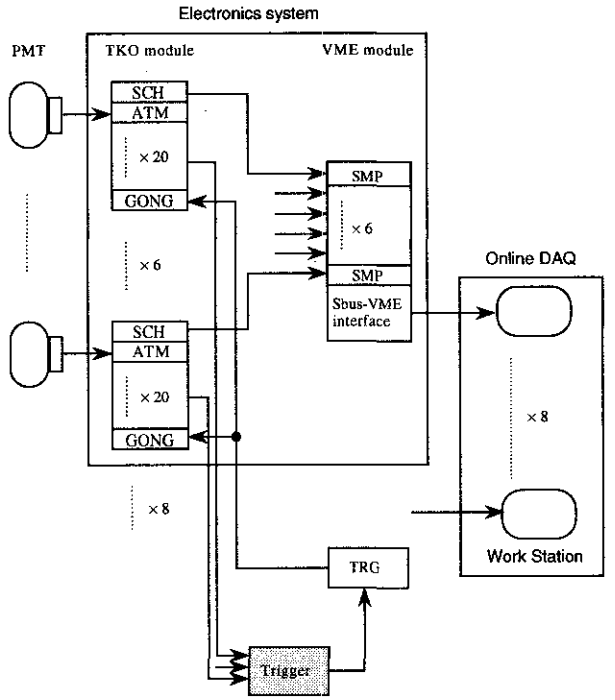

Figure 2.5: Inner detector data acquisition system

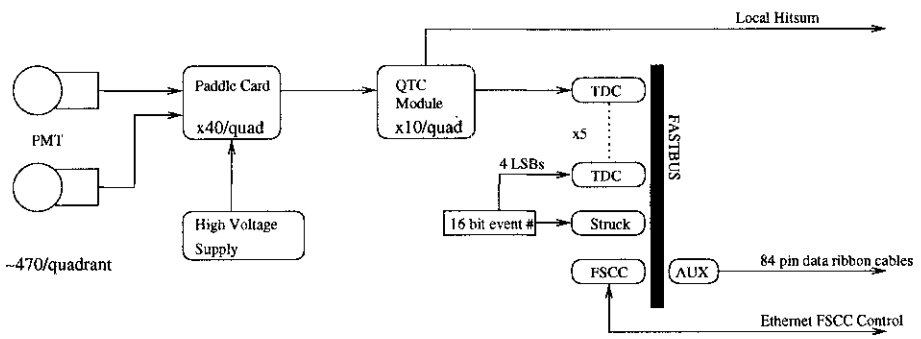

Figure 2.6: Outer detector acquisition system

smart crate controller (FSCC).

The paddle card has 12 PMT channels. The signal and high voltage lines are AC coupled and the paddle card has a role to pick off the PMT signals through a high voltage capacitor.

The QTC module converts a PMT signal into a logic pulse (ELC level), the leading edge of which corresponds to the arrival time of signal and the width is proportional to the integrated charge of PMT pulse. The QTC module also provides a HITSUM signal (200 nsec, 20mV rectangular pulse) and send it to the trigger module in the central hut.

The LeCroy 1877 Multi-hit Time-to-Digital Converter is used for the TDC modules of the outer detector and it has up to 96 ELC level inputs per one module. The least count accuracy of the TDC modules is 0.5 nsec. The TDC module serves as a pipeline buffer within 32 μsec and digitize 16 of the most recent signals and stores in the memory. The time window was set to the full 32 μsec centered around the trigger time in the early period of the operation, but in September 1996, this width was cut to 16 μsec (trigger time is 10 μsec after opening gate) in order to reduce the amount of data. The control and read-out of the TDC modules are operated by FSCC and the stored data are sent to the online machines.

2.6 Trigger

The Super-Kamiokande detector has 3 triggers for the inner detector, which are named as High energy trigger (HE), Low energy trigger (LE) and Super Low energy trigger (SLE), and 1 trigger for the outer detector, Outer detector trigger (OD). Each of them is triggered by its own level of HITSUM signal independently.

The HE trigger is used mainly to identify cosmic-ray muon, atmospheric neutrino and proton decay candidates. It requires a coincidence of 31 HITSUM signals within 200nsec time window and the trigger rate is about 5 $\sim$ 6 Hz. The LE trigger is used for solar neutrino analysis above 5$\sim$6 MeV in the energy and its threshold is 29 HITSUM. Fig 2.7 shows the trigger rate of the HE and LE. They are stable through the period of this experiment.

The SLE trigger started from May-1997 in order to push the the analysis threshold of solar neutrino energy spectrum down to 4.6 MeV. The computer upgrade and the increase of the network speed make it possible. The SLE triggered events are not used at all in the atmospheric neutrino analysis and removed at the first step of the data reduction.

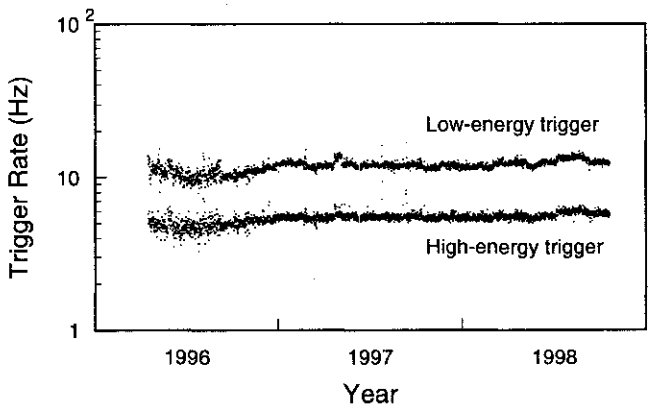

Figure 2.7: Figure of the low-energy and high-energy trigger rate as a function of year.

The OD trigger is used for the rejection of the cosmic-ray muons. It is formed by the coincidence of 19 HITSUM signals from the QTC modules in the outer detector. If the OD trigger is generated, the trigger signal is sent to the TRG modules.

The global trigger is generated independently when any of these four trigger is generated, and the data stored in memory modules is read through online workstations.

2.7 Data acquisition and offline system

The data acquisition system consists mainly of 8(1) slave workstations for collecting data of the inner(outer) detector and 1 host workstation for controlling run status and collecting data from the 9 slave workstations. The host workstation provides the graphical interface for shift workers to control run status, and sends commands to each slave workstation via socket according to the requirement of shift workers. Each slave workstation reads out the data from electronics modules when the global trigger is generated, and transfers it to the host workstation via FDDI network. The host workstation concatenates all the information of hit PMTs for both inner and outer detectors, and records as one event.

The data, which are builded as an event in the host workstation, are passed to the offline system. First, the format of data is changed to "ZEBRA" format, which is easy to handle and

store additional information. The sequence of data is separated into a data file in every ten minutes, the data size of which corresponds to about 50 M Bytes. This reformatted data is transfered from the detector site to the offline computer facility out of the mine, and stored to the magnetic tape library. At the same time, the data are transfered to the recalibration process, which is called as"TQREAL", and the primary reduction. In the TQREAL process, the timing and charge information of PMTs are converted from ADC and TDC counts to units of photoelectron and nanosecond, respectively, according to the pedestal height and the calibration constant. Several primary reductions for the different energy range, including the fully-contained and partially-contained first reductions (see section 4), run in parallel with a total of 20 CPUs in order to process a large amount of data speedy. The reducted data are also stored to the tape library and the subsequent reduction is processed by each analysis group.

2.8 Water purification system

The 50000 ton of pure water is filled in the Super-Kamiokande detector It was produced from the natural water flowing near the detector site and filled into the detector. The water purification system circulates 50 m^3 of pure water per hour to keep its quality. The instruments to measure the water quality are equipped in various places and continuous monitor. The purpose of the water purification is to remove the radioactive material and bacteria and keep high water transparency. The radioactive materials, especially radon (^{222}Rn), become a background of solar neutrino analysis and make it difficult to lower the analysis energy threshold.

Fig 2.8 shows the water purification system. The solid line shows the main circulation of water and the dotted line shows the supplementary circulation line. The heat exchanger keeps the temperature of water about 13 °C to suppress bacteria growth. The Ion exchanger and cartridge polisher remove metal ions such as Ra and Th in the water. The ultra-violet sterilizer kills bacteria in water. The gas in water, such as oxygen and radon, is removed by the vacuum degasifier and finally the ultra filter (UF) removes the small dust which size is the order of 10 nanometers.

After the water purification, the concentration of radon, which is 10^4Bq/m^3 in the mine water, is reduced to < 10mBq/m^3 and the light attenuation length is kept to about 100 m at a wavelength of 420 nm.

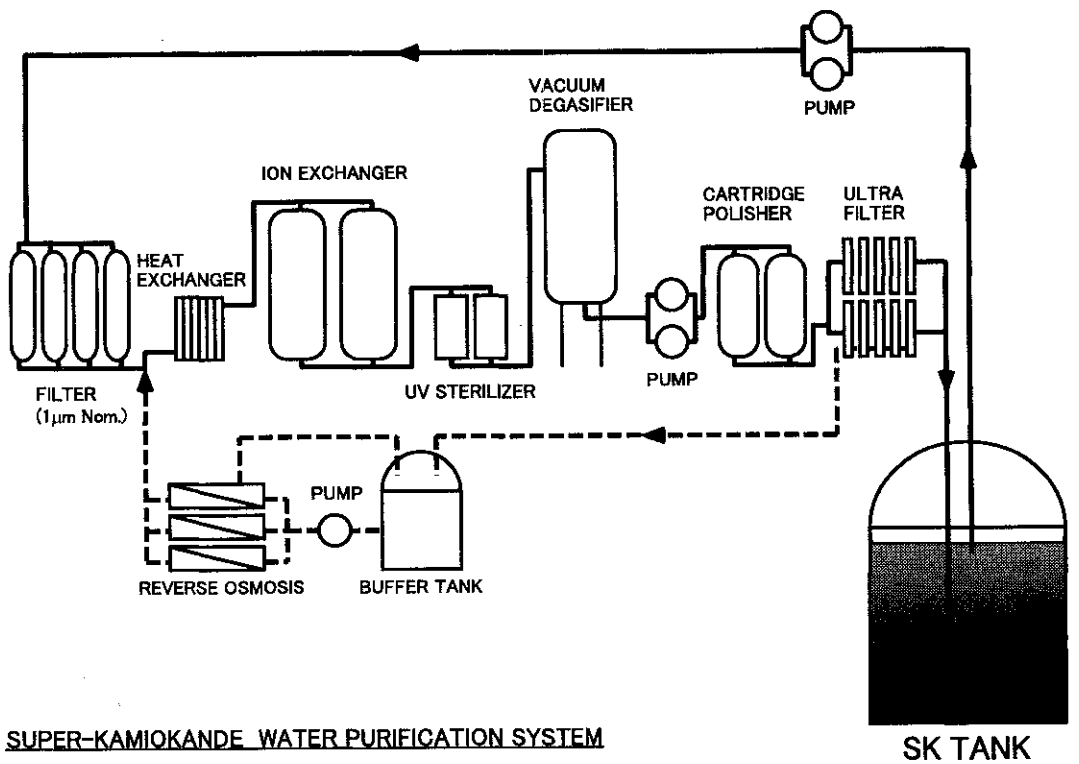

Figure 2.8: Water purification system.

Chapter 3

Calibration

3.1 Relative gain calibration

The uniformity of relative gain in all PMTs is important to measure the momentum without systematic difference in zenith angle direction. At the beginning of the experiment, the relative gain was measured by a Xe-lamp calibration system and the proper high voltage value for each PMT was determined so that all PMT have same gain. Fig 3.1 shows the relative gain calibration system by a Xe-lamp. The light generated by a Xe-lamp is passed through an ultra-violet (UV) filter and split into some lines. One is injected into a scintillator ball via an optical fiber and others are used for monitoring the light intensity and triggering data.

The scintillator ball is made of acrylic resin mixed with BBOT scintillator and MgO powder. The BBOT scintillator has a role of wavelength shifter, which absorbs UV light and re-emits light whose wavelength is peaked at 440 nm. The MgO powder is used for diffusing light in the ball.

The relative gain of the i-th PMT is expressed as follows:

$$G_i = \alpha \cdot \frac{Q_i}{f(\theta)} \cdot r_i^2 \exp\left(\frac{r_i}{L}\right)$$

where α is the normalization factor, Q_i is the measured charge of i-th PMT, r_i is the distance from the light source to PMT, L is the light attenuation length and $f(\theta)$ is the relative photosensitive area as a function of PMT facing angle.

The gain of each PMT are measured at various different positions by changing the height of the ball in the detector to minimize the position dependence. The relative gain spread after

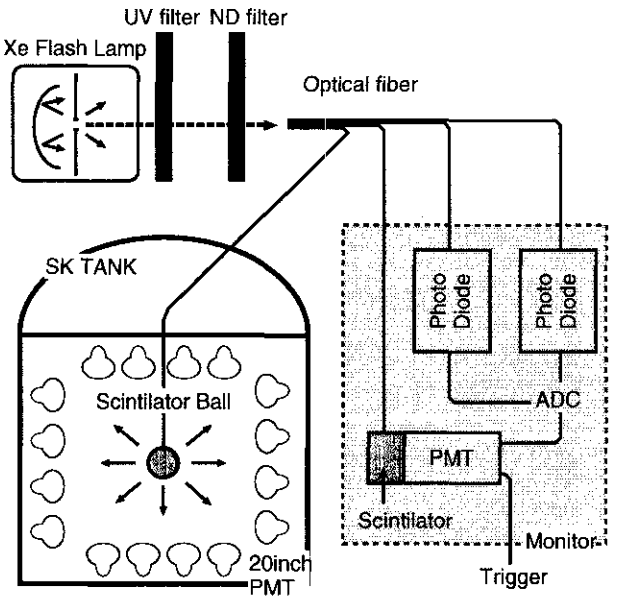

Figure 3.1: Schematic view of the absolute gain calibration system.

adjusting high voltage is ~7%.

3.2 Single photoelectron distribution

The absolute gain of the PMT is determined by using charge distribution of single photoelectron (p.e.) signal, which is obtained using low energy gamma ray emitted by the Ni(n,γ)Ni* reaction. Fig 3.2 shows the schematic view of the calibration source. The cylindrical polyethylene vessel contains ^{252}Cf source, nickel wires and water. The ^{252}Cf is used as a neutron source and the nickel wires are filled inside the vessel completely. The energy of gamma ray is about 6 $\sim$ 9 MeV, corresponding to 50 $\sim$ 80 p.e. in total charge, therefore the number of photon observed in a PMT is at most one.

The single photoelectron distribution for a typical PMT is also shown in Fig 3.2. The large spike near zero is caused by the fact that a fraction of the photoelectrons go through the first dynode of the PMT. The mean value in this distribution is 2.055 pico coulomb (pC) and we always use this constant to convert PMT charge from pico coulomb to photoelectron.

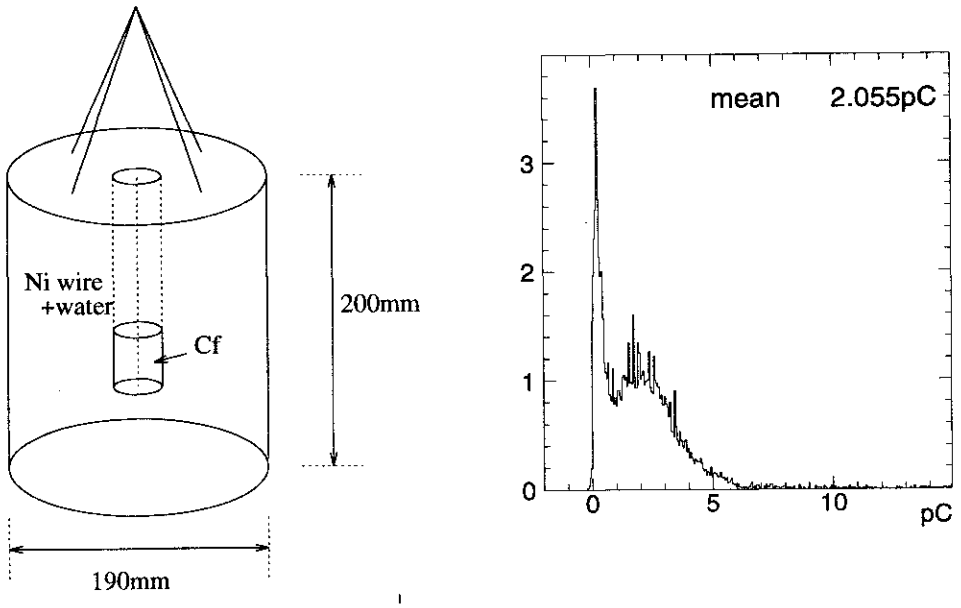

Figure 3.2: Schematic view of Nickel calibration source (left) and charge distribution of an inner detector PMT (right) in Nickel calibration. The peak around 2 pC corresponds to that of single photoelectron

3.3 Timing calibration

The timing calibration of the PMTs is important for determination of vertex position because vertex fitting depends on the timing information of each PMT largely. The timing response depends on the cable length, the transit time of a PMT and the pulse height due to the slewing effect in the discriminator. Therefore the timing difference should be measured as a function of pulse height for each PMT.

Fig 3.3 shows the calibration system of relative timing of the PMTs. We use the N_2 laser light source which emits light of 337 nm in wavelength, and a dye laser module converts to 384 nm which is near the wavelength of Čerenkov light. The time width of laser pulse is less than 3 nsec. The laser light is split into two, one is injected into the diffuser ball in the water tank via an optical fiber and another is used for monitoring the intensity and triggering the data-taking system. The intensity of light is changeable using an optical filter and the timing response is measured at various levels of pulse height.

Fig 3.4 shows the typical 2-dimensional plot of timing and charge. This plot is made for each PMT.

3.4 Water transparency

The water transparency is an important information to determine the energy of an event independent of the vertex position. Also in order to keep the energy scale constant throughout the period of the experiment, the continuous measurement is necessary. We have two independent methods to measure the light attenuation length. One is the method by a dye laser and a CCD camera. This method can measure the wavelength dependence of the attenuation length by changing the dye of the laser. Another is by comic ray muons. This method cannot measure the wavelength dependence, but it can measure the wavelength-averaged transparency without disturbing normal data taking and check the stability of water transparency continuously.

3.4.1 Laser and CCD camera method

Fig 3.5 shows the system for the measurement of water transparency with a laser and a CCD camera. For the light source, a N_2 laser and a dye module are used [26]. The dye module can

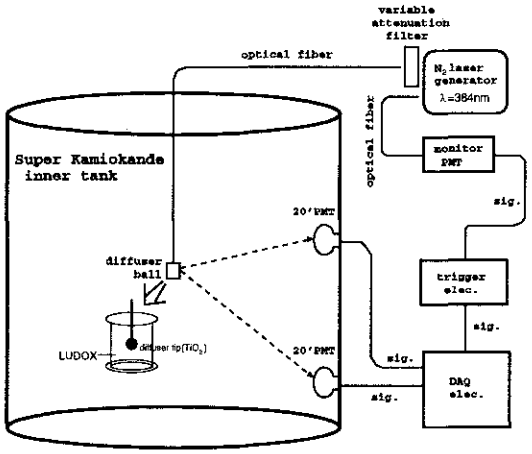

Figure 3.3: Relative timing calibration system using laser light source.

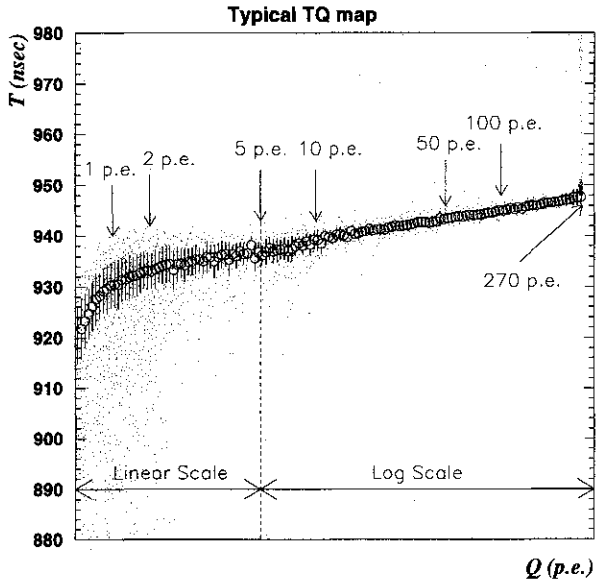

Figure 3.4: Figure of the relation between Q (p.e.) and T (nsec) for a typical PMT. Circles and error bars show peak values and resolutions (1σ level).

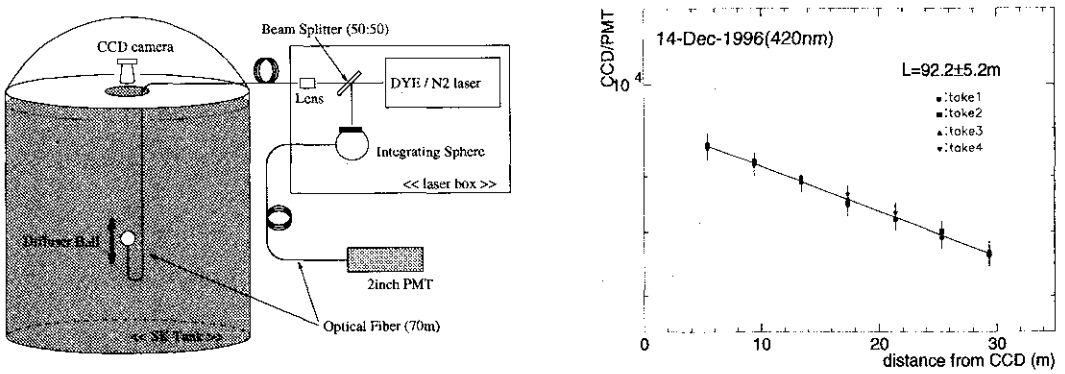

Figure 3.5: System of water transparency measurement by a laser and a CCD camera (left figure) and the ratio of I_{CCD} to I_{laser} as a function of the distance from the CCD camera at 420 nm in wavelength (right figure).

shift the wavelength of the laser beam to 337 $\sim$ 600 nm. The laser light is injected into an acrylic diffuser ball which is sunk in the water tank and its intensity (I_{laser}) is monitored simultaneously. The diffuser ball diffuses the laser light isotropically and the CCD camera , which is set at the top of the tank, takes an image of the diffuser ball. The intensity of the light from the diffuser ball (I_{CCD}) is measured from this image. The distance from CCD camera is changed from 5 m to 30 m. Fig 3.5 shows the $\frac{I_{CCD}}{I_{laser}}$ as a function of the distance from CCD camera when the wavelength of laser is set to 420 nm. The attenuation length is obtained by fitting these data with a least square method The derived water transparency is 92.2 m in Fig 3.5. The results of this measurement is described in section 5.4.2.

3.4.2 Cosmic ray muon method

The events of cosmic-ray muons are suitable for continuous measurement of the attenuation length. The attenuation length is measured at every run. Is is used in the reconstruction programs, such as the determination of momentum. The drift of the PMT gain averaged over all the PMTs can be measured simultaneously and it is also used for the correction of momentum.

The vertical-going muons entering from the top of the detector and exiting to the bottom, are selected and the muon track is reconstructed by connecting the entering and exiting points. The number of photoelectron observed by the i-th PMT, Q_i, is a function of the flight length of

a photon, l_i, and is expressed as follows:

$$Q_i = \alpha \cdot \frac{f(\Theta_i)}{l_i} \cdot \exp\left(-\frac{l_i}{L}\right)$$

where α is the normalization factor, $f(\Theta_i)$ is the relative sensitive area of PMT and L is the attenuation length. The track of muons are reconstructed as a connecting line between the entrance and exiting point, and the photon flight length for the i-th PMT, l_i is defined as the distance between the PMT and the emitted point on the track, where the opening angle to PMT is 42°. The above equation is transformed as follows:

$$\log\left(\frac{Q_i \times l}{f(\theta)}\right) = -\frac{l}{L} + const.$$

Fig 3.6 shows $\log\left(\frac{Q_i \times l}{f(\theta)}\right)$ as a function of l in a typical run and the attenuation length is obtained from the fitted slope. The estimator of PMT gain is also derived from this figure as a intersection at y-axis with the fitted line. The drift of this value does not exactly correspond to the PMT gain drift, but it can be approximated as the relative gain drift of the whole PMT.

The variation of the attenuation length and PMT gain are shown in Fig 3.7 as a function of time. The average value of 30 runs is used for atmospheric analysis in order to reduce the statistical fluctuation.

In this thesis, the data taken before 27-May-1996, when the attenuation length less than 90 m, was not used because the quality of data was quite different due to shorter and unstable attenuation length.

3.5 Absolute energy calibration

We calculated the momentum of the particle from the charge information of PMT (see section 6.5) and its energy scale is estimated from Monte Carlo simulation. Therefore, it is important to understand how precise the Monte Carlo simulation reproduces the absolute energy scale because the systematic uncertainty in the absolute energy scale affects the atmospheric neutrino measurement directly. We have calibrated the absolute energy scale using the following 5 calibration sources.

- muon-decay electron

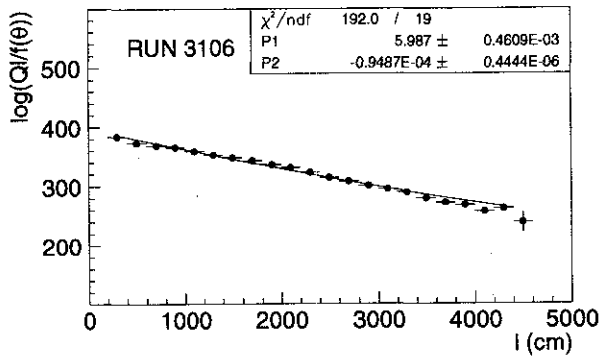

Figure 3.6: The log $\left(\frac{Q_i \times l}{f(\theta)}\right)$ plot as a function of the photon flight length. Solid line shows the the result of fitting.

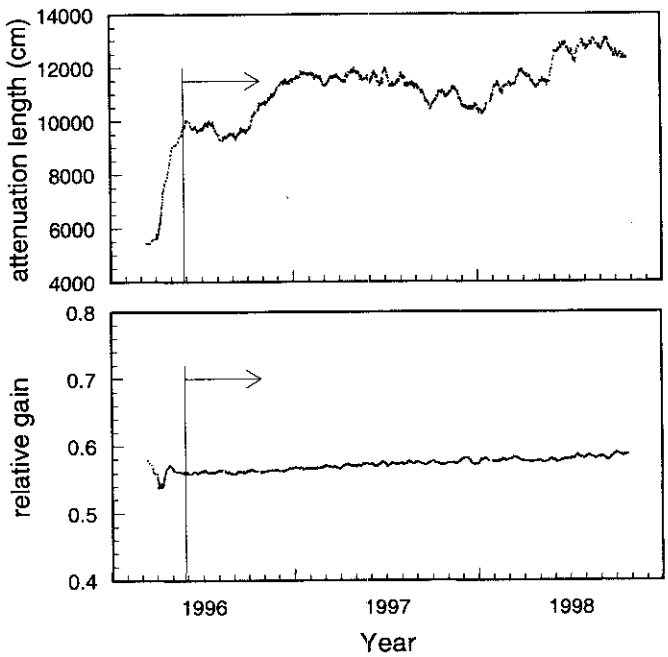

Figure 3.7: Time variation of attenuation length and relative PMT gain. Data which was taken after May-1996 (region to the left of arrow) is used for this thesis.

- LINAC
- π^0 invariant mass
- low-energy stopping muon
- high-energy stopping muon

3.5.1 Muon-decay electron

A large number of electrons are produced by the decay of cosmic-ray muons. The absolute energy scale is checked by comparing the energy spectrum of the decay electron between the data and Monte Carlo. Muon-decay electrons are selected by the following criteria:

1. Electrons triggered within 1.5 μsec to 8 μsec after the trigger of a parent muon are selected.
2. Number of PMT hits in the inner detector should be less than 1000.
3. Goodness of the low-energy fitter (G_{low}) should be more than 0.5.
4. Vertex position is reconstructed in the fiducial volume.

G_{low} shows the goodness of fitting the vertex position of event. It is calculated based on the timing information of PMT and takes the value from 0 to 1 (see section 6.1). Monte Carlo electron events are generated uniformly in the fiducial volume and randomly for the direction. The effect of the nucleon Coulomb field caused by the atomic capture of a parent muon [27] is taken into account for the energy spectrum of Monte Carlo electrons. Fig 3.8 shows the momentum spectrum of muon-decay electrons compared with Monte Carlo events. The shape of the momentum spectrum agrees well with Monte Carlo. The mean value of the Monte Carlo is 2.0 % lower than that of the data.

3.5.2 LINAC

An electron linear accelerator (LINAC) is instrumented at the Super-Kamiokande site and used to understand the performance of the detector for low energy events precisely [28]. The energy of electrons can be adjusted from 5~16 MeV and injected into the various point of Super-Kamiokande detector through the beam pipe. We use electrons with the energy of 16 MeV and

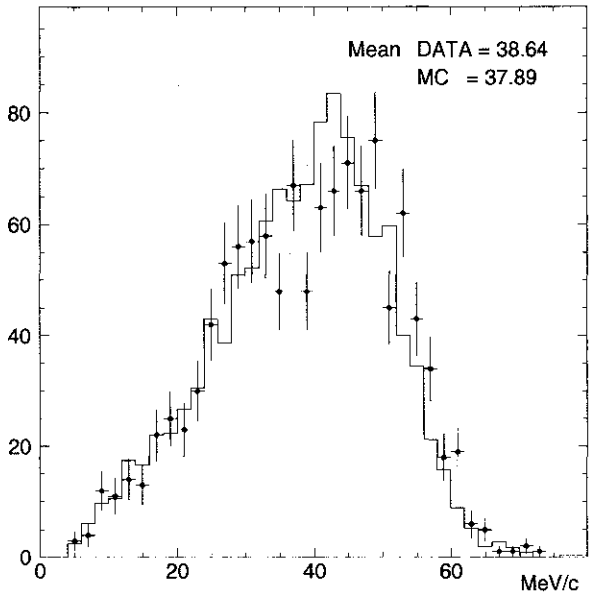

Figure 3.8: Momentum spectrum of muon-decay electron. Points with error bar show the data and histogram shows the Monte Carlo.

injected downward at 6 m from the inner top PMT plane. LINAC electrons events are selected according to the following criteria:

1. Number of PMT hits in the inner detector should be between 100 and 210.
2. Goodness of the low-energy fitter (G_{low}) should be more than 0.5.
3. The distance between the injected position and the reconstructed position should be less than 2 m.

Fig 3.9 shows the momentum distribution of LINAC electrons compared with Monte Carlo events. The agreement of the momentum distribution is good. The mean value of the Monte Carlo is 2.4 % higher than that of the data.

3.5.3 π^0 invariant mass

We can calibrate the absolute energy scale using single π^0 events which are produced by the atmospheric neutrino interaction. The π^0 invariant mass, M_{π^0}, is reconstructed by the momentum

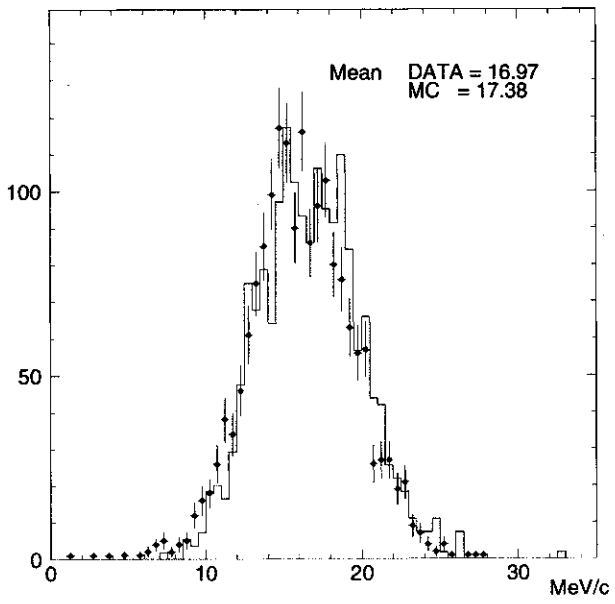

Figure 3.9: Momentum spectrum of LINAC electron. Points with error bar show the data and histogram shows the Monte Carlo.

of two gamma-rays, $P_{\gamma 1}$, $P_{\gamma 2}$, and their opening angle θ as follows:

$$M_{\pi^0} = 2P_{\gamma 1}P_{\gamma 2}(1 - \cos\theta)$$

The single π^0 events are selected by the atmospheric neutrino fully-contained sample with the following criteria:

1. There should be two Čerenkov ring in a event and both of them be identified as e-like.
2. Reconstructed π^0 momentum should be less than 400 MeV/c.
3. Vertex position should be in the fiducial volume.

Fig 3.10 shows the distribution of the reconstructed π^0 invariant mass for data and Monte Carlo. The clear peaks of π^0 around 135 MeV/c^2 can be seen in both distributions. By fitting the peaks with Gaussian distribution, The peak of the Monte Carlo distribution is 2.2 % lower than that of the data.

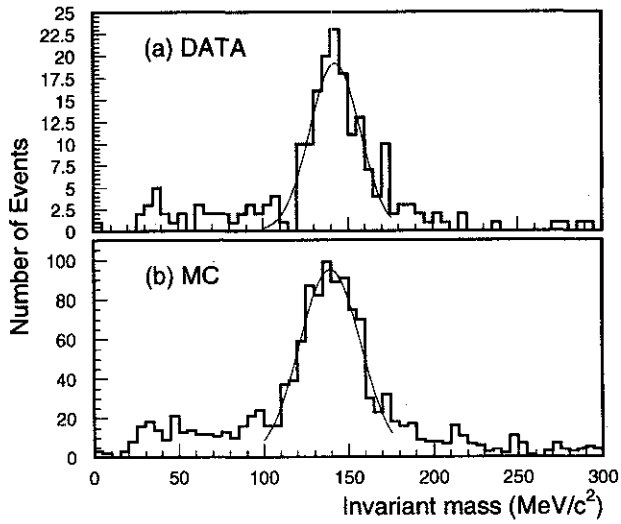

Figure 3.10: Distribution of the reconstructed π^0 invariant mass for (a) data and (b) Monte Carlo. Each peak is fitted by Gaussian distribution.

3.5.4 Low energy stopping muons

The Čerenkov opening angle is determined by the momentum as shown in Eq 2.1. For electrons, the opening angle is almost constant for the momentum of $P_e > 100$ MeV/c due to its small mass. However, for the low energy muons of $P_\mu \lesssim 350$ MeV/c, the Čerenkov opening angle depends largely on the momentum. We checked the energy scale comparing with the Čerenkov angle and the momentum for the low energy stopping muons. Fig 3.11 shows the reconstructed momentum as a function of the Čerenkov opening angle for the data and Monte Carlo events. We calculated a ratio, $R_{data,MC}$, which is defined as (momentum)/(momentum estimated by the Čerenkov opening angle). Fig 3.12 shows the $\langle R_{MC} \rangle / \langle R_{data} \rangle$ as a function of momentum. ($\langle R \rangle$ means the average of R.) This ratio shows the systematic difference of the momentum determination between the data and the Monte Carlo. The deviations from 1 are less than $\pm$ 2.5 %.

3.5.5 High energy stopping muons

We can estimate the momentum of high energy muons from its range because the range is almost proportional to the momentum. We used the stopping muons whose range is greater than

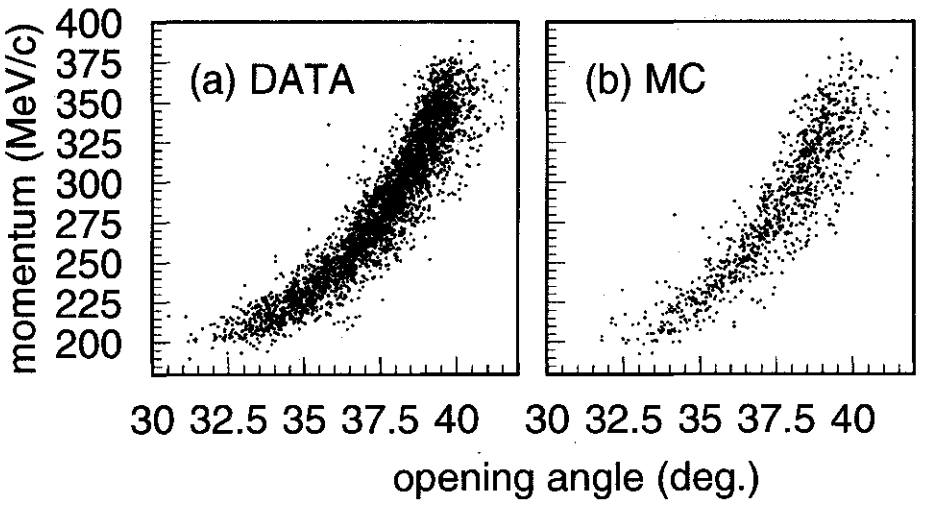

Figure 3.11: Distribution of the Čerenkov opening angle vs the momentum for the low energy stopping muons of (a) data and (b) Monte Carlo.

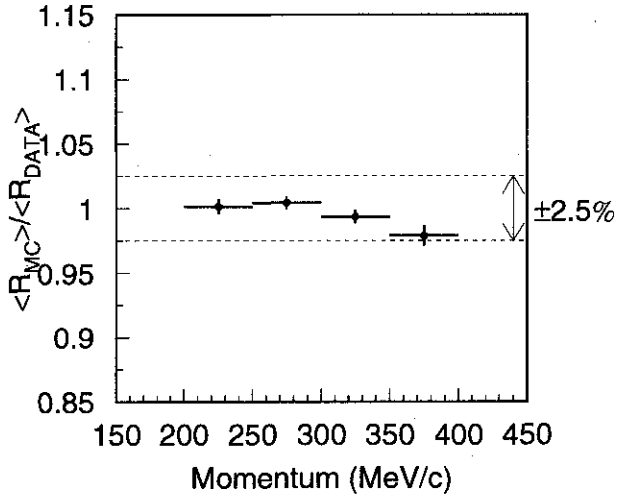

Figure 3.12: $\langle R_{MC} \rangle / \langle R_{data} \rangle$ as a function of momentum. Dotted lines show $\pm$ 2.5 %.

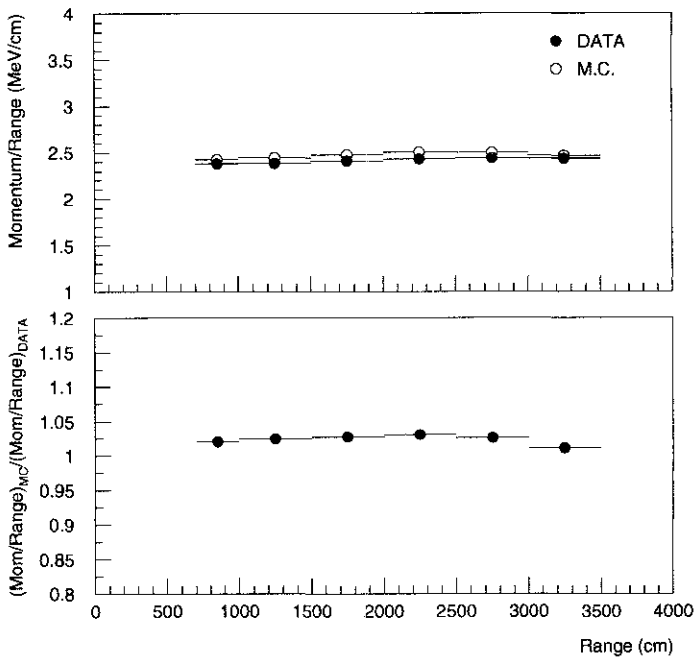

Figure 3.13: ⟨momentum/range⟩ for data and Monte Carlo and the ratio, ⟨mom./range⟩$_{MC}$/ ⟨mom./range⟩$_{data}$ as a function of range.

7 m and with one decay electron. The range is estimated by the distance from the entrance point and the vertex point of the decay electron. Fig 3.13 shows the ratio of momentum to range, ⟨mom./range⟩, as a function of range for the data and the Monte Carlo and the ratio, ⟨mom./range⟩$_{MC}$/ ⟨mom./range⟩$_{data}$. The deviation from 1 is estimated as the systematic difference of momentum determination.

3.5.6 Summary of the absolute energy scale

Fig 3.14 shows the summary of the absolute energy scale calibration. Events with the momentum from 16 MeV/c to about 10 GeV/c are examined and the uncertainty of the energy scale is estimated to be within ± 2.5 %.

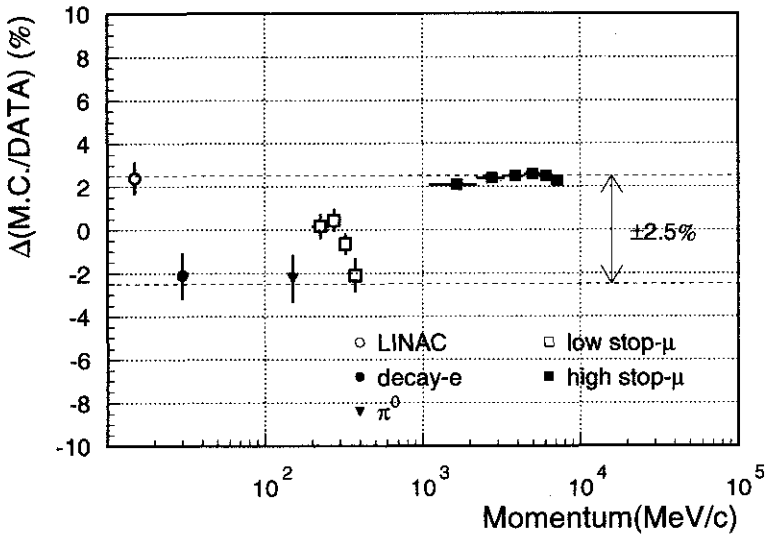

Figure 3.14: Summary of the absolute energy calibration with the several calibration sources. In total, the uncertainty is estimated within ± 2.5%.

Chapter 4

Reduction and event selection

In Super-Kamiokande, about 10^6 events are triggered per day excluding super-low-energy triggered events, and they are equivalent to 9 GB of data size. Most of them are caused by cosmic-ray muons and low energy events from radioisotope material. On the contrary, only $\sim$ 10 atmospheric neutrino events are observed per day. Therefore efficient reduction is necessary to select neutrino events among such large quantity of data.

In this thesis, two types of atmospheric neutrino sample are presented. One is fully-contained (FC) event, for which the whole particle tracks are contained within the inner detector. The momenta of particles can be measured because all of the particle energy are deposited inside the inner detector and the particle type can be identified using the Čerenkov ring pattern.

Another is partially-contained (PC) event, which requires vertex within the inner fiducial area and some energy deposit by an exiting charged particle in the outer detector. The PC events are regarded as muon neutrino events because of the presence of the exiting particle, most of which are muons. According to the Monte Carlo estimates, 98 % of them are caused by charged current (CC) $\nu_\mu + \bar{\nu}_\mu$ interactions.

Fig 4.1 shows the FC and PC typical events. For FC events, there is no possible energy deposit in the outer detector, but for PC event, the hit-PMT cluster which corresponds to the exit point of the particle can be seen in the outer detector. A fully-contained event which is identified to be electron (muon) by particle identification program is called by "e-like" ("μ-like") (see section 6.3).

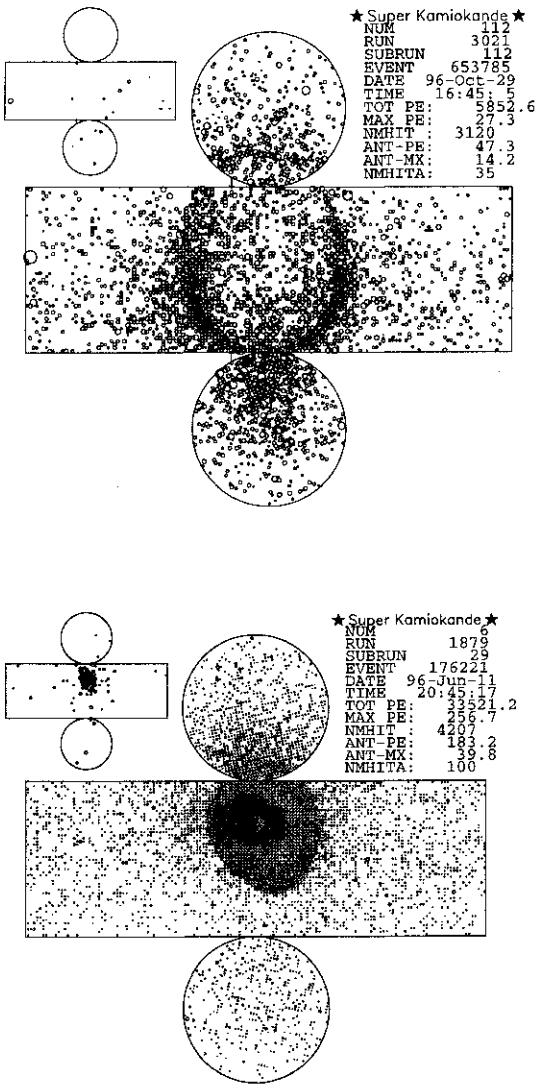

Figure 4.1: Visual displays of FC e-like (left upper), FC μ-like (right upper) and PC event (left lower), shown in the exploded view of the cylindrical tank. The left upper part of each display shows the outer detector.

4.1 Reduction for fully-contained events

There are 4 steps of reduction for the FC sample as shown in Fig 4.2. The main reduction scheme for this sample is to eliminate cosmic ray muons, low energy events from radioisotopes and electric noise events. The cut based on the number of hits in the outer cluster is efficient to reject cosmic muons.

4.1.1 1st reduction for FC sample

The first reduction for the FC sample is processed together with other first reduction programs (partially-contained, solar neutrino and upward-going muon). Therefore the simple and effective criteria are required so as not to load computer CPU power. About 3500 events are remained from 10^6 events per day by applying the following criteria:

1. The maximum number of photoelectron (p.e.) within 300 nsec time window (PE_{300}) observed in the inner detector should be greater than 200, which corresponds to 22 MeV/c for electrons and 190 MeV/c for muons.

2. The number of hits in the outer detector within 800 nsec time window (N_{hita}) should be less than 50 hits.

Fig 4.3 shows the PE_{300} distribution for data and final sample. The low energy background events caused by radon and gamma ray from the rock are eliminated by the first criteria. The majority of cosmic-ray through-going muons are rejected by the second criterion. The first reduction also passes the events accompanying within 30 μsec after the selected event so as to examine the presence of an electron produced by a muon decay and they are referred as "sub"-event attaching to the preceding event.

4.1.2 2nd reduction for FC sample

The 2nd reduction rejects low energy events and cosmic muon events furthermore. The reduction criteria are as follows:

1. PE_{max}(maximum number of p.e. in a PMT)/PE_{300} should be less than 0.5.

2. N_{hita} should be less than 25.

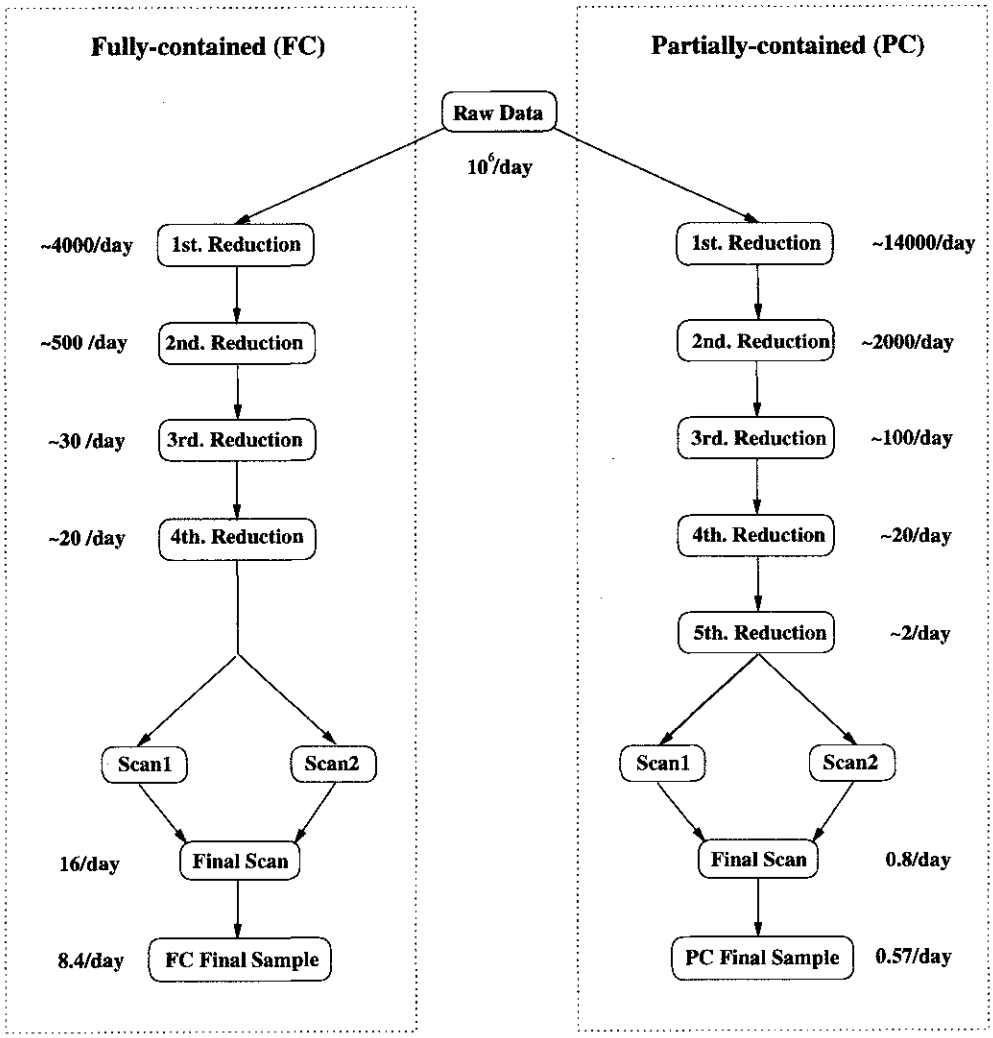

Figure 4.2: Figure of the fully-contained (FC) and partially-contained (PC) reduction steps. Raw data are applied by 4 (5) reduction programs for FC (PC) sample and reduced to 20 (2) events/day until the human scanning.

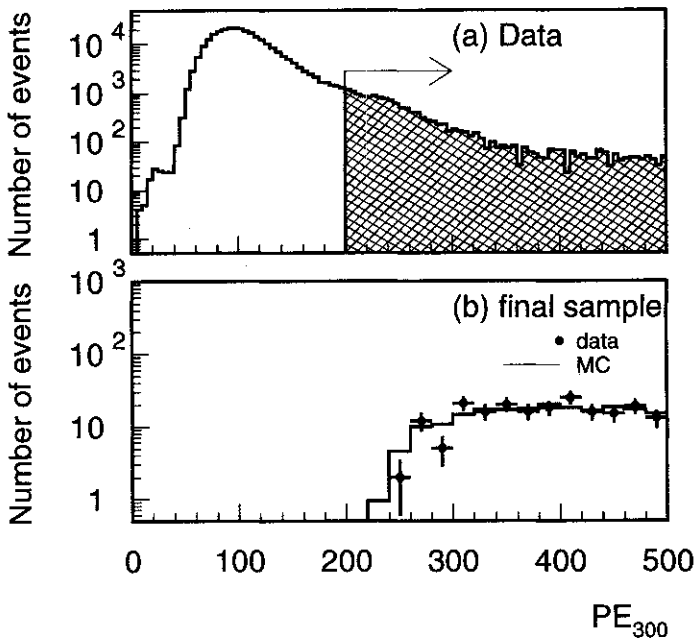

Figure 4.3: PE_{300} distribution for (a) data and (b) final sample data and Monte Carlo events (no oscillation). Number of Monte Carlo events in (b) is normalized to that of data.

The PE_{max}/PE_{300} cut removes the low energy events with one large accidental hit. Fig 4.4 shows the PE_{max}/PE_{300} distribution for data, atmospheric neutrino Monte Carlo events and final sample, whose vertex position is at least 1.5 m away from the inner detector wall. Fig 4.4 indicates that the $PE_{max}/PE_{300} < 0.5$ cut is safe enough for the atmospheric neutrino events.

Fig 4.5 shows the N_{hita} distribution in data, atmospheric Monte Carlo events and final sample. because of no energy deposit in the outer detector. The $N_{hita} < 25$ cut is safe for the fully-contained events. Most of the cosmic-ray muons are rejected by these N_{hita} cuts.

The event rate after the 2nd reduction is about 400 events per day.

4.1.3 3rd reduction for FC sample

Most of the background have been removed by the 2nd reduction, but the backgrounds which often occur in some specific cases still remain. The 3rd reduction is provided to reject such events by the further intelligent but CPU-power-consuming algorithm.

The 3rd reduction consists of the following 6 cuts:

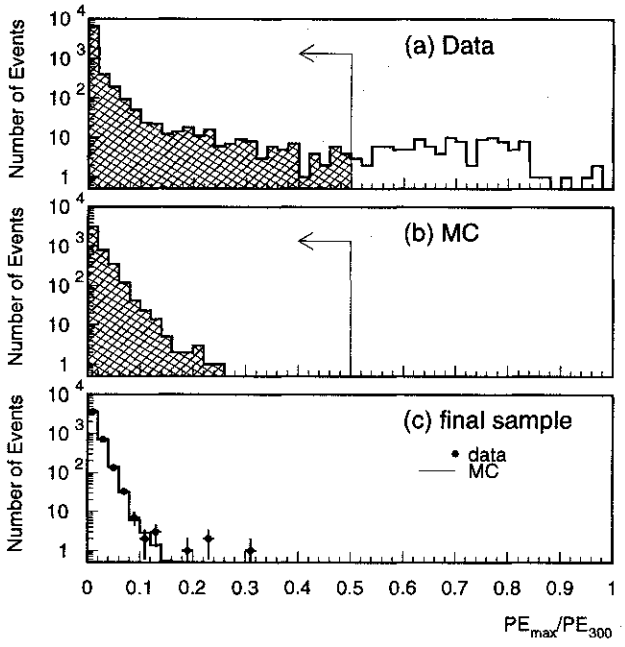

Figure 4.4: PE_{max}/PE_{300} distribution for (a) data, (b) atmospheric Monte Carlo events whose vertex is more than 1 m from the detector wall and (c) final sample data and Monte Carlo (no oscillation). Number of Monte Carlo events in (c) is normalized to that of data.

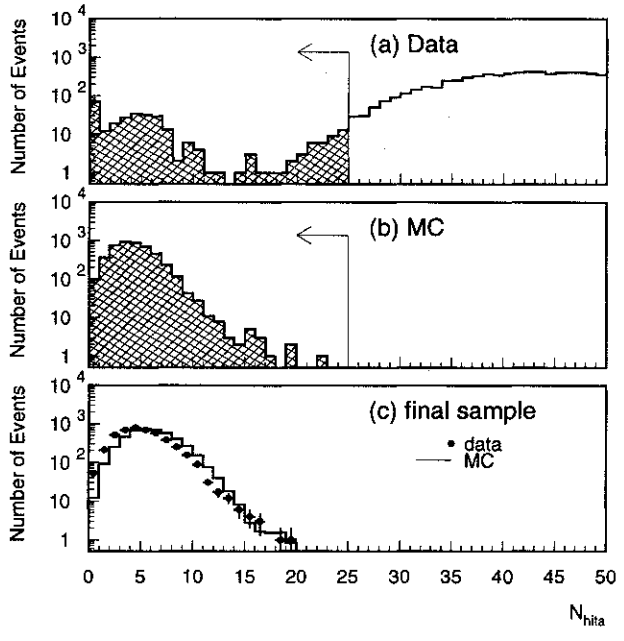

Figure 4.5: N_{hita} distribution for (a) data, (b) atmospheric Monte Carlo events and (c) final sample data and Monte Carlo (no oscillation). Number of Monte Carlo events in (c) is normalized to that of data.

1. through-going muon cut
2. stopping muon cut
3. low energy event cut
4. flashing PMT event cut
5. accidental hits cut
6. cable-hole muon cut

The "through-going" and "stopping" muon cut remove the events with more than 9 OD hits around the entrance or exit point. The entrance and exit points are determined by each special fitters for through-going and stopping muons.

The "low energy event" cut is to reject the remaining low energy events and applied for the events such as less than 500 hits in the inner detector. This cut is based on the parameters calculated in the fitter for the low energy events, which is developed for the solar neutrino analysis. One parameter is "N_{50}", the maximum number of hits within a 50 nsec time window in the time residual (time subtracted by photon's time-of-flight (TOF)). The N_{50} is the good indicator for the low energy events because the number of hits is proportional to the energy of particle in this energy region. Another is the goodness of the vertex fitting, "G_{low}". The definition of the goodness is described in section 6.1. The cut criteria are as follows:

1. the N_{50} should be more than 50, which corresponds to about 10 MeV.
2. G_{low} should be greater than 0.5

If a PMT has a mechanical problem in the dynode structure, the PMT emits light by an internal corona discharge (flashing PMT events), and these events are characterized by its broad time distribution. They are removed by the cut based on the minimum number of hits within 100 nsec time window (N_{min}). This time window is 300 nsec to 900 nsec after the event trigger, which is outside the genuine signal region. If the N_{min} is greater than 15(10) and the number of ID hits is greater(less) than 800, the events are rejected by this cut.

The "accidental hits" events occur when more than two independent particles are observed within the same trigger gate. This kind of events consists of a low-energy particle and an

accidentally following cosmic-ray muon, which is observed in the later region of the trigger gate. Therefore if more than 5000 p.e. for ID and more than 20 hits for OD is observed within 400 nsec to 600 nsec after the event trigger, the events are removed by this cut.

The "cable hole" indicates the hole, through which cables from PMTs are taken out. There are in total 12 cable holes, and 4 of them are located away from the fringe of the tank. The cosmic muons which enter the inner detector through these 4 cable-holes survive in the second reduction sample because of the lower detection efficiency of the OD around there. In order to reject these "cable-hole" muons, plastic scintillation counters, whose size is 2.0 m × 2.5 m, were installed above these cable holes in April 1997. In addition to the hit information of these veto counter, the events are removed only when the vertex position fitted by the muon fitter is less than 4 m from the veto counter.

The event rate after the 3rd reduction is about 30 events per day.

4.1.4 4th reduction for FC sample

The purpose of the 4th reduction is the final rejection of the flashing PMT events. This reduction program uses the charge pattern of the inner detector because the flashing PMT tend to cause the same charge pattern of events repeatedly. The program scans all events which remain after the 3rd reduction and calculate the sum of the PMT charge in each 2 m × 2 m region, which is called as "patch". After that, the patterns are compared between two different events one by one and the goodness of the pattern matching is estimated by the following "R_{match}" value:

$$R_{match} = \frac{1}{n}\sum_{i=1}^{n}\frac{(q_1(i)-\bar{q_1})\times(q_2(i)-\bar{q_2})}{\sigma_{q_1}\times\sigma_{q_2}}$$

where $q_1(i)(q_2(i))$ is the charge sum in the i-th patch for the first and second events, $\bar{q_1}(\bar{q_2})$ and $\sigma_{q_1}(\sigma_{q_2})$ are the average value and deviation of $q_1(q_2)$, respectively. The R_{match} takes the value of less than 1 and the higher value is estimated to be better matched. Events 1 and 2 are said to be "matched" if R_{match} exceeds the threshold. Then the number of matched events (N_{match}) is counted.

Fig 4.6 shows the 2-dimensional plots of "R^{max}_{match}" and N_{match}, where R^{max}_{match} indicates the maximum value of R^{max}_{match} for the event against all the other events. The upper figure shows the distribution for the neutrino sample from which the flashing PMT events are removed by eye-scanning, and the lower shows the flasher-identified events by eye-scanning. A cluster can

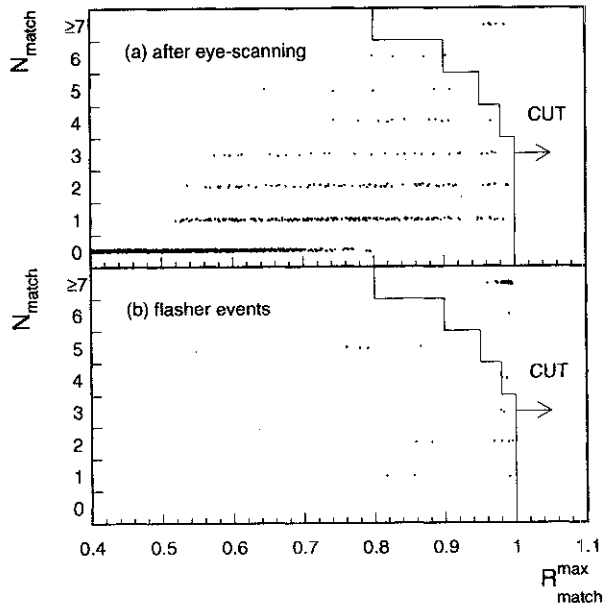

Figure 4.6: R^{max}_{match} vs N_{match} distributions for the eye-scanned events (upper) and flasher-identified events (lower). The events in the right side of solid line is removed by the FC 4th reduction.

be seen in the high R^{max}_{match} region of the lower plot. The events in the right side of the region separated by the solid line are identified as the flashing PMT events. Some events of the neutrino sample are identified as the flasher events ,but all of them are removed by the fiducial volume cut because their vertex is near the detector wall.

The event rate after the 4th reduction is about 20 events per day. The total efficiency of FC reduction is estimated by the atmospheric neutrino Monte Carlo and the probability rejecting the atmospheric neutrino events is less than 0.1 % for the visible energy greater than 30 MeV and within fiducial volume.

4.2 Reduction for partially-contained events

The data reduction for PC sample is completely different from that for FC sample because of the presence of additional hits in the outer detector. A simple criterion based on the number of hit in the outer detector cannot be used and the reduction methods are more complicated than that for FC sample. The main background for PC sample is cosmic-ray muons and 5 steps of reduction shown in Fig 4.2 are applied to remove them. The remaining events after the 5th

reduction are also scanned by the same method as FC sample.

4.2.1 1st reduction for PC sample

The purpose of the 1st reduction for PC sample is to reject through-going cosmic muons as much as possible and keep not only atmospheric neutrino events but also cosmic stopping muons. The reduction criteria in the 1st reduction are as follows:

1. Total number of p.e. in the inner detector should be greater than 1000.
2. The time width in the OD hits (T_{width}) should be less than 240 nsec.
3. The number of cluster in the outer detector (N_{clust}) should be less than or equal to 1.

An exiting particle in the PC sample must have a track length of $\gtrsim$ 2.5 m ,which is the minimum distance from the fiducial volume to the outer detector, corresponding to muons with $\gtrsim$ 700 MeV/c. Therefore this total charge cut is safe enough for PC reduction because the momentum of a muon which emits 1000 p.e. in the inner detector corresponds to 310 MeV/c.

The T_{width} is the time difference between the leading edge and trailing edge, which have more than 15 hits in a 100 nsec time window. The through-going muon have two timing edges in the OD time distribution, corresponding to the entering and exiting time. The T_{width} cut removes through-going muons.

The "cluster" means the special cluster of neighboring hit-PMTs and it indicates the entrance or exit point of cosmic-ray muons. A cluster is formed around PMT which has more than 8 p.e. and the clusters which lie within 8 m are merged. The events which have more than or equal to 2 clusters are rejected because through-going muons have 2 clusters, corresponding to the entrance and exit points.

The event rate after PC 1st reduction is about 14000 events per day.

Fig 4.7 and 4.8 shows the T_{wid} and N_{clust} distribution for data, atmospheric neutrino Monte Carlo events and final sample.

4.2.2 2nd reduction for PC sample

The 2nd reduction is also based on the number of hit PMTs in the outer detector clusters, which is calculated by an algorithm shown in Fig 4.9. Each grid is separated by 10 m $\times$ 10 m size in

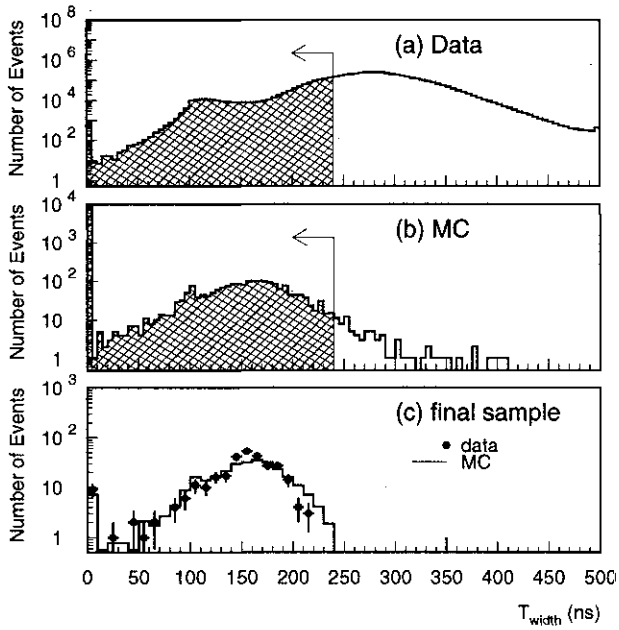

Figure 4.7: T_{width} distribution for (a) data, (b) atmospheric Monte Carlo events whose vertex is more than 1 m from the inner detector wall and (c) final sample data and Monte Carlo (no oscillation). Number of Monte Carlo events in (c) is normalized to that of data.

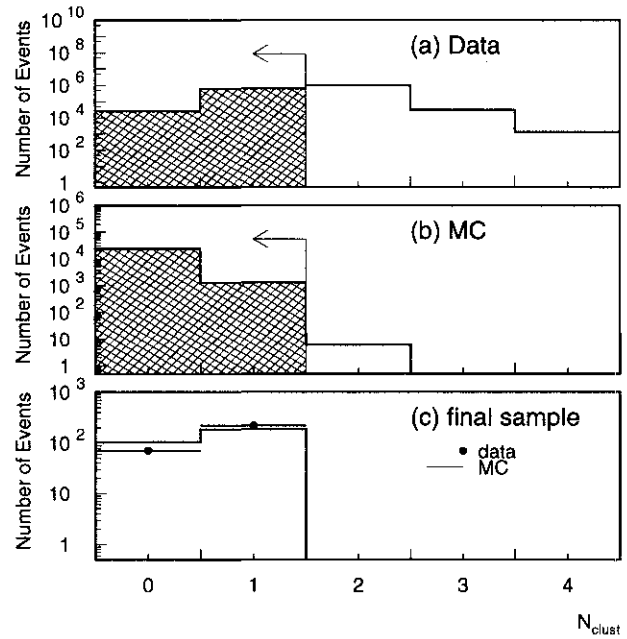

Figure 4.8: N_{clust} distribution for (a) data, (b) atmospheric Monte Carlo events whose vertex is more than 1 m from the inner detector wall and (c) final sample data and Monte Carlo (no oscillation). Number of Monte Carlo events in (c) is normalized to that of data.

the outer detector and the cluster is formed by looking at the charge gradient to the neighboring grids.

In addition to this, the sum of charge in the inner detector cluster which lies behind the outer detector cluster is used for the primary rejection of stopping muons. This is due to the difference of the energy deposit at the entrance point of entering particles and exit point of outgoing particles. The outgoing particles radiate much more photons around the exit point than the entering particles.

The 2nd reduction criteria is as follows:

1. The number of OD cluster which have more than 7 hit PMT should be less than or equal to 1. This cut eliminates through-going muons.

2. The minimum number of hits in the side, top or bottom region for the highest charge OD cluster ($N_{clustmin}$) should be less than 7. This cut eliminates corner clipping muons, which hits OD PMTs in both side and top, or side and bottom regions.

3. For the events whose number of OD cluster is 1, if the sum of charge within 200 cm of the highest charge PMT in the inner cluster closest to the OD cluster (PE_{200}) is less than 1000 p.e., this events is rejected. This cut eliminates stopping muons.

Fig 4.8 and Fig 4.11 show the effects of the 2nd reduction for data, atmospheric neutrino Monte Carlo events and final sample. Fig 4.12 shows the PE_{200} distribution for final sample data and Monte Carlo. The number of hits in the highest charge cluster calculated here (N_{hitac}) is also used in the separation of FC and PC sample. (see section 7.1)

The event rate after PC 2nd reduction is about 2000 event per day.

4.2.3 3rd reduction for PC sample

The purpose of the 3rd reduction is the reduction of the cosmic muons which stops in the inner detector. Since the background level has been reduced sufficiently until this reduction step, the reduction by using automatic fitter is available.

The same algorithm described at the section of FC 3rd reduction is used for the rejection of flashing PMT events (see section 4.1.3). For the stopping muons rejection, the reduction using the vertex fitter, which is modified from PFIT (see section 6.1) is used The entrance position is

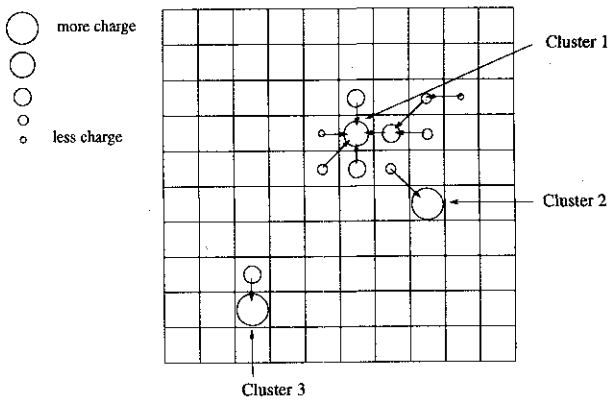

Figure 4.9: Schematic view of the 2nd reduction clustering algorithm. The circles represent the number of charge observed in an angular bin. The larger the radius of the circle, the more charge. The arrows represent the vector charge gradient. The angular bin sizes corresponds to roughly 10 m × 10 m in the outer detector.

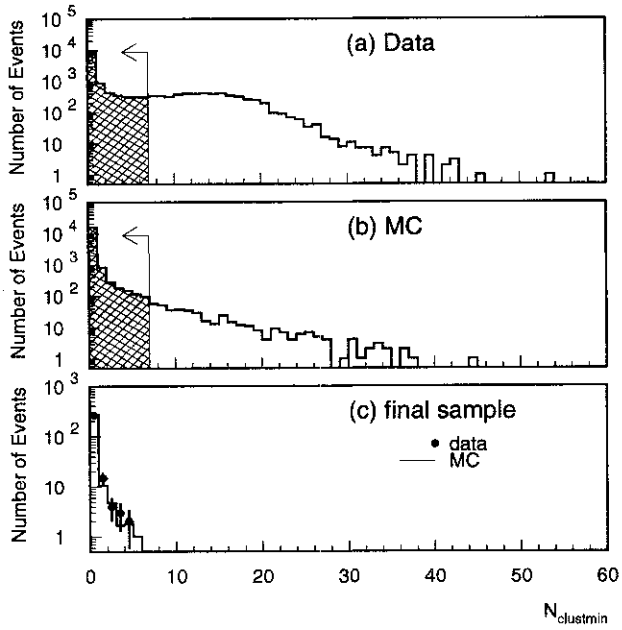

Figure 4.10: $N_{clustmin}$ distribution for (a) data, (b) atmospheric Monte Carlo events and (c) final sample data and Monte Carlo (no oscillation). Number of Monte Carlo events in (c) is normalized to that of data.

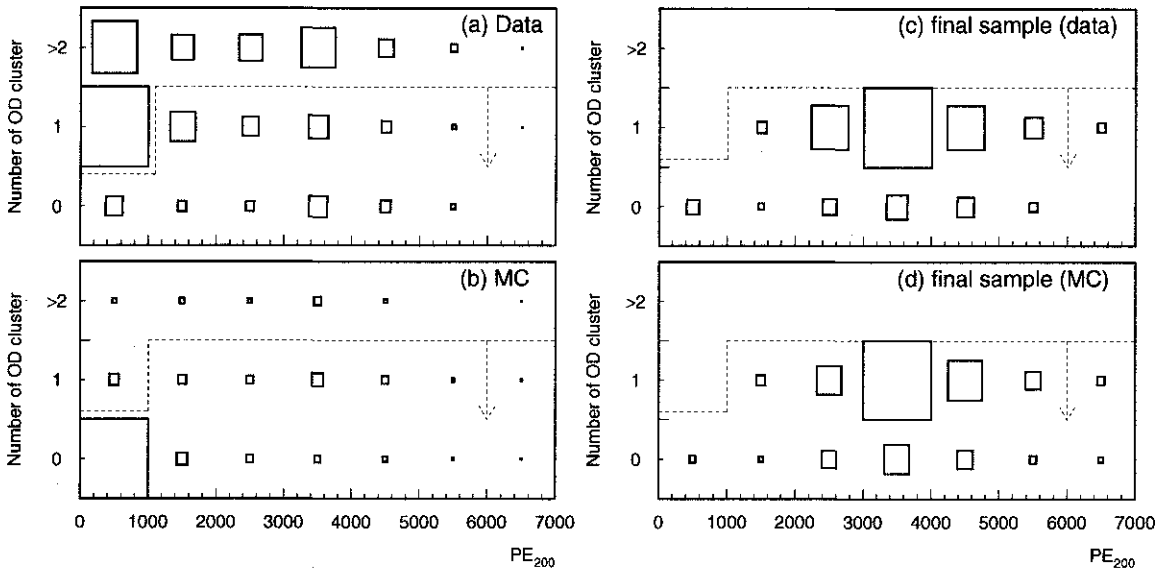

Figure 4.11: 2-dimensional plot of the number of OD cluster and PE_{200} for (a) data, (b) atmospheric neutrino Monte Carlo events, (c) final sample of data and (d) of Monte Carlo events (no oscillation). The size of the box histogram indicates the number of events in the bin. The events below the dashed line are selected for the PC 2nd reduction.

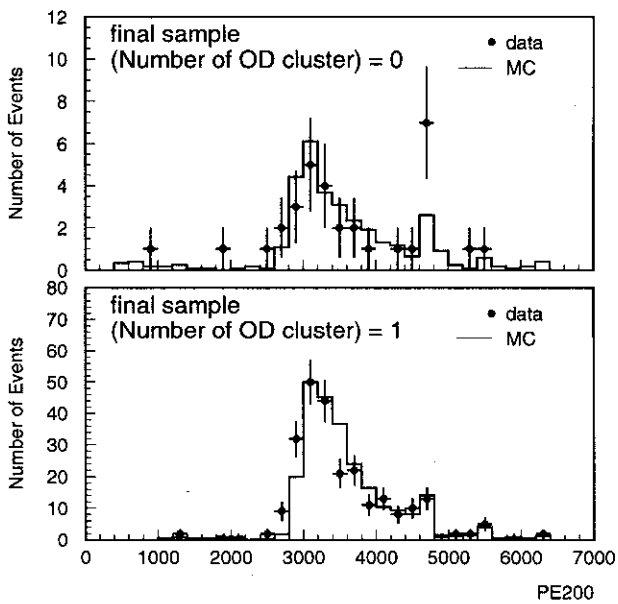

Figure 4.12: PE_{200} distributions in Figpcred2 (c) and (d). Upper (lower) figure shows the events whose number of OD cluster is equal to 0 (1). Points with error bars show data and histograms show Monte Carlo (no oscillation). Number of Monte Carlo events is normalized to that of data.

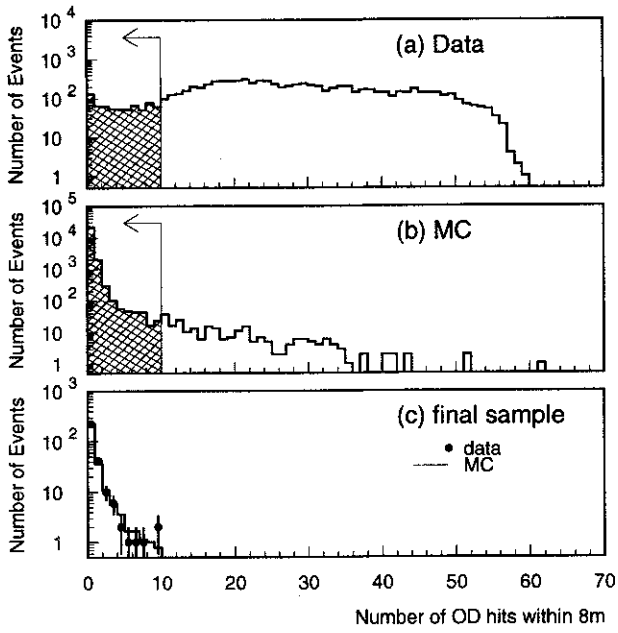

Figure 4.13: Distribution of the number of OD hits within 8 m of the entrance position for (a) data, (b) atmospheric neutrino Monte Carlo events and (c) final sample data and Monte Carlo (no oscillation). Number of Monte Carlo events in (c) is normalized to that of data.

estimated by back-extrapolating from the fitted vertex and direction. The 3rd reduction requires less than 10 OD hits within a 8 m of the entrance position in the outer detector because the atmospheric neutrino event has no cluster in the entrance position.

Fig 4.13 shows the number of hits in the entrance position for the data, atmospheric neutrino Monte Carlo events and final sample. The event rate after PC 3nd reduction is about 100 event per day.

4.2.4 4th reduction for PC sample

The 4th reduction attempts to remove cosmic-ray muons which pass the 3rd reduction due to the inefficiency of the outer detector. The inefficiency of the outer detector in these events is due to the cable bundles, lack of OD PMT coverage and dead PMTs.

Two vertex fitter are applied in this reduction step and the reduction is done according to the reconstructed vertex and direction. One is PFIT, which is also used in the 3rd reduction

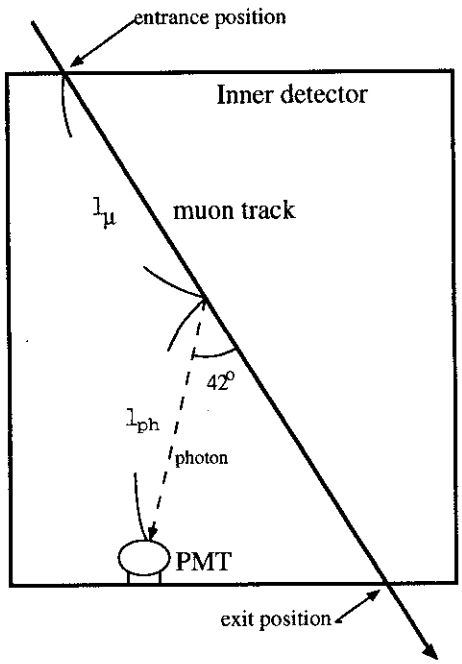

Figure 4.14: Definition of l_μ and l_{ph} for through-going muon fitter. l_μ is the muon flight length from the entrance position to the emission position, and l_{ph} is the phon flight length from the emission position to hit-PMT.

and another is through-going muon fitter. The through-going muon fitter was developed to reconstruct the track of the through-going cosmic-ray muon. The muon fitter finds the entrance and exit positions. The entrance position is defined by the position of the earliest inner hit-PMT with more than two neighboring hit-PMTs. The exit position is defined by the center position of hit-PMTs whose charge is saturated (greater than 231p.e.). Furthermore, a precise determination of the exit position using a goodness of fit is done. The goodness is calculated using the timing information of PMT and the exit position is determined so as to maximize the following goodness:

$$\text{goodness} = \frac{1}{\sum \frac{1}{\sigma_i^2}} \times \sum_i \frac{1}{\sigma_i^2} \exp\left\{-\frac{1}{2}\left(\frac{t_i - T_{ent}}{1.5\sigma_i}\right)^2\right\}$$

$$t_i = T_i - \frac{l_\mu}{c} - \frac{n}{c} l_{ph}$$

where T_{ent} is the entering time of muon, σ_i is the PMT timing resolution ($\sim$3 nsec), T_i is time of i-th hit-PMT, c is light velocity, n is the reflective index of water. l_μ and l_{ph} are the flight length of muon and photon for i-th PMT, as shown in Fig 4.14.

Fig 4.15 shows the event display of typical through-going muon event. The track length of through-going is defined as the distance between the entrance and exit positions. In case of

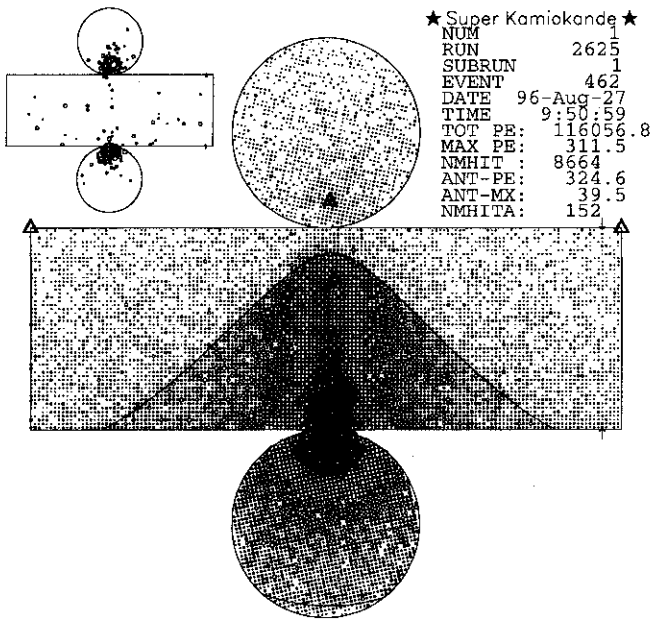

Figure 4.15: Event display of typical through-going muon event. Cross point of four triangle marks shows the reconstructed entrance position.

the partially-contained neutrino events, the muon fitter cannot find the vertex position precisely because the real vertex is not on the inner detector wall. Therefore, the goodness becomes worse than that of through-going muon event.

The 4th reduction consists of the following 3 cuts.

1. From the vertex position determined by PFIT, if PFIT direction ($\vec{d}_{PFIT}$) and the direction to the "earliest" and charge-saturated PMT ($\vec{d}_{PMT}$) is opposite, ($\vec{d}_{PFIT} \cdot \vec{d}_{PMT} < -0.8$), the event is rejected.

2. If the goodness of the through-going muon fitter is greater than 0.85, and if the estimated muon track length by the entrance and exit point is greater than 30 m, the event is rejected. This cut is aimed to eliminates through-going muons.

3. The distance of vertex position from the detector fringe (DCORN) must be greater than 150 cm. This cut is aimed to eliminates corner-clipping muons.

Fig 4.16 and Fig 4.17 shows the effect of each cut for data, atmospheric neutrino Monte Carlo events and final sample. The event rate after PC 4th reduction is about 20 events per day.

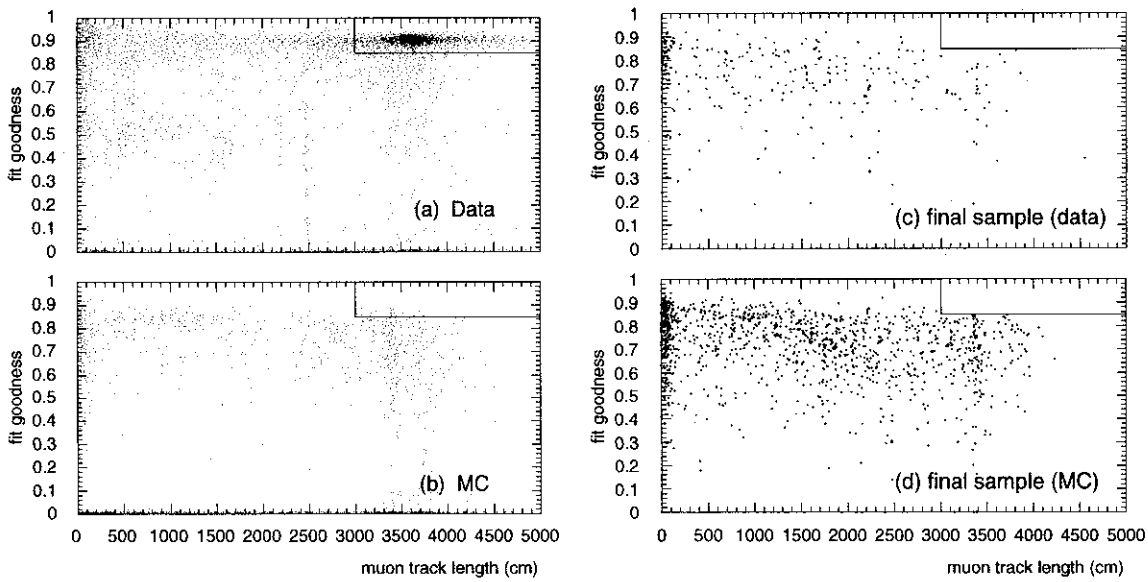

Figure 4.16: Distribution of muon track length and muon fitter goodness for (a) data, (b) atmospheric neutrino Monte Carlo events and (c) final sample data and Monte Carlo (no oscillation). The events in the upper-right region are rejected by this cut.

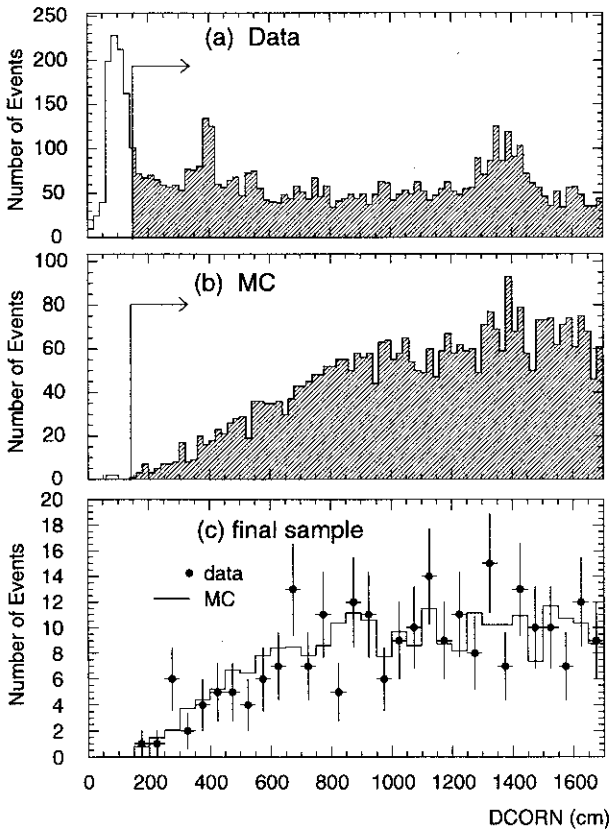

Figure 4.17: Distribution of the distance of vertex from the detector fringe (DCORN) for (a) data, (b) atmospheric neutrino Monte Carlo events and (c) final sample data and Monte Carlo (no oscillation). Number of Monte Carlo events in (c) is normalized to that of data.

4.2.5 5th reduction for PC sample

The 5th reduction is based on the number of hits in the back-extrapolated entrance point. It is similar to the 3rd reduction, but instead of PFIT, the more precise and time-consuming vertex-position fitting is used for the determination of vertex. If the number of OD hits in the extrapolated entrance point is greater than 10, the event is rejected. The event rate after PC 5th reduction is about 2 events per day. The total efficiency of PC reduction is estimated to be 88 % using the atmospheric neutrino Monte Carlo events in the fiducial volume.

4.3 Scanning

The event rate after all of FC (PC) reductions is 20 (2) events per day. But some backgrounds such as cosmic muons and flashing PMT events still remain. In order to remove them, physicists scan the data with a visual display and classify events one by one. Two independent scanners are assigned for one data set so as not to miss neutrino events (double scanning). At the same time scanners check the data quality from the electronics status and the event rate, and if they find any problem in the scanning run(subrun), these are regarded as bad-runs(subrun-s) and these data are removed from the final sample and livetime calculation. The event rate after scanning is 16 (0.6) events per day for FC (PC) sample.

After the double scanning, the final scanners, who are grouped by two experienced scanners, check the consistency of the classifications by two scanner (final scanning) and make the final FC and PC data sample. The scanning efficiency is estimated to be $\geq$99 % for the events in the fiducial volume.

The precise livetime is necessary for the calculation of neutrino event rate. The livetime are estimated for each subrun and summed up for the good subruns of FC and PC samples. The pedestal data-taking time and the electronics dead time are removed from the livetime. The livetimes of the FC and PC final samples presented in this thesis are calculated to be both 535 days.

Chapter 5

Monte Carlo simulation

The Monte Carlo simulation is necessary for the precise observation of the atmospheric neutrinos. It can show us the expectation including all of the complicated factor, such as neutrino flux, interactions, particle tracking and so on, and this expectation is important to examine the neutrino oscillation and determine the oscillation parameters.

In this section, the methods of Monte Carlo simulation used in the atmospheric neutrino analysis are presented.

5.1 Atmospheric neutrino flux

Atmospheric neutrino fluxes have been calculated by several models, Honda et al [29, 30], Gaisser et al [31], Barr et al [32], Bugaev and Naumov [33] and Lee and Koh [34].

We adopt the flux calculated by Honda et al [30], which is employed by a full Monte Carlo method at low energies (30 MeV $\sim$ 3 GeV) and a hybrid method at high energies (1 $\sim$ 3000 GeV).

In the Monte Carlo method, the nucleus and the primary energy of cosmic ray are sampled according to its energy spectrum and rigidity cutoff, and put into the propagation program which simulates the interaction, decay and energy loss of the particles in the atmosphere. The muon polarization is also taken into account. It employs a one-dimensional approximation in which all the secondary particles and the neutrinos keep the direction of their parent cosmic rays.

The calculation in the hybrid method is based on the ν-yield function for nucleon, $\eta_\nu^N(E, E_\nu, \theta)$,

which denotes the number of neutrino in the energy region from E_ν to $E_\nu + dE_\nu$, created by a nucleon with energy of E incident from the zenith angle θ. The η_ν^N is calculated by a Monte Carlo method. The atmospheric neutrino flux is obtained by integrating this function with the energy spectrum of the nucleon flux. The flux obtained this way is connected smoothly to the flux below 3 GeV, which is calculated by the Monte Carlo method.

The uncertainty of the atmospheric neutrino flux is estimated to be 20% at 100 MeV and 15% at 1-100 GeV, but for the $(\nu_\mu + \bar{\nu}_\mu)/(\nu_e + \bar{\nu}_e)$ flavor, it is estimated to be $< 5\%$ because the ambiguity in the absolute flux is cancelled out by taking the ratio.

5.2 Neutrino interaction

Atmospheric neutrinos interact with nucleons and electrons in water via charged current (CC) and neutral current (NC) weak interactions. However neutrino interaction with an orbital electron is negligible because the cross section with an electron is about 1000 times smaller than that with a nucleon at the energy region of atmospheric neutrinos.

For the atmospheric neutrino simulation, the following interactions are taken into account:

1. CC quasi-elastic scattering $\nu N \to l N'$
2. NC elastic scattering $\nu N \to \nu N$
3. CC single-pion production $\nu N \to l N' \pi$
4. NC single-pion production $\nu N \to \nu N' \pi$
5. CC multi-pion production $\nu N \to l N' m\pi (m \geq 1)$
6. NC multi-pion production $\nu N \to \nu N' m\pi (m \geq 1)$
7. CC coherent pion production $\nu\,^{16}\mathrm{O} \to l^{\pm}\,^{16}\mathrm{O}\pi^{\mp}$
8. NC coherent pion production $\nu\,^{16}\mathrm{O} \to \nu\,^{16}\mathrm{O}\pi^{0}$

where N shows a nucleon and l shows a charged lepton. Early version of these interaction programs are developed for the background estimation of the proton decay analysis in Kamiokande experiment [35] and inherited with various modifications.

5.2.1 Quasi-elastic scattering

About 60 % of the atmospheric neutrinos at 1 GeV interacts with nucleons via CC quasi-elastic scattering. One charged lepton is produced via this interaction and we intent to observe these events for the fully-contained analysis because the identification of the charged lepton informs us the incident neutrino flavor. Therefore the simulation of this interaction is especially important.

The cross section is calculated based on the standard V-A (Vector and Axial-vector) theory and it depends on the q^2 value (4-momentum transfer). The q^2-dependence of the cross section can be expressed in terms of the hadronic current [36]:

$$< N'|J^t_{had}|N >= \cos\theta_c \bar{u}(N') \left[\gamma_\lambda F_V^1(q^2) + \frac{i\sigma_{\lambda\nu}q^\nu \xi F_V^2(q^2)}{2M_N} + \gamma_\lambda\gamma_5 F_A(q^2) \right] u(N)$$

where $\cos\theta_c$ is the Cabibbo angle, M_N is a nucleon mass and F_V^1, F_V^2 and F_A are the vector and axial-vector form factors expressed as follows:

$$F_V^1(q^2) = \left(1 - \frac{q^2}{4M^2}\right)^{-1} \left[G_E^V(q^2) - \frac{q^2}{4M^2} G_M^V(q^2) \right],$$

$$\xi F_V^2(q^2) = \left(1 - \frac{q^2}{4M^2}\right)^{-1} \left[G_M^V(q^2) - G_M^E(q^2) \right],$$

$$G_E^V(q^2) = \frac{1}{\left(1 - \frac{q^2}{M_V^2}\right)^2}, \quad G_M^V(q^2) = 1 + \frac{\xi}{\left(1 - \frac{q^2}{M_V^2}\right)^2}, \quad \xi \equiv \mu_p - \mu_n = 3.71,$$

$$F_A(q^2) = \frac{-1.23}{\left(1 - \frac{q^2}{M_A^2}\right)^2}$$

where M_V and M_A are the vector and axial-vector mass and are taken to be 0.84 and 1.01, respectively, according to Ref [37].

In case of the reaction with nucleons in oxygen, the effects of the Fermi motion and the Pauli blocking are considered. The Fermi momentum distribution is estimated from the $e - {}^{12}$C scattering experiment. The Fermi gas model is adopted to simulate the Pauli blocking and momentum of a recoil nucleon is restricted to be larger than the Fermi surface momentum (250 MeV/c).

Fig 5.1 shows the total cross section of $\nu_\mu n \to \mu^- p$ and $\bar{\nu}_\mu p \to \mu^+ n$ with $M_A = 1.01 \pm 0.10$, compared with the experimental data. They are consistent within 10% uncertainty of M_A.

The scattered angle of the lepton, which is determined by the q^2 value, depends strongly on the incident neutrino energy and affects the zenith angle distribution of lepton direction. Fig 5.2 shows the scattered angle of muons as a function of neutrino energy in $\nu_\mu d \to \mu^- pp$ reaction. Our simulation and the experimental data measured by the BNL 7-foot bubble chamber experiment [39] are shown and agree well each other.

We also consider the neutral current elastic interactions, most events of which are invisible with our detector. The total cross section is estimated by the following ratio of NC to CC cross section according to Ref [43, 44]:

$$\begin{aligned}
\sigma(\nu p \to \nu p) &= 0.153 \times \sigma(\nu p \to e^- p) \\
\sigma(\bar{\nu} p \to \bar{\nu} p) &= 0.218 \times \sigma(\bar{\nu} p \to e^+ n) \\
\sigma(\nu n \to \nu n) &= 1.5 \times \sigma(\nu p \to \nu p) \\
\sigma(\bar{\nu} n \to \bar{\nu} n) &= 1.0 \times \sigma(\bar{\nu} p \to \bar{\nu} p)
\end{aligned}$$

5.2.2 Single pion production

The single pion production is dominant next to the quasi-elastic interaction in the energy range of less than 1 GeV. Neutrinos produce one lepton and one pion via the following interactions:

$$\text{Charged current} \begin{cases} \nu p \to l^- p\pi^+ & \bar{\nu} n \to l^+ n\pi^- \\ \nu n \to l^- p\pi^0 & \bar{\nu} p \to l^+ n\pi^0 \\ \nu n \to l^- n\pi^+ & \bar{\nu} p \to l^+ p\pi^- \end{cases}$$

$$\text{Neutral current} \begin{cases} \nu p \to \nu p\pi^0 & \bar{\nu} p \to \bar{\nu} p\pi^0 \\ \nu p \to \nu n\pi^+ & \bar{\nu} p \to \bar{\nu} n\pi^+ \\ \nu n \to \nu n\pi^0 & \bar{\nu} n \to \bar{\nu} n\pi^0 \\ \nu n \to \nu p\pi^- & \bar{\nu} n \to \bar{\nu} p\pi^- \end{cases}$$

The simulation of these interactions are based on the Rein-Sehgal's model [45]. In this model, the interaction is calculated through the following two part:

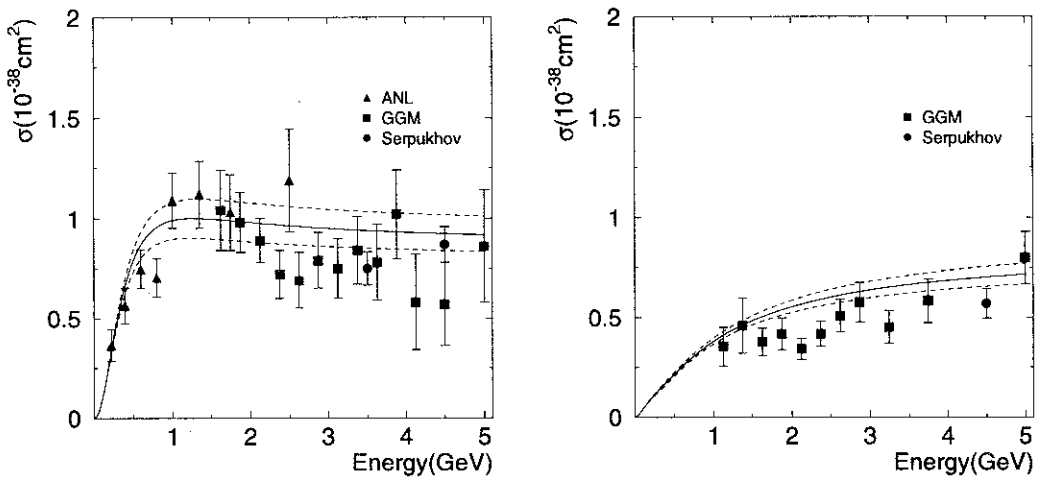

Figure 5.1: Calculated total cross sections of $\nu_\mu n \to \mu^- p$ (left) and $\bar{\nu}_\mu p \to \mu^+ n$ (right) compared with the experimental data, ANL [40], GGM [41] and Serpukhov [42]. Upper and lower dashed lines show the cross section with $M_A = 1.11$ and 0.91, respectively

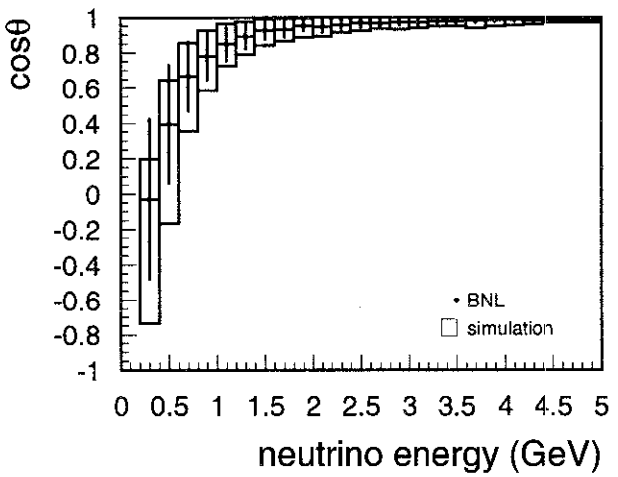

Figure 5.2: Scattered angle of lepton in $\nu_\mu d \to \mu^- pp$ reaction as a function of neutrino energy. Data with error bar shows the result measured by BNL 7-boot bubble chamber [39] and square histogram is obtained by our simulation.

$$\begin{aligned} \nu + N &\rightarrow l + N^* \\ N^* &\rightarrow \pi + N' \end{aligned}$$

where N^* is the baryon resonance, for which $\Delta(1232)$ and other 17 states of resonance below 2 GeV/c^2 are taken into account, including interferences among them. If this interaction occurs via one resonance state, the differential cross section $d^2\sigma/dq^2dE$ is expressed as follows:

$$\frac{d^2\sigma}{dq^2 dE_\nu} = \frac{1}{32\pi M_N E_\nu^2} \cdot \frac{1}{2} \cdot \sum_{spins} |T(\nu N \rightarrow lN^*)| \cdot \chi_{E_\nu} \cdot \delta(W^2 - M^2)$$

where

E_ν	neutrino energy
M_N	nucleon mass
W	invariant mass of πN system
M	invariant mass of resonance
$T(\nu N \rightarrow lN^*)$	amplitude of resonance
χ_E	decay probability of resonance

The total cross section is obtained by integrating the above equation with q^2 and E_ν. We restricted that the invariant mass W to be less than 1.4 GeV/c^2 because multi pion production is dominant at $W > 1.4$GeV/c^2. Fig 5.3 and Fig 5.4 shows the total cross sections for charged current and neutral current interactions, compared with the experimental data. The calculated cross sections agree well with the experimental data.

The angular distribution of pion from $\Delta(1232)$ resonance is also calculated using this model. However, for other resonances, it is assumed to be isotropic in the rest frame of the πN system.

5.2.3 Multi pion production

Multi pion production indicates the interaction that produces more than one pion with the invariant mass of hadronic system W being larger than 1.4GeV/c^2. The cross section and kinematics of multi pion production is calculated under the assumption of Bjorken scaling. The differential cross section with Bjorken scaling parameter is expressed as follows:

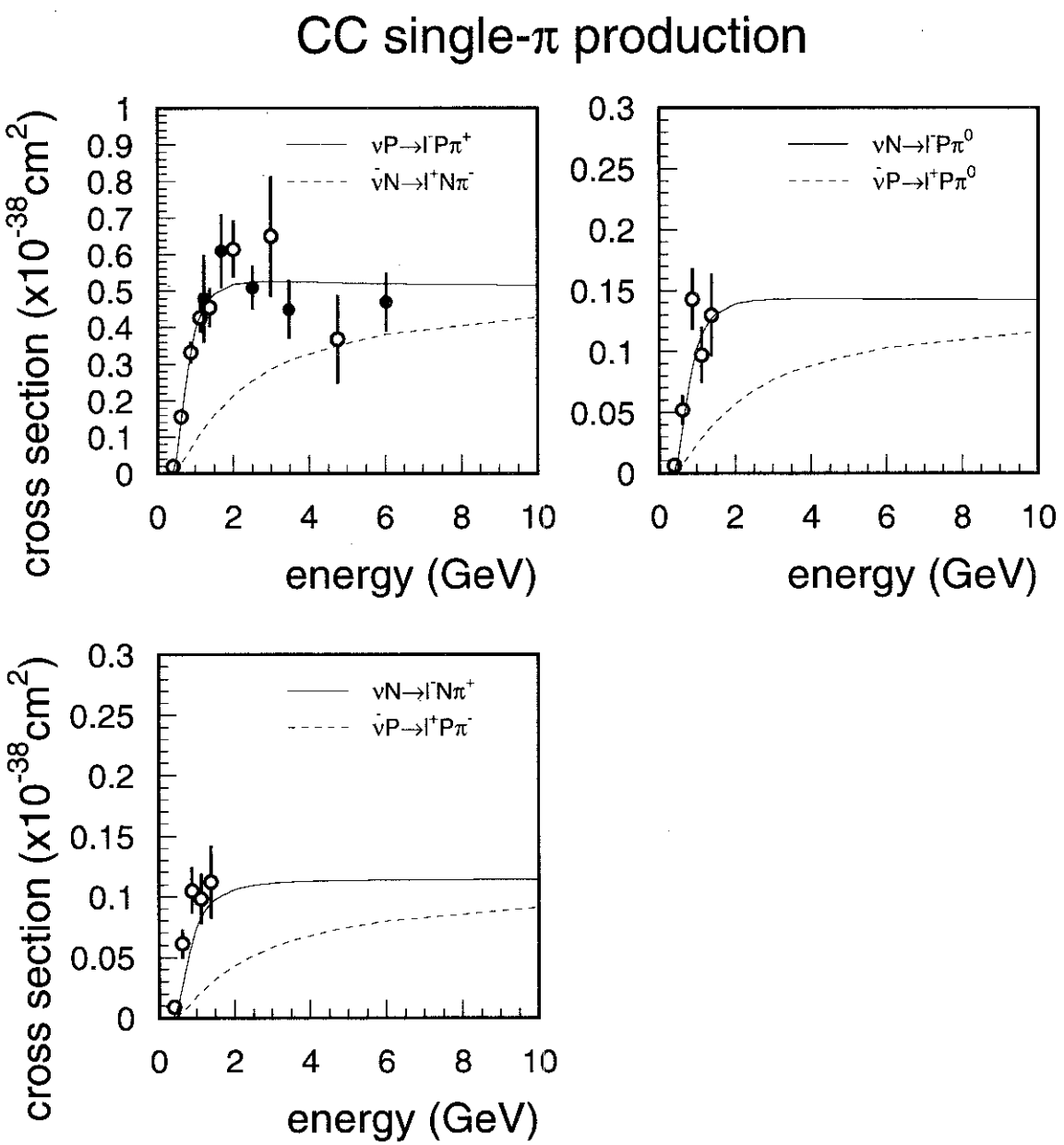

Figure 5.3: Calculated cross section of charged current single-π production.

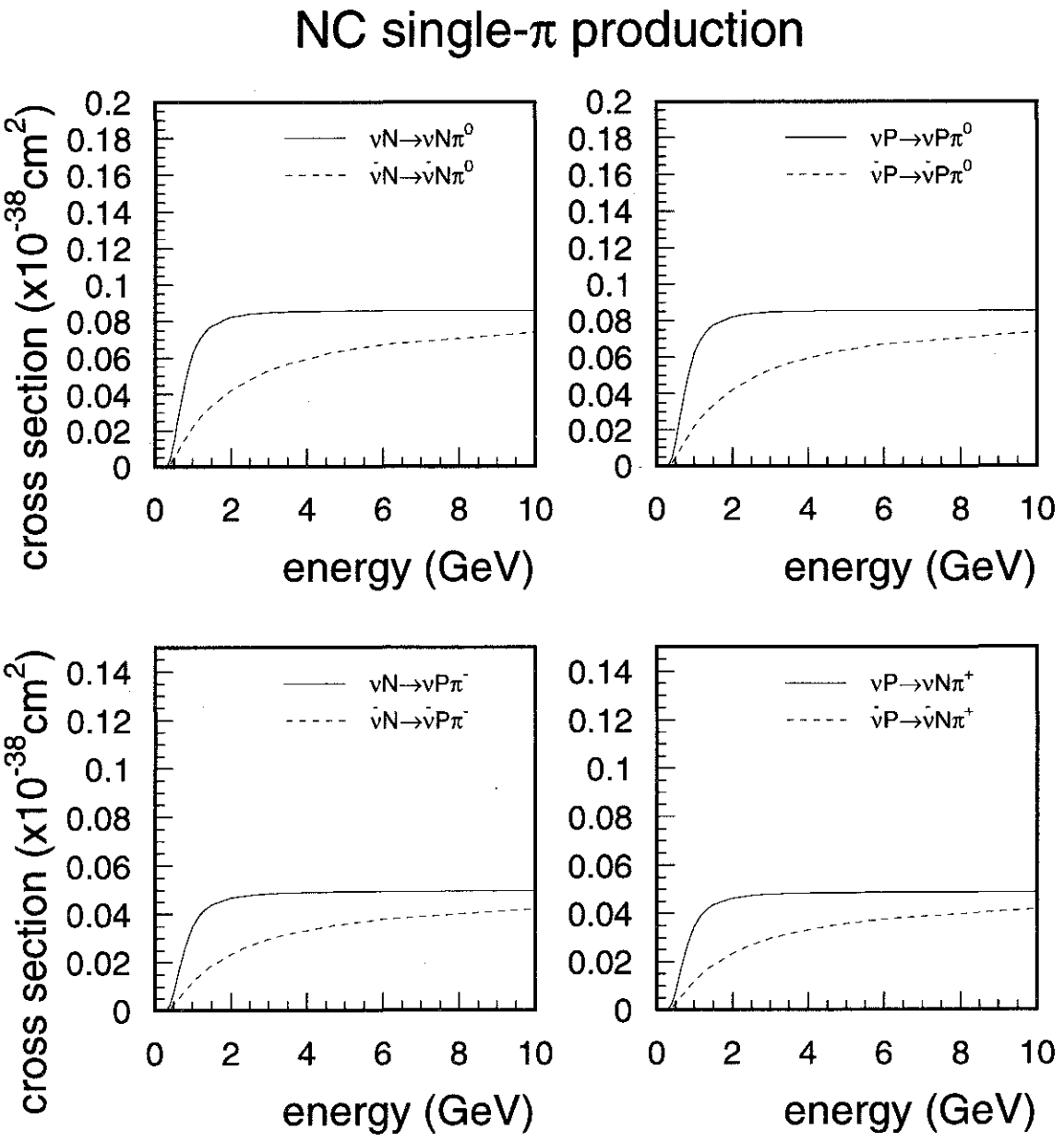

Figure 5.4: Calculated cross section of neutral current single-π production.

$$\frac{d^2\sigma^{\nu,\bar{\nu}}}{dxdy} = \frac{G_F^2 M_N E_\nu}{\pi} \cdot \left\{ (1 - y + \frac{1}{2}y^2 + C_1)F_2(x) \pm y(1 - \frac{1}{2}y + C_2)\,[xF_3(x)] \right\}$$

where

$$C_1 = \frac{m^2(y-2)}{4M_N E_\nu x} - \frac{M_N xy}{2E_\nu} - \frac{m^2}{E_\nu^2}$$

$$C_2 = -\frac{m^2}{4M_N E_\nu x}$$

G_F	Fermi constant
M_N	nucleon mass
E_ν	neutrino energy
m	lepton mass
E_l	lepton energy
x	Bjorken scaling parameter ($= -q^2/(2M(E_\nu - E_l) + M^2)$)
y	Bjorken scaling parameter ($= (E_\nu - E_l)/E_\nu$)

$F_2(x)$ and $F_3(x)$ are taken from the CCFR experimental result [47]. The total cross section for charged current is obtained by integrating the above function with a constraint of $W > 1.4\mathrm{GeV/c}^2$ and is shown in Fig 5.5.

The mean multiplicity of charged pions $\langle n_c \rangle$ is measured to be $(0.06 \pm 0.06) + (1.22 \pm 0.03) \ln W^2$ by the Fermilab 15-foot hydrogen bubble chamber experiment [48]. From this measurement, we estimated the mean multiplicity including neutral pion $\langle n_\pi \rangle$ under the assumption of $\langle n_{\pi^+} \rangle = \langle n_{\pi^-} \rangle = \langle n_{\pi^0} \rangle$ and $\langle n_{\pi^+} \rangle = 1/2\langle n_c \rangle$ as follows:

$$\langle n_\pi \rangle = 0.09 + 1.83 \ln W^2$$

To determine the pion multiplicity for individual events, KNO (Koba-Nielsen-Olesen) scaling which reproduce BEBC data [49] for the process $\nu_\mu P \to \mu X^{++}$ is adopted. The charge of each hadron is randomly chosen under the constraint of the total charge conservation. The effect of Δ resonance in the final state is considered in the decay of hadron system because the result of the Argonne bubble chamber experiment shows a clear signal of Δ in the multi-hadron final

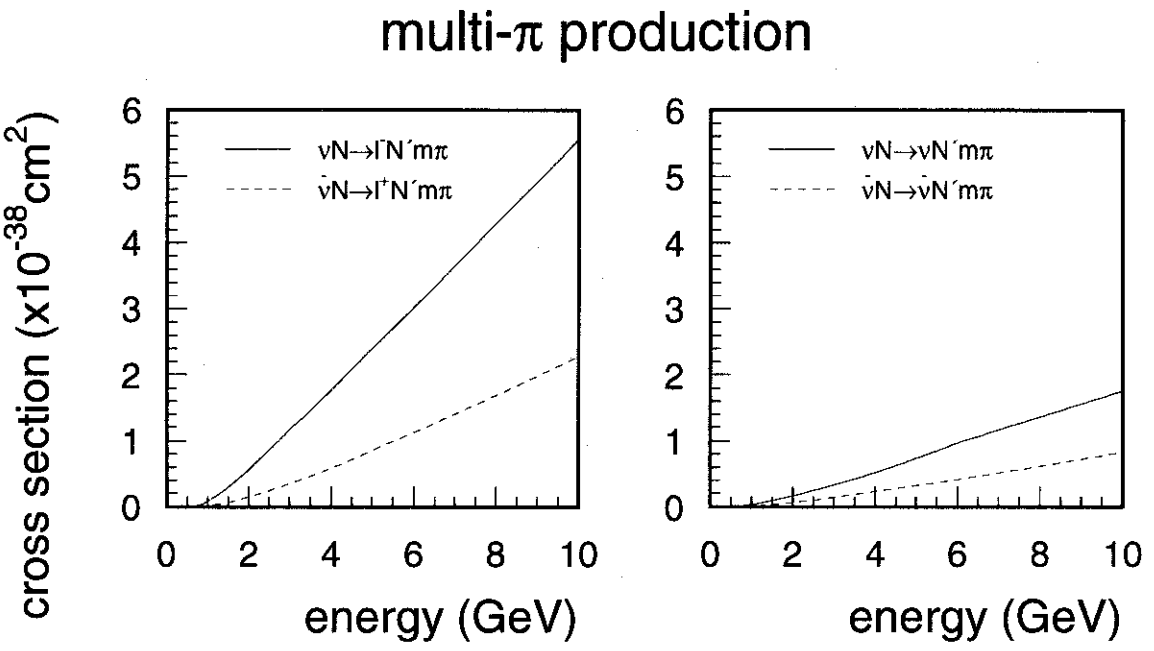

Figure 5.5: Calculated cross section of multi-π production interaction.

states [50]. The forward-backward multiplicity asymmetry measured by the BEBC data is also taken into account to be $\langle n_\pi^F \rangle / \langle n_\pi^B \rangle = (0.35 + 0.41 \ln W^2)/(0.50 + 0.09 \ln W^2)$.

For neutral current interaction, the ratio of CC and NC cross section is estimated by the Ref [51] ($E_\nu < 3$GeV) and Ref [52] ($E_\nu > 3$GeV).

$$\frac{\sigma(\nu N \to \nu X)}{\sigma(\nu N \to l^- X)} = \begin{cases} 0.26 & (E_\nu < 3 \text{ GeV}) \\ 0.26 + 0.04(E_\nu/3 - 1) & (3 \text{ GeV} < E_\nu < 6 \text{ GeV}) \\ 0.30 & (E_\nu > 6 \text{ GeV}) \end{cases}$$

$$\frac{\sigma(\bar{\nu} N \to \bar{\nu} X)}{\sigma(\bar{\nu} N \to l^+ X)} = \begin{cases} 0.39 & (E_\nu < 3 \text{ GeV}) \\ 0.39 + 0.02(E_\nu/3 - 1) & (3 \text{ GeV} < E_\nu < 6 \text{ GeV}) \\ 0.37 & (E_\nu > 6 \text{ GeV}) \end{cases}$$

5.2.4 Coherent pion production

Coherent pion production is a coherent interaction of neutrino with a nucleus as a whole. This interaction produces one pion of the same charge as the incoming weak current, therefore the following 3 types of interactions are considered:

$$\begin{aligned}
\bar{\nu}\mathcal{N} &\rightarrow l^+\mathcal{N}\pi^- \\
\nu\mathcal{N} &\rightarrow l^-\mathcal{N}\pi^+ \\
\nu\mathcal{N} &\rightarrow \nu\mathcal{N}\pi^0, \quad \bar{\nu}\mathcal{N} \rightarrow \bar{\nu}\mathcal{N}\pi^0
\end{aligned}$$

where $l^\pm$ is a charged lepton and $\mathcal{N}$ is a nucleus. Coherent pion production is characterized by an angular distribution of pion that is more sharply peaked in the forward direction than the incoherent and resonant interactions. The nucleus does not break up in this reaction due to a negligible amount of energy transfer to it.

The calculation of the cross section and kinematics is based on the Rein-Sehgal model [53]. In this model, the coherent process is described by the dominant process of the isovector axial current and the contribution from the vector current is neglected. Therefore the cross section for neutrino and anti-neutrino can be approximated to be equal.

The differential cross section is expressed as follows by using Adler's PCAC (partially conserved axialvector current) theory [57]:

$$\frac{d^3\sigma}{dxdyd|t|} = \frac{G_F^2 M_N E_\nu}{\pi^2}\frac{1}{2}f_\pi^2(1-y)\left.\frac{d\sigma(\pi\mathcal{N}\rightarrow\pi\mathcal{N})}{d|t|}\right|_{E_\pi=E_\nu y}\left(1+\frac{Q^2}{M_A^2}\right)^{-2}$$

x	Bjorken scaling parameter ($= Q^2/2M_E(E_\nu - E_l)$)
y	Bjorken scaling parameter ($= (E_\nu - E_l)/E_\nu$)
t	momentum transfer to the nucleus ($= (p_\pi - q)^2$)
G_F	Fermi constant
M_N	nucleon mass
E_ν	neutrino energy
E_l	lepton energy
f_π	pion decay constant

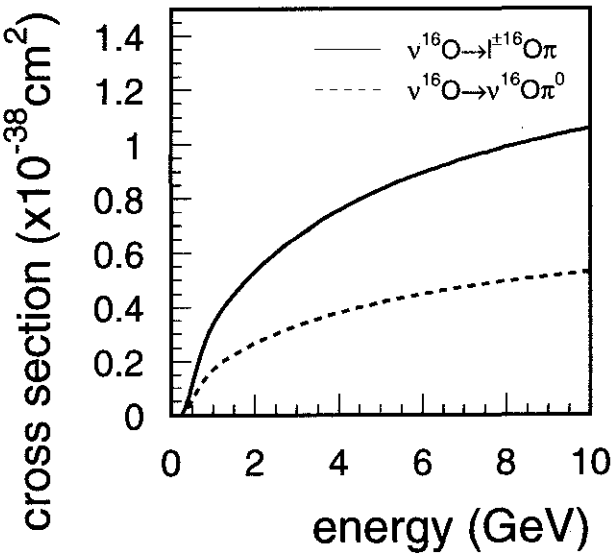

Figure 5.6: Calculated cross section of coherent π production off ^{16}O nuclei.

The pion-nucleus differential cross section $d\sigma(\pi\mathcal{N} \to \pi\mathcal{N})/d|t|$ is approximated to $A^2|F_{\mathcal{N}}(t)|^2[d\sigma(\pi N \to \pi N)/d|t|]_{t=0}$, where A is the number of nucleons in the nucleus, $F_{\mathcal{N}}(t)$ is the nuclear form factor and $[d\sigma(\pi N \to \pi N)/d|t|]_{t=0}$ is the pion-nucleon differential cross section in the forward direction.

Fig 5.6 shows the total cross section of coherent pion production off ^{16}O, for charged current and neutral current as a function of neutrino energy.

Table 5.1 shows the measured total cross section by the accelerator experiments, compared with the expected value calculated by the Rein-Sehgal method. The calculation agrees well with the experimental data.

5.3 Meson nuclear effect

Mesons, especially pions, produced in a ^{16}O nucleus often make secondary interactions before leaving the nucleus. In our Monte Carlo simulation, the following nuclear interactions for pions are considered: inelastic scattering, absorption and charge exchange.

For the density of the nucleus, the following function of Woods-Saxon model is adopted:

$$\rho(r) = \frac{Z}{A}\bar{\rho}\left\{1 + \exp\left(\frac{r-c}{a}\right)\right\}$$

where A is the atomic number, Z is the number of proton in nucleus, $\bar{\rho}$ is the average density of

experiment	measurement	calculation
Aachen-Padova [54] ($\langle E_\nu \rangle$ = 2 GeV)	$\sigma^\nu(\pi^0) = 29 \pm 10$	33
	$\sigma^{\bar{\nu}}(\pi^0) = 25 \pm 7$	33
SKAT [55] ($\langle E_\nu \rangle$ = 7 GeV)	$\sigma^\nu(\pi^+) = 106 \pm 16$	112
	$\sigma^{\bar{\nu}}(\pi^-) = 113 \pm 35$	112
	$\sigma^\nu(\pi^0) = 52 \pm 19$	56
CHARM [56] ($\langle E_\nu \rangle$ = 31 GeV)	$\sigma^\nu(\pi^0) = 96 \pm 42$	107

Table 5.1: Summary of the measured cross section of coherent pion production. Unit of the cross section is 10^{-40}cm^2/nuclei. The calculation by Rein and Sehgal model is also shown.

nucleus, and a and c, the density parameter of nucleus, are set to be $1.80/4\ln 3 = 0.41$fm and 2.69 fm, respectively.

The mean free path for pions is calculated from the optical potential model of π-nucleus [58], as a function of the distance from the nuclear center. The scattered direction of pions is determined by using the result of phase shift analysis obtained from the π-N scattering experiment [59].

The Fermi motion of nucleons and Pauli blocking effect are taken into account for the pion interaction. The nucleon momentum in the final state is restricted by Pauli blocking, to be greater than the Fermi surface momentum $P_F(r)$, which is calculated by the following equation:

$$P_F(r) = \left\{ \frac{3}{2}\pi^2 \rho_F(r) \right\}^{\frac{1}{3}}$$

This simulation program of nuclear effect is tested by

- π^{12}C scattering [60]
- π^{16}O scattering [61]
- pion photo-production ($\gamma + {}^{12}\mathrm{C} \rightarrow \pi^\pm + X$)

Fig 5.7 shows the calculated cross section of π^{16}O scattering, compared with experimental data. The simulation and experiment agree reasonably.

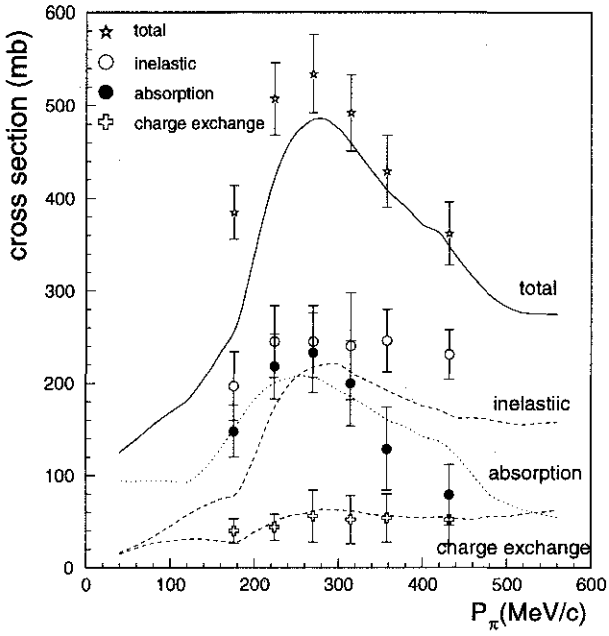

Figure 5.7: Calculated cross section of π^+ ^{16}O scattering, compared with the experimental data.

We checked the program of nuclear effect by simulating pion photo-production in a ^{12}C nucleus. The cross section of pion photo-production with nucleon was measured by using light nucleus, such as deuterium [62, 63]. Pions are generated in a ^{12}C nucleus according to this production cross section and passed through the nucleus. Fig 5.8 shows the calculated cross section, compared with experimental data [64, 65]. The agreement is good around the peak. Although there is some disagreement in the low energy region, it seems to be due to the effects which are not considered in this simulation (i.e. pion identification and interaction with the detector material).

5.4 Particle tracking and detector simulation

5.4.1 Particle tracking

The information of particles after leaving the nucleus are inputed into the program which simulates particle tracking and detector response. We adopted the GEANT code for this purpose, which has been developed at CERN and commonly used in high-energy experiments. The

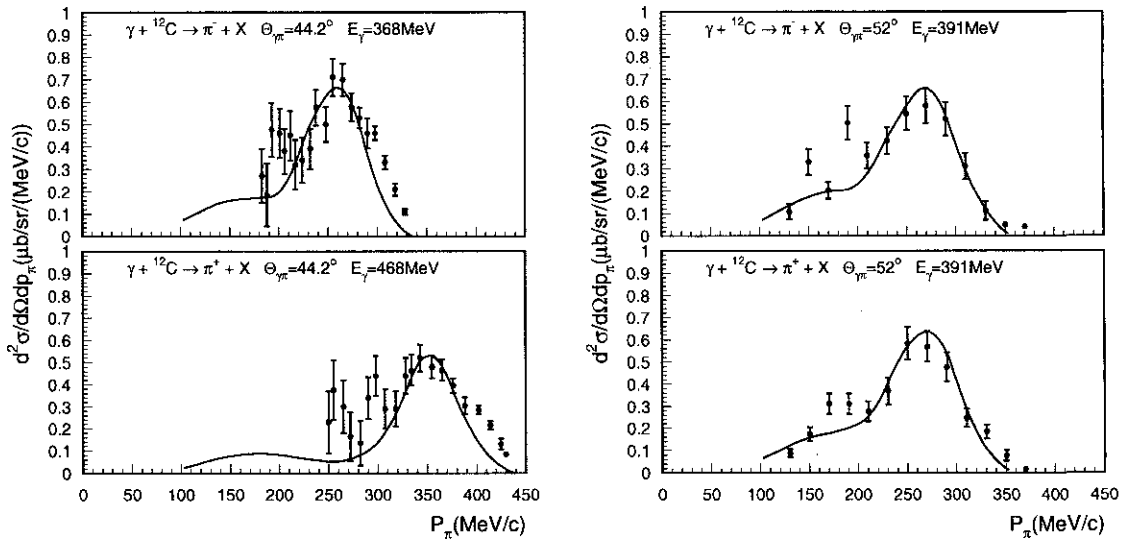

Figure 5.8: Differential cross section of pion photo-production. Solid line shows Monte Carlo calculation. Data points are taken from Ref [64] (left) and Ref [65] (right).

CALOR program is used for the hadronic interactions in water. It also has been developed at CERN and its calculation is based on the cascade mode [66]. But, in the energy range of $E_\pi < 500$ MeV, the CALOR does not reproduce experimental data well [67]. Therefore when pion momentum is less than 500 MeV/c, we developed our own program which use the cross section estimated from the experimental data of $\pi - {}^{12}\mathrm{C}$ scattering [68] and $\pi - p$ scattering [69].

5.4.2 Detector simulation

GEANT program simulates the interactions and energy loss for all particles and traces Čerenkov photon emitted by charged particles until it is detected by a PMT or absorbed.

For the attenuation of Čerenkov photon, we consider Rayleigh scattering, Mie scattering and absorption. Fig 5.9 shows the attenuation length of Čerenkov photon in our simulation program, as a function of wavelength.

Photons interact with the molecule of water through Rayleigh scattering, whose coefficient is known to have λ^{-4} dependence (the attenuation length is proportional to λ^4.) Mie scattering is included for the effect of scattering with particles, whose size is roughly same as the wavelength. Photons are scattered predominantly in the forward direction, and no wavelength dependence of attenuation coefficient is assumed in our simulation. Absorption is dominant above 450 nm

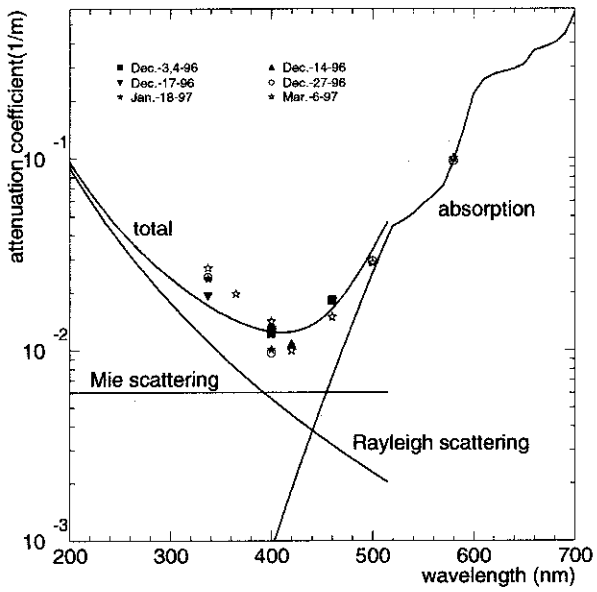

Figure 5.9: Various marks show the measured attenuation coefficient as a function of the wave length. Solid lines show the attenuation coefficient used in the Monte Carlo program.

in wavelength. We used the data given in Ref [71] for the attenuation coefficient of absorption. The absolute factors of scattering are tuned to reproduce the results measured by a laser system (see section 3.4.1 and Fig 5.9).

The reflection and absorption at the surface of the PMTs and black sheets are included in the simulation program. The reflection probability is calculated as a function of incident angle, and compared with the measurements. Fig 5.10 shows the reflection probability for each medium. Calculation and measurement agreed well and we used the calculated value. In the calculation, the photon polarization effect is included.

The quantum efficiency of PMT is shown in Fig 2.3. The dark noise of PMTs, charge and timing resolution are also taken into account in the Monte Carlo simulation.

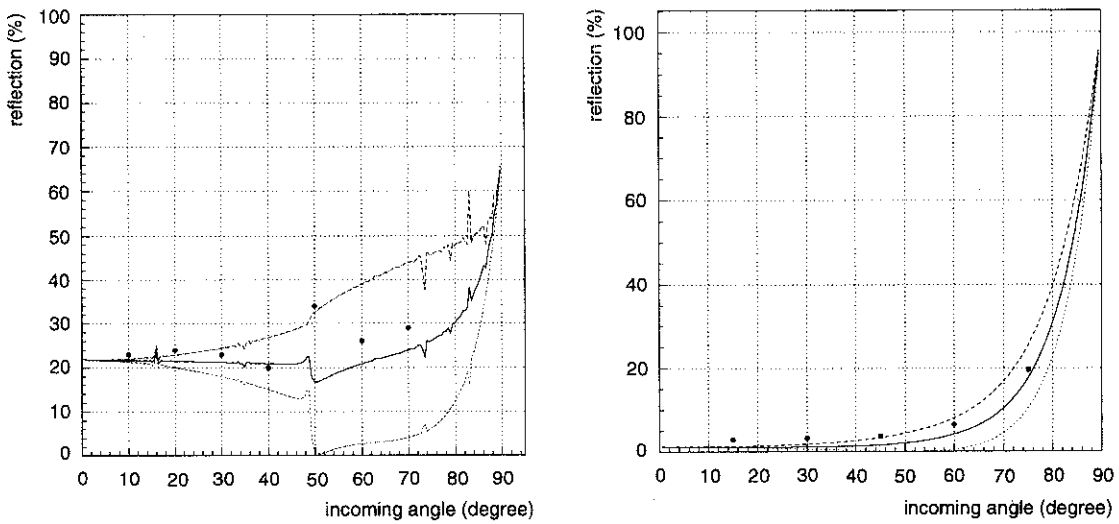

Figure 5.10: Reflection probability on the surface of a PMT (left) and a black sheet (right) as a function of incident angle. The lines are calculations: the dashed line shows S-wave and dotted line shows P-wave, the solid line shows averaged value. Points show the measured values.

Chapter 6

Event Reconstruction Method

As shown below, we have five reconstruction steps for FC atmospheric neutrino events and one step for PC events.

- For Fully-contained (FC) events
  - Vertex position determination (TDC-fit)
  - Ring counting
  - Particle identification (PID)
  - Precise vertex position determination (MS-fit)
  - Momentum determination
- For Partially-contained (PC) events
  - Vertex position determination (TDC-fit)

The difference between FC and PC reconstruction comes from the final selection of each sample. In the case of FC sample, for the identification of incident neutrino flavor, events with one Čerenkov ring are selected. In addition, momentum and particle type are determined. On the other hand, PC events are regarded as the ν_μ-induced events because the exiting tracks, in most cases, muons. It is not necessary to count number of Čerenkov rings and momentum cannot be measured because of the energy loss out of the inner detector.

After these reconstructions, we can obtain the vertex position and direction for both FC and PC sample, and additionally the number of ring, particle type and momentum for FC sample.

Most of the reconstruction programs are inherited from that of Kamiokande, but they are reorganized to be fully automatic in order to analyze a large amount of data and Monte Carlo events.

6.1 TDC-fit

TDC-fit is the vertex and direction reconstruction program using TDC information. There are two step in TDC fit, one is a rough fitting without the Čerenkov edge information (PFIT), another is a more precise fitting using the edge (TDC-fit). The vertex determined by TDC-fit is used until MS-fit is applied, and for PC sample, this is the final vertex position.

We use the time information called time residual (t_i), which is calculated by subtracting photon time-of-flight (TOF) from the photon arrival time to the i-th PMT, as follows:

$$t_i = t_i^0 - \frac{1}{c(Q_i, l_i)} \times \sqrt{(x - x_i)^2 + (y - y_i)^2 + (z - z_i)^2}$$

t_i^0	hit time of the i-th PMT
(x, y, z)	vertex position
(x_i, y_i, z_i)	position of the i-th PMT
$c(Q_i, l_i)$	light velocity in water

The time residual is expected to have a common value in all PMTs for the real vertex if the Čerenkov photons are emitted by an infinitesimally short track particle, but in fact, it is not. Also some of the photons are scattered in the water. Nevertheless the distribution of the time residual becomes shape near the real vertex. In order to quantify its sharpness, we define the goodness as a estimator of the vertex fitting as follows:

In case of PFIT:

$$G_P = \frac{1}{N_{hit}} \sum_i \exp\left(-\frac{(t_i - \langle t \rangle)^2}{2(1.5\sigma)^2}\right)$$

and in case of TDC-fit:

$$G = \begin{cases} \dfrac{\sum_i \frac{1}{\sigma^2} \exp\left(-\frac{(t_i - \langle t \rangle)^2}{2(1.5\sigma)^2}\right)}{\sum_i \frac{1}{\sigma^2}} & \text{(inside Čerenkov cone)} \\ \dfrac{\sum_i \frac{1}{\sigma^2} \mathrm{Max}\left[\exp\left(-\frac{(t_i - \langle t \rangle)^2}{2(1.5\sigma)^2}\right), 0.8 \exp\left(-\frac{t_i - \langle t \rangle}{20nsec}\right)\right]}{\sum_i \frac{1}{\sigma^2}} & \text{(outside Čerenkov cone)} \end{cases}$$

where σ is the mean value of PMT timing resolution, $\rangle t\langle$ is the mean of t_i. The goodness takes the value from 0 to 1 and the higher value is estimated to be better. The track length of charged particle and time delay of the scattered light are also taken into account in the calculation of goodness of TDC-fit. TDC-fit finds the vertex where the goodness becomes maximum.

In order to find out the particle direction, TDC-fit picks up the outer edge of the Čerenkov cone from the observed charge image.

The Čerenkov edge is obtained from the charge distribution as a function of the Čerenkov opening angle (PE(θ)). Fig 6.1 shows the typical (PE(θ)) distribution for an e-like event. The Čerenkov edge (θ_{edge}) is determined so as to be outside but nearest the peak of PE(θ) distribution (θ_{peak}) with $d^2PE/d\theta^2$ 0. Under these conditions, the direction is searched so as to maximize the following evaluation function:

$$f = \frac{\int_0^{\theta_{edge}} \mathrm{PE}(\theta)d\theta}{\sin\theta_{edge}} \cdot \left(\frac{d\mathrm{PE}(\theta)}{d\theta}\right)^2 \cdot \exp\left\{-\frac{(\theta_{edge}-\theta_C)^2}{\sigma_\theta^2}\right\}$$

where θ_C and σ_θ are the Čerenkov opening angle and its resolution, respectively.

Fig 6.2 shows the distribution of the distance of real vertex to fitted vertex for FC e-like, μ-like and PC events. The vertex resolutions were estimated to be 64.2, 58.7 and 134.4 cm for FC e-like, μ-like and PC events.

6.2 Ring counting

TDC-fit tends to find the most energetic Čerenkov ring and determine its vertex and direction, but ring finding and direction fit is necessary for other Čerenkov rings.

Fig 6.3 shows the basic concept to find other rings. The shaded circle shows the Čerenkov image projected to a plane perpendicular to the particle direction. The ring counting programs picks up hit PMTs and draws the virtual circles (dashed line) whose center are at the hit PMTs and opening angle is 42°. After virtual rings are drawn, the center of Čerenkov ring is estimated as a intersection point of these rings.

The detail procedure is as follows: first of all, expected photoelectron (charge) of the Čerenkov ring which was picked at TDC-fit is subtracted for each PMT. The virtual Čerenkov

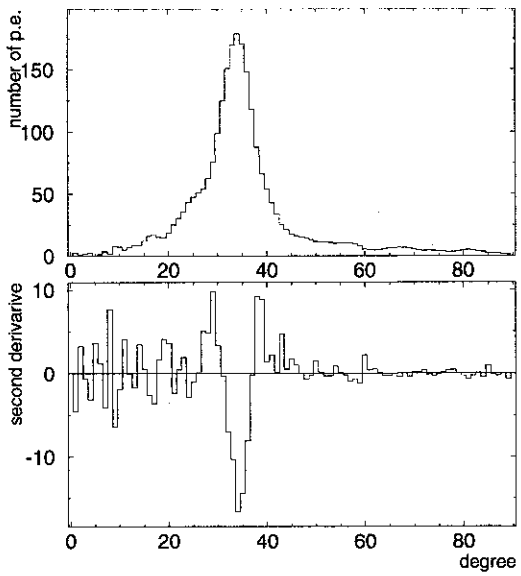

Figure 6.1: A typical PE(θ) distribution for an e-like event and $d^2PE/d\theta^2$ distribution as a function of opening angle.

rings are drawn in the PMT direction from the vertex position weighted by its residual charge onto the "charge map". This "charge map" is a 2-dimensional map with the direction of azimuth and polar angle in the view from the vertex position. Typical "charge map" is shown in Fig 6.3. If the second ring exists, the second peak can be seen, shown as the plot. The ring counting program picks up some candidate rings from this map. Then a likelihood method is used to judge if these candidates are real Čerenkov rings or not.

We checked the performance of the ring counting with the charged current quasi-elastic events of the atmospheric neutrino Monte Carlo because the charged current quasi-elastic interaction generates only one lepton and should be identified as a single-ring event. The efficiency is defined as (Number of quasi-elastic events identified as a single-ring event)/ (Number of quasi-elastic events).

Fig 6.4 shows the efficiency as a function of the distance of vertex from the inner detector wall (D_{wall}). The efficiency is worse near the detector wall because the ring counting program tends to count more number of Čerenkov ring than real due to the scattered light. However, the efficiency keeps more than 85 % in the fiducial volume.

Fig 6.5 shows the efficiency in the fiducial volume as a function of the lepton momentum. The lower efficiency for ν_e events is caused by the difficulty of judging the number of Čerenkov ring due to its diffused Čerenkov edge by the electromagnetic shower.

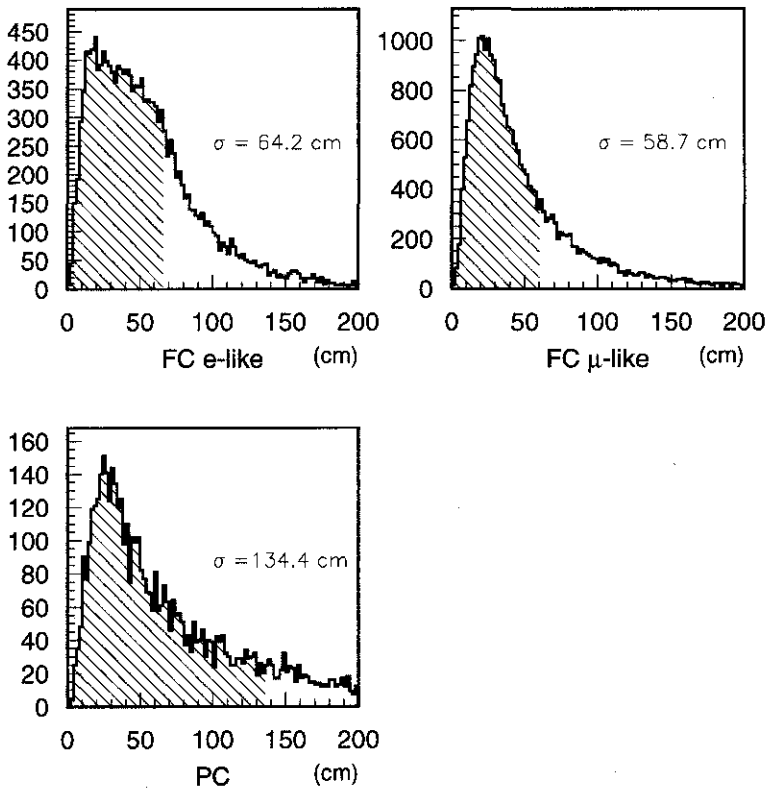

Figure 6.2: Distribution of the distance from real vertex to fitted vertex by TDC-fit, for FC e-like, μ-like and PC events. The vertex resolution is defined as the distance where the 68 % of events are found within and shown by hatched region.

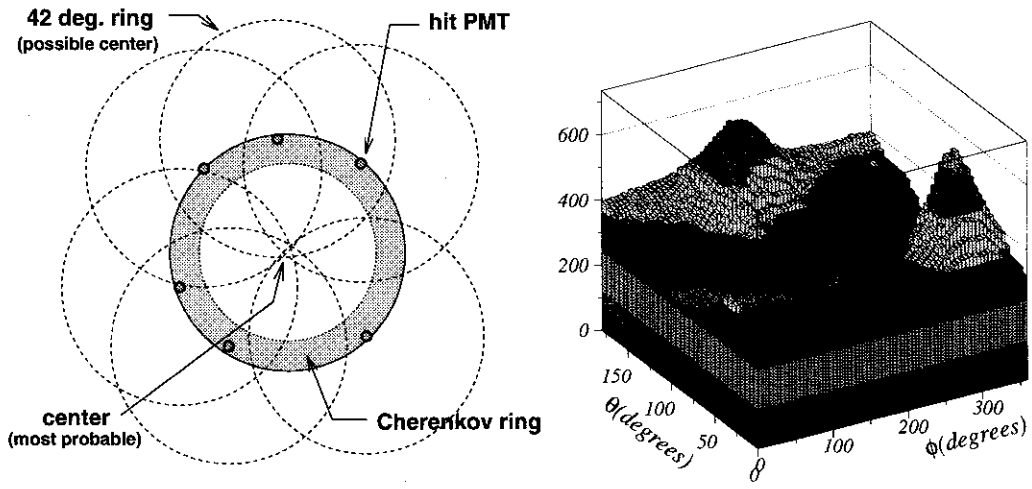

Figure 6.3: Left figure shows the basic concept of finding Čerenkov ring direction. The shaded ring shows Čerenkov ring and possible center can be found by the focus of dashed circles. Right figure shows the charge map for a typical two ring event. The position of the two peaks in $\theta - \phi$ plane correspond to the directions of Čerenkov rings.

6.3 Particle identification

It is possible to separate Čerenkov rings due to electrons and gammas from those due to muons and pions. Čerenkov ring produced by an electron is diffuse because of the electromagnetic shower and multiple scattering. Čerenkov ring produced by a muon is characterized by its sharpness of Čerenkov edge because a muon propagate in water with a simple dE/dx energy loss only. In addition to the pattern of the ring, the information of opening angle is also used to separate particles. The opening angle is important for the identification of low energy muons because the opening angle, θ, and particle velocity has a relation of $\cos\theta = (n\beta)^{-1}$.

The details of the particle identification method is described below. First of all,we calculate the expected Čerenkov image pattern of both e-like and μ-like from the reconstruction information, (vertex, direction, momentum and opening angle). The expected number of p.e. in the i-th PMT is expressed as follows:

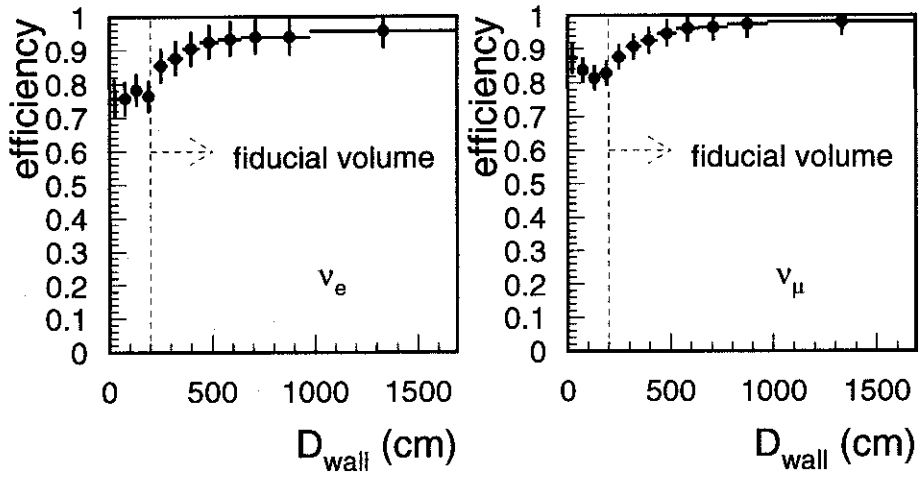

Figure 6.4: Efficiency identified as a single-ring event for ν_e (left) and ν_μ (right) charged current quasi-elastic events in the atmospheric neutrino Monte Carlo sample, as a function of the distance of vertex from the inner detector wall (D_{wall}).

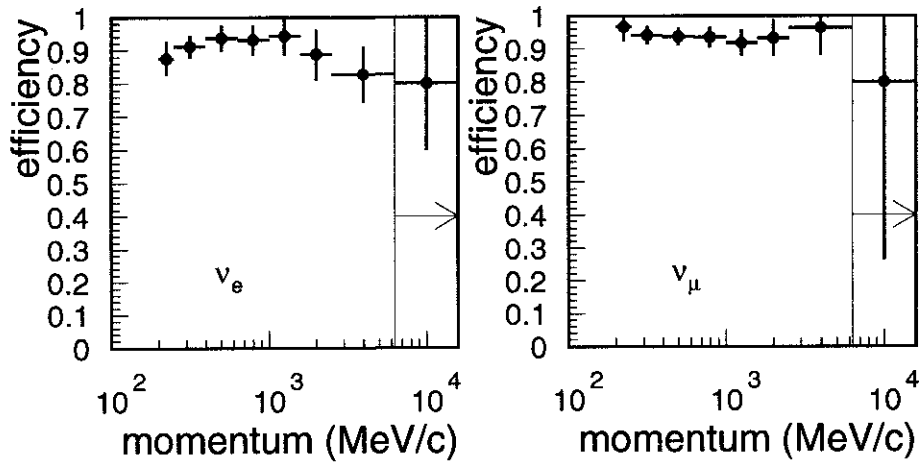

Figure 6.5: Efficiency identified as single-ring event for ν_e (left) and ν_μ (right) charged current quasi-elastic events in the atmospheric neutrino Monte Carlo sample, as a function of lepton momentum.

$$Q_i^{exp} = \begin{cases} \alpha_e \cdot Q_{MC}(\theta_i, p_e) \cdot (\frac{16.9m}{l_i})^{1.5} \cdot \exp(-\frac{l_i}{L}) \cdot f(\Theta) + S_i & (\text{ e-like }) \\ \left(\alpha_\mu \cdot \frac{\sin^2\theta_i}{l_i(\sin\theta_i + l_i(\frac{d\theta}{dx}))} + Q_i^{knock}(\theta_i)\right) \cdot \exp(-\frac{l_i}{L}) \cdot f(\Theta) + S_i & (\ \mu\text{-like }) \end{cases}$$

where

α_e,α_μ	normalization factor
l_i	distance from vertex to i-th PMT
θ_i	angle of PMT from the particle direction
L	light attenuation length
$f(\Theta)$	function of relative PMT photo sensitive area
S_i	expected amount of scattered light

In the case of e-like events, the expected p.e., $Q_{MC}(\theta_i, p_e)$ was produced beforehand by a Monte Carlo simulation because the analytic calculation of electromagnetic shower is difficult. $Q_{MC}(\theta_i, P_e)$ is the table of the expected p.e., which is the average number of p.e. in a circular area of 50cm diameter (equal to PMT photosensitive area) located on a sphere of 16.9m in radius. The factor of $(\frac{16.9m}{l_i})^{1.5}$ takes into account the distance dependence of the light intensity. Its power index is estimated from a Monte Carlo study. $\exp(-l_i/L)$ indicates the light attenuation in water.

In the case of μ-like events, we can calculate the expected p.e. by the above formula. The second term in the right-hand side originate from the ionization energy loss $\frac{dE}{dx}$ in water. $dx\sin\theta + ld\theta$ takes into account the change in the photon density which is caused by the change in θ, corresponding to the energy loss. $\sin^2\theta_i$ expresses the intensity variation of Čerenkov photons. $Q_i^{knock}(\theta_i)$ is the contribution from knock-on electron, which was estimated and tabulated beforehand by a Monte Carlo simulation. In addition to this expected p.e., the expected scatter light S_i is also added to the direct photon.

The definition of Likelihood for Čerenkov image pattern for both e-like and μ-like is expressed as follows:

$$L(e \text{ or } \mu) = \prod_{\theta_i < (1.5 \times \theta_C)} Prob(Q_i^{exp}(e \text{ or } \mu), Q_i^{obs})$$

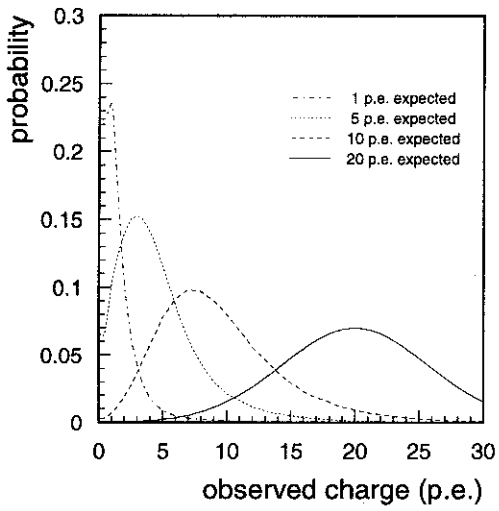

Figure 6.6: Probability function as a function of observed charge and expected charge. This function is composite by the single-photoelectron distribution (Q_{obs}<20p.e.) and Gaussian distribution (Q_{obs}>20p.e.).

where *Prob* is the function that gives the probability to detect Q_i^{obs} p.e. in i-th PMT when Q_i^{exp} is expected. This function is estimated based on the single-photoelectron distribution for Q_{obs} <20p.e. and approximated by a Gaussian distribution for Q_{obs} >20 p.e., as shown in Fig 6.6.

In order to combine with the information of the Čerenkov opening angle, this likelihood is translated to χ^2 parameter:

$$\chi^2_{pattern}(e \text{ or } \mu) = -2\log(L(e \text{ or } \mu)) + \text{constant}$$

Then the probability by Čerenkov pattern is given by

$$P_{pattern}(e \text{ or } \mu) = \exp\left\{-\frac{1}{2}\left(\frac{\chi^2(e \text{ or } \mu) - \text{Min}[\chi^2(e), \chi^2(\mu)]}{\sigma_{\chi^2}}\right)^2\right\}$$

where $\sigma_{\chi^2} = \sqrt{N_D}$. N_D is the number of the used PMT for the likelihood calculation.

When the particle type is assumed, the expected Čerenkov opening angle can be calculated from the particle momentum. Therefore The probability by the Čerenkov opening angle is given by

$$P_{angle}(e \text{ or } \mu) = \exp\left\{-\frac{1}{2}\left(\frac{\theta_{exp}(e \text{ or } \mu) - \theta_{obs}}{\sigma_{\Delta\theta}}\right)^2\right\}$$

Total probability is defined as the production of the probabilities of the Čerenkov pattern and opening angle.

$$P(e \text{ or } \mu) = P_{pattern}(e \text{ or } \mu) \times P_{angle}(e \text{ or } \mu)$$

Finally, PID estimator is defined as

$$\text{PID estimator} = \text{constant} \times (\sqrt{-\log P(e)} - \sqrt{-\log P(\mu)})$$

If this PID estimator is positive (negative), the event is identified as e-like (μ-like).

Fig 6.7 shows the PID estimator estimated by the atmospheric Monte Carlo events for visible energy $E_{vis} < 1.33$ GeV (sub-GeV) and $E_{vis} > 1.33$ GeV (multi-GeV) sample. The agreement of data and Monte Carlo is quite good. The misidentification probabilities for charged current quasi-elastic events is estimated to be 0.4 % (0.6 %) for sub-GeV ν_μ (ν_e) events and 1.4 % (0.3 %) for multi-GeV events.

6.4 MS-fit

TDC-fit works well for all energy range and all types of neutrino events. But it has worse vertex resolution in the direction of Čerenkov ring, compared to that in the perpendicular direction. It comes from the goodness definition of TDC-fit. The deviation of time residual $t_i - < t >$, which can be seen in the goodness definition of TDC-fit, is not significantly changed in places where the distance from all hit PMTs is same. Therefore it is difficult to determine the vertex in the Čerenkov direction precisely, due to the axial-symmetry of Čerenkov ring.

In order to solve this problem, we apply the likelihood method which is used in the PID algorithm to determine vertex in the particle direction and inherit the goodness of TDC-fit for fitting vertex in the perpendicular direction. MS-fit was developed based on this method. The meaning of "MS" comes from the types of Čerenkov pattern, M(eson) and S(hower). MS-fit follows PID because it uses the particle type determined by PID algorithm. The difference of likelihood methods between PID and MS-fit is the treatment of the Čerenkov opening angle. In the case of PID algorithm, vertex position is fixed by TDC-fit and opening angle is a free parameter to find maximum likelihood, but for MS-fit, the opening angle is fixed according to the momentum and particle type, and find vertex where the likelihood becomes maximum. As a result, we get better resolution in both vertex and direction than TDC-fit.

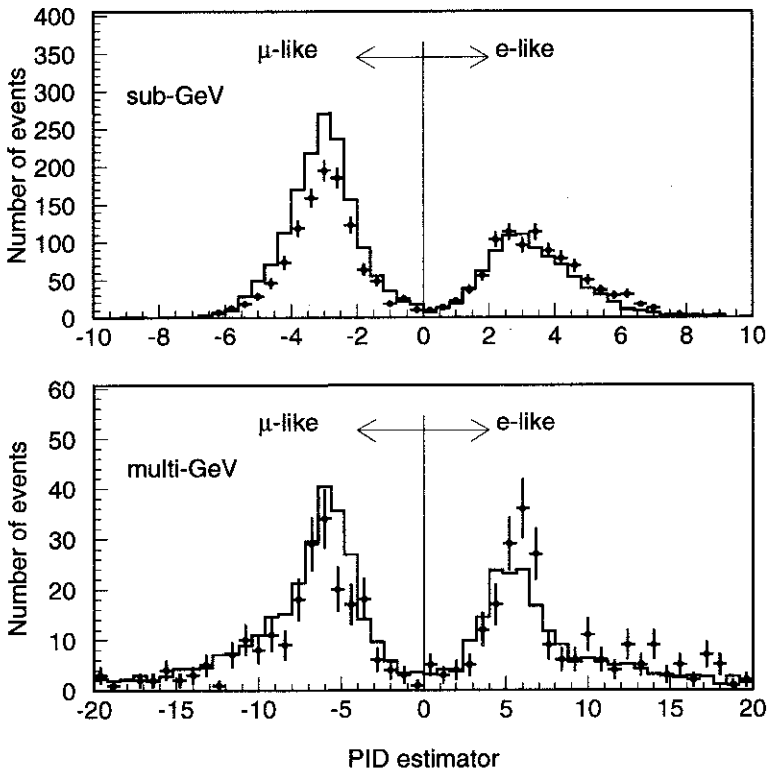

Figure 6.7: Distribution of PID estimator for the atmospheric sub-GeV and multi-GeV data (points) and Monte Carlo (histogram) events. The events of the positive (negative) value are identified as e-like (μ-like) events.

Fig 6.8 shows the distribution of distance from "real" vertex to fitted vertex which is estimated by the atmospheric neutrino Monte Carlo events. The vertex resolution is defined as the distance where the 68 % of events are found within. We can obtain 23~56 cm in resolution for sub-GeV and multi-GeV sample. The vertex resolution determined by MS-fit becomes better than that of TDC-fit, especially for μ-like.

Fig 6.9 shows the distribution of the angle of real particle direction and reconstructed direction, estimated by the atmospheric neutrino Monte Carlo events. The angular resolution is estimated to be 0.9~3.0°.

6.5 Momentum determination

The Momentum of charged particle is an important information to estimate the incident neutrino energy. In order to determine momentum, we use the sum of the corrected photoelectrons, called as RTOT. The purpose of RTOT is to derive momentum which does not depend on vertex position, particle direction and water transparency, therefore the corrections of water transparency , PMT acceptance, gain and so on are included in the calculation of RTOT. Momentum are derived from RTOT according to the conversion table, which is previously obtained from a Monte Carlo simulation.

In case of multi-ring event, charge separation for each ring are applied before momentum determination. But for single ring event, this separation is not necessary.

The method of calculating RTOT and momentum determination is as follows:

1. apply timing cut and eliminate photoelectrons due to a muon-decay electron which happens within the 1μsec gate window. Timing window is set to (-50,250) nsec in residual time, where the peak of residual time distribution is set to zero.

2. calculate summed photoelectrons for the PMTs, the opening angle of which is less than 70° and calculate the primary RTOT. each PMT charge is corrected by water transparency and PMT acceptance. In the case of muon, muon range is taken into account for the calculation of photon flight length.

3. subtract expected scatter light from RTOT.

4. correct RTOT with relative gain of the whole PMT.

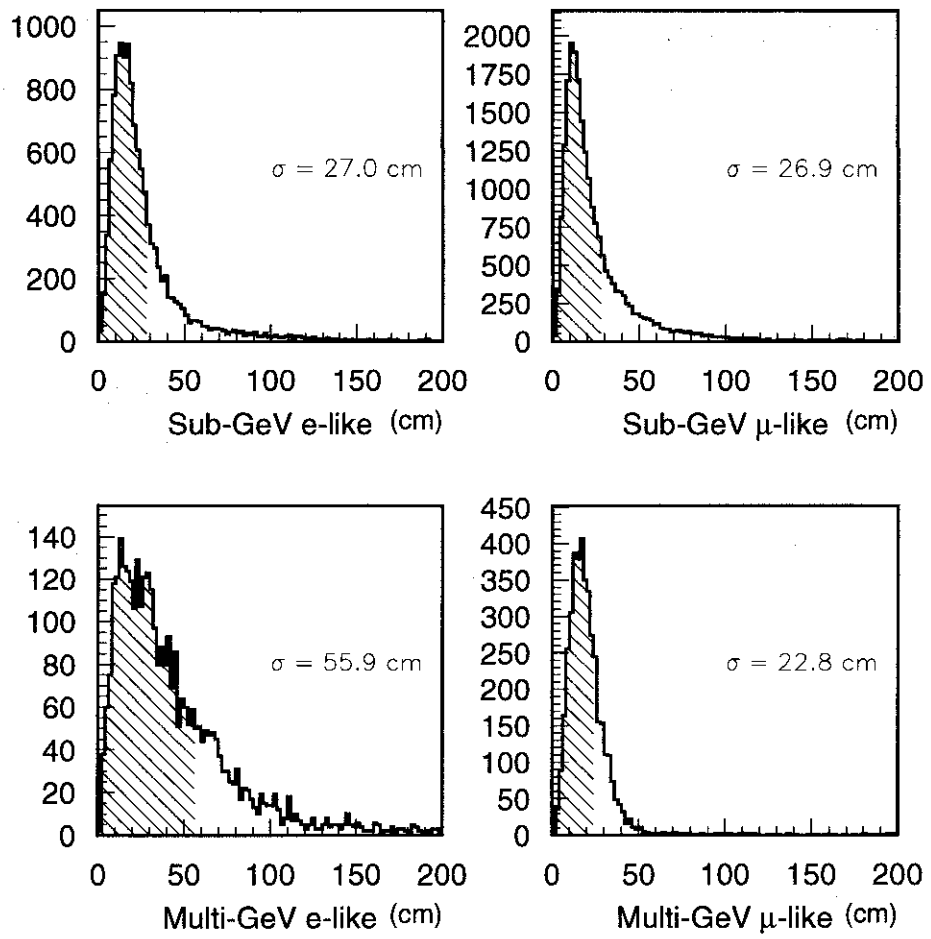

Figure 6.8: Distribution of the distance from real vertex to fitted vertex for FC sub-GeV and multi-GeV events. The vertex resolution is defined as the distance where the 68 % of events are found within and shown by hatched region.

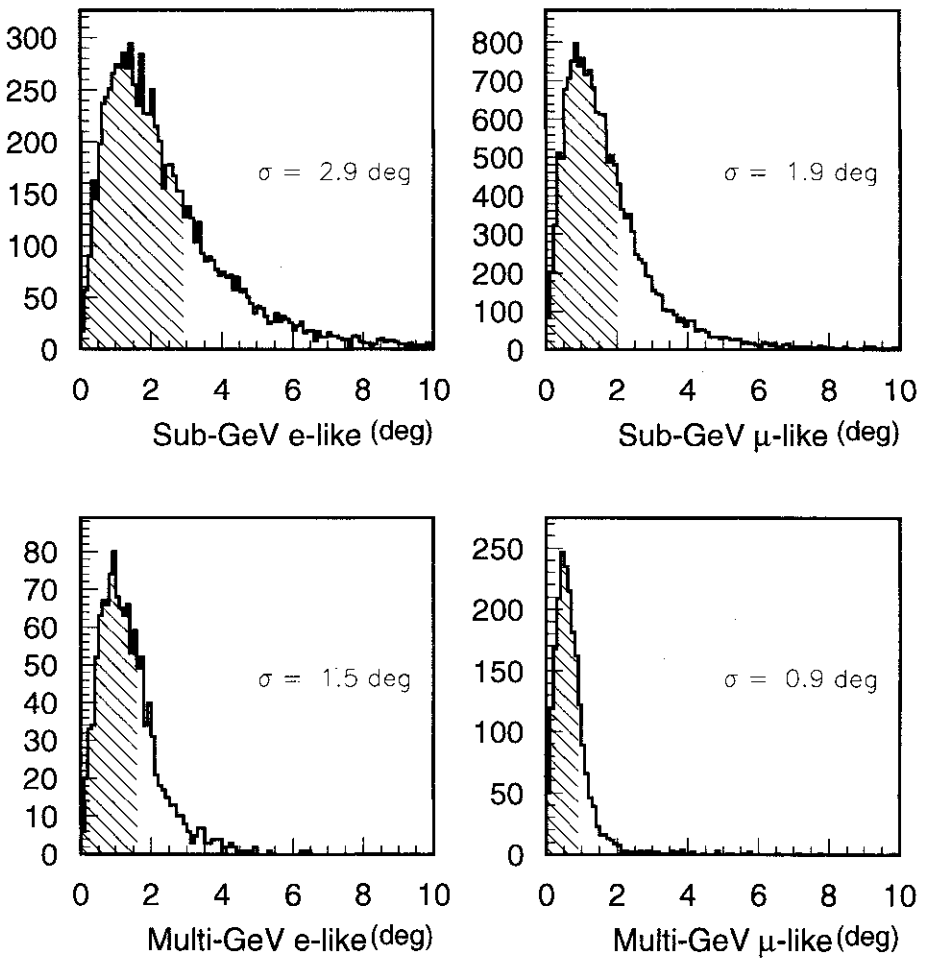

Figure 6.9: Distribution of the angle of real particle direction and reconstructed direction for FC sub-GeV (multi-GeV) events. The angular resolution is defined as the angle where the 68 % of events are found within and shown by hatched region.

5. obtain momentum based on RTOT and particle type.

The subtraction of scatter light makes the momentum resolution better because the ratio of scatter light in RTOT is not constant, it depends on vertex and particle direction. For example, the momentum resolution of 1 GeV electron is improved from 4.8 % to 3.2 % by scatter light subtraction.

The relative gain correction is adopted to correct for the time variation of energy scale. It is obtained from the water transparency measurement using cosmic ray muon (see section 3.4.2).

RTOT can be expressed by the following equation:

$$\mathrm{RTOT} = \frac{G_{MC}}{G}\left\{\alpha \times \sum_{\substack{\theta_i < 70^\circ \\ -50 < t_{res} < 250}} Q(i) \cdot \frac{\cos\Theta}{f(\Theta)} \cdot \exp(-\frac{l_i}{\lambda}) - \sum_{\theta_i<70^\circ} S(i)\right\}$$

where

α	normalize factor
G,G_{MC}	relative PMT gain of data and Monte Carlo
t_{res}	time from the peak of time residual
θ_i	opening angle between PMT direction from the vertex position and the particle direction
Θ	angle of photon arriving direction relative to the PMT facing direction
$f(\Theta)$	function of relative PMT photo sensitive area
l_i	distance from vertex to the i-th PMT position
λ	attenuation length of light in the water
$Q(i)$	photoelectron detected by the i-th PMT
$S(i)$	expected photoelectron of scatter light in the i-th PMT

Fig 6.5 shows the relation between RTOT and momentum for electron and muon events. These are estimated from Monte Carlo events, whose vertex positions are in fiducial volume and directions are random.

Fig 6.11 shows momentum resolution estimated from these MC sample as a function of momentum. It is defined as 1σ width of the Gaussian fit. As a result of fitting these data, the momentum resolution is estimated to be:

$$0.6 + \frac{2.6}{\sqrt{\mathrm{P(GeV/c)}}}\% \qquad \text{(electron)}$$

$$1.7 + \frac{0.7}{\sqrt{\mathrm{P(GeV/c)}}}\% \qquad \text{(muon)}$$

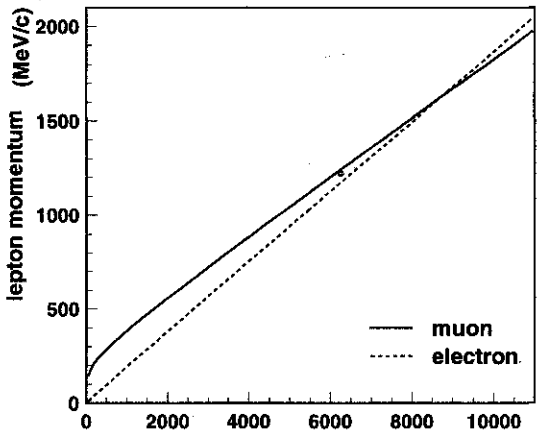

Figure 6.10: Relation between RTOT and momentum for electron and muon type.

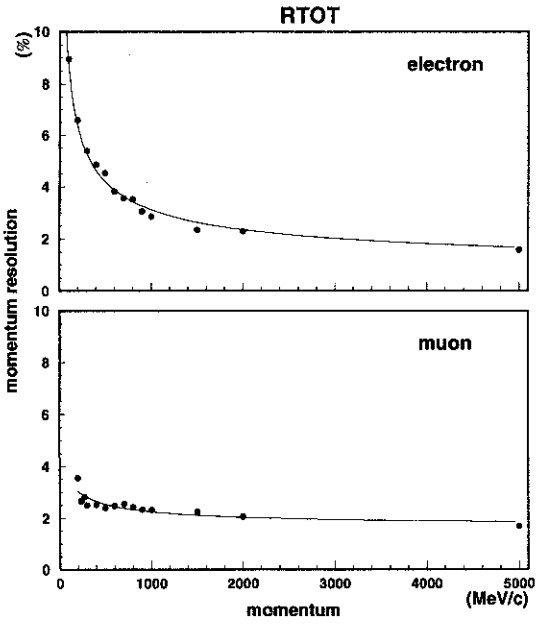

Figure 6.11: Momentum resolution for (a)electron and (b)muon. solid lines show the fitted result, estimated from MC events in the fiducial volume.

Chapter 7

Event summary and results

7.1 Event summary

In this thesis, we have analyzed the data which were taken from May-1996 to May-1998, and the experimental livetime amounts to 535 days for both fully-contained (FC) and partially-contained (PC) sample. We applied the following criteria for FC and PC samples and made the final data sets:

- Fully-contained (FC)
  - $D_{wall} > 200$ cm
  - Number of outer detector hits (N_{hitac}) < 10
  - Visible energy (E_{vis}) > 30 MeV
- Partially-contained (PC)
  - $D_{wall} > 200$ cm
  - Number of outer detector hits (N_{hitac}) ≥ 10
  - Total photoelectron > 3000 p.e.

where D_{wall} is the distance of the event vertex position from the nearest inner detector wall. The region $D_{wall} > 200$ cm is defined as the fiducial region for both FC and PC events. The fiducial volume corresponds to 22.5 kton and the exposure of the detector amounts to the 33.0

ktonyr. The visible energy (E_{vis}) is defined as the energy sum of each ring assuming that each ring is produced by an electron. 30 MeV corresponds to 197 MeV/c of muon momentum. The definition of number of outer detector hits (N_{hitac}) was described at the section of PC 2nd reduction (see 4.2.2). N_{hitac} is used to separate FC and PC events. Fig 7.1 shows N_{hitac} distribution for both FC and PC events in the fiducial volume. The separation of FC and PC events is clearly seen. The requirement of total photoelectron > 3000 p.e., which corresponds to ~580 MeV/c of muon momentum, is safe enough for PC events because the exiting muons must have at least 700 MeV/c momentum to reach the outer detector.

We obtained a total of 4474 FC events and 301 PC events according to the above criteria. The Monte Carlo simulation was made for both FC and PC with 10 years of livetime, based on the Honda flux [30], and analyzed by the same reduction and reconstruction methods as data.

The distributions of the number of Čerenkov ring and visible energy are shown in Fig 7.2 and Fig 7.3. From these figures, it can be seen that Monte Carlo can reproduce the atmospheric neutrino events well.

7.2 Flavor ratio

Table 7.1 shows the event summary of the atmospheric neutrino sample compared with the Monte Carlo prediction. We separate FC sample into two at 1330 MeV of the visible energy, E_{vis}, in order to see the energy dependent features of the atmospheric neutrino sample. The sample with E_{vis} < 1330 MeV is called as "sub-GeV" and with E_{vis} > 1330 MeV is "multi-GeV". All PC events are categorized to "multi-GeV" sample.

In order to measure the μ/e ratio, we required that there should be only a single ring identified in a FC event (1-ring event). Each 1-ring event is categorized to be either e-like or μ-like by the result of PID algorithm and the particle type indicates us the incident neutrino flavor. Table 7.2 shows the estimation of the neutrino interaction mode for sub-GeV, multi-GeV and PC samples by the Monte Carlo simulation. According to it, 84~88 % of e-like events are due to charged current ν_e interactions and 95~99 % of μ-like and PC are charged current ν_μ interactions. From this table, we assign all PC events to be μ-like. The lower momentum threshold for sub-GeV 1-ring events is set to be 200 MeV/c for both e-like and μ-like events.

Fig 7.4 shows the event vertex distribution projected to Z direction (left) and X-Y plane

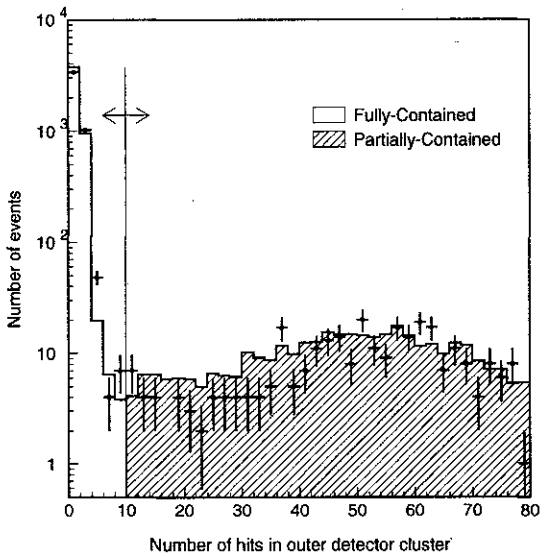

Figure 7.1: Distribution of N_{hitac}, the number of hits within a 500 nsec window in an outer detector cluster, for data (points) and Monte Carlo (histogram). Monte Carlo is normalized to the livetime of data. The separation between FC and PC events is made at 10 hits.

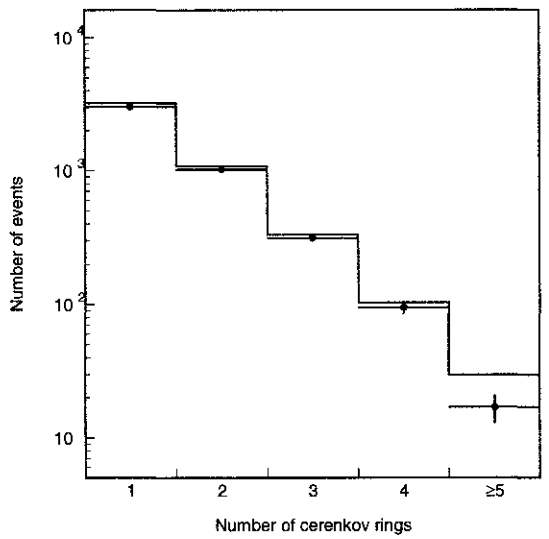

Figure 7.2: Distribution of number of Čerenkov ring for fully-contained data (points) and Monte Carlo (histogram) events. Monte Carlo is normalized to the livetime of data.

	Data	Monte Carlo	Data/M.C.
sub-GeV fully-contained (E_{vis} < 1.33 GeV)			
1-Ring	2196	2462.0	0.88
e-like (P_e > 200MeV/c)	1037	884.4	1.16
μ-like (P_μ >200MeV/c)	1158	1573.6	0.74
μ/e	1.12	1.77	0.63
2-Ring	733	780.1	0.94
>3-Ring	178	200.5	0.89
R = 0.63 ± 0.03 (stat.) ± 0.04 (syst.)			
multi-GeV fully-contained (E_{vis} > 1.33 GeV)			
1-Ring	520	531.7	0.98
e-like	290	236.0	1.23
μ-like	230	295.7	0.78
μ/e	0.79	1.25	0.65
2-Ring	285	296.2	0.96
>3-Ring	248	263.8	0.94
Partially-contained	301	371.6	0.81
R_{FC+PC} = 0.65 ± 0.05 (stat.) ± 0.08 (syst.)			

Table 7.1: Summary of atmospheric neutrino events for 33.0 ktonyr exposure of the detector for data and Monte Carlo. The number of Monte Carlo events is normalized by the livetime of the data.

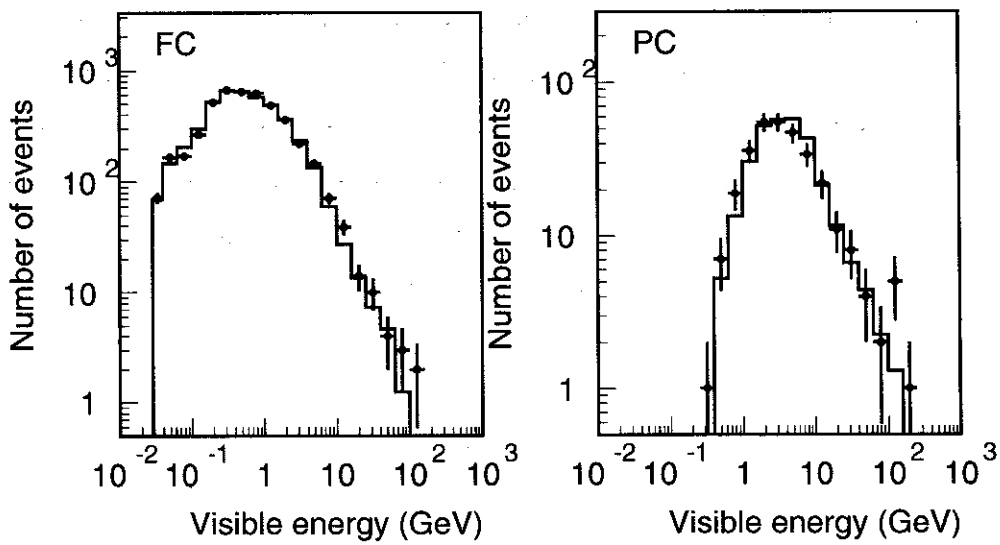

Figure 7.3: Visible energy distribution for fully-contained (FC) and partially-contained (PC) events. Points with error bars show data and histograms show Monte Carlo prediction, which is normalized by the livetime of the data.

	ν_e CC(q.e.)	ν_μ CC(q.e.)	NC
FC sub-GeV			
e-like	88.7(69.3)	1.9(0.3)	9.3
μ-like	0.4(0.3)	95.9(75.4)	3.8
FC multi-GeV			
e-like	84.4(38.2)	7.0(0.9)	8.6
μ-like	0.5(0.1)	99.1(54.1)	0.4
PC	1.6(0.3)	97.8(17.9)	0.7

Table 7.2: Summary of the neutrino interaction mode for FC and PC Monte Carlo samples. "CC" shows charged current and "NC" shows neutral current interaction events. "q.e." shows quasi-elastic scattering events. Unit is percent(%).

(right) for the atmospheric neutrino events. The region pointed by lines and arrows shows the fiducial region. The number of Monte Carlo events is normalized to that of data events within fiducial region in order to compare the shape of distributions. The distributions of data and Monte Carlo agree well. The excess at the highest bin in the Z distribution is due to cosmic-ray muons which entered into the inner detector through less efficient regions of the outer detector. Any excess cannot be seen near the detector wall inside the fiducial volume.

We defined R as the μ/e ratio of the data compared with the Monte Carlo prediction ($(\mu/e)_{Data}/(\mu/e)_{MC}$) and obtained for sub-GeV and multi-GeV samples as follows:

$$\begin{aligned} \mathrm{R} &= 0.63 \pm 0.03\ (\mathrm{stat.}) \pm 0.04\ (\mathrm{syst.}) \qquad (\text{sub-GeV}) \\ \mathrm{R_{FC+PC}} &= 0.65 \pm 0.05\ (\mathrm{stat.}) \pm 0.08\ (\mathrm{syst.}) \qquad (\text{multi-GeV}) \end{aligned}$$

where PC events are included to the multi-GeV μ-like events. R, $\mathrm{R_{FC+PC}}$ are significantly smaller than unity. The systematic errors in R and $\mathrm{R_{FC+PC}}$ are estimated to be 7 % and 11 % respectively and the details are discussed later. These results are consistent with the results obtained by Kamiokande [5], IMB (sub-GeV) [6] and Soudan-2 [8].

Fig 7.5 shows the D_{wall} distribution of the event vertex for e-like, μ-like and the μ/e ratio. Each bin is taken to be equal in the detector volume. The μ/e ratio is consistent with flat inside the fiducial region for both the sub-GeV and multi-GeV samples. The relatively high μ/e value just inside the fiducial region for the multi-GeV is due to relative deficit of e-like events.

Fig 7.6 shows the momentum distribution for FC e-like and μ-like events. The μ/e ratio, the ratio of Data to Monte Carlo, and R=$(\mu/e)_{Data}/(\mu/e)_{MC}$ as a function of momentum are also shown. There is a deficit for μ-like events and an excess for e-like events in all the momentum regions of this figure. However, because of the systematic error of absolute event rate ($\pm$25 %, most of which comes from the uncertainty of the primary proton flux), we cannot determine whether the deviation of R from unity is caused by a muon deficit or an electron excess. The R distribution shows no strong momentum dependence for both sub-GeV and multi-GeV energy regions.

7.3 Systematic uncertainty in the flavor ratio

Table 7.3 shows the summary of the possible sources of systematic uncertainties in R.

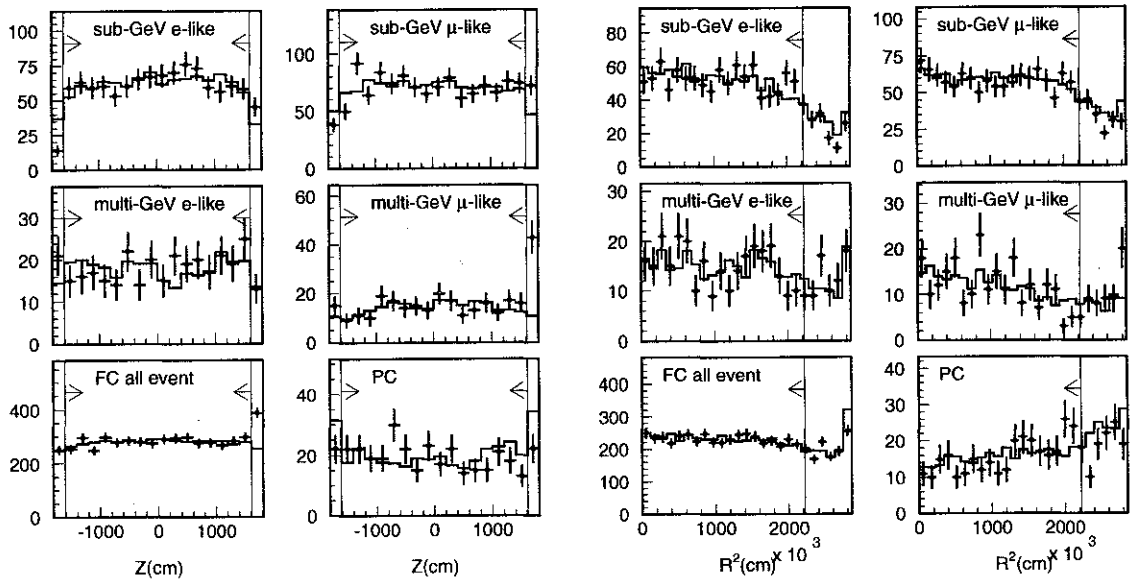

Figure 7.4: Z (left) and $R^2(=X^2+Y^2)$ (right) distributions of the event vertex for the atmospheric neutrino samples. Error bar shows the statistical error for the real data. Histogram shows the Monte Carlo prediction and normalized to the number of data events within the fiducial volume. Z=0 and R^2=0 correspond to the center of the detector. The high rate at the highest bin in the Z distribution is due to cosmic-ray muons.

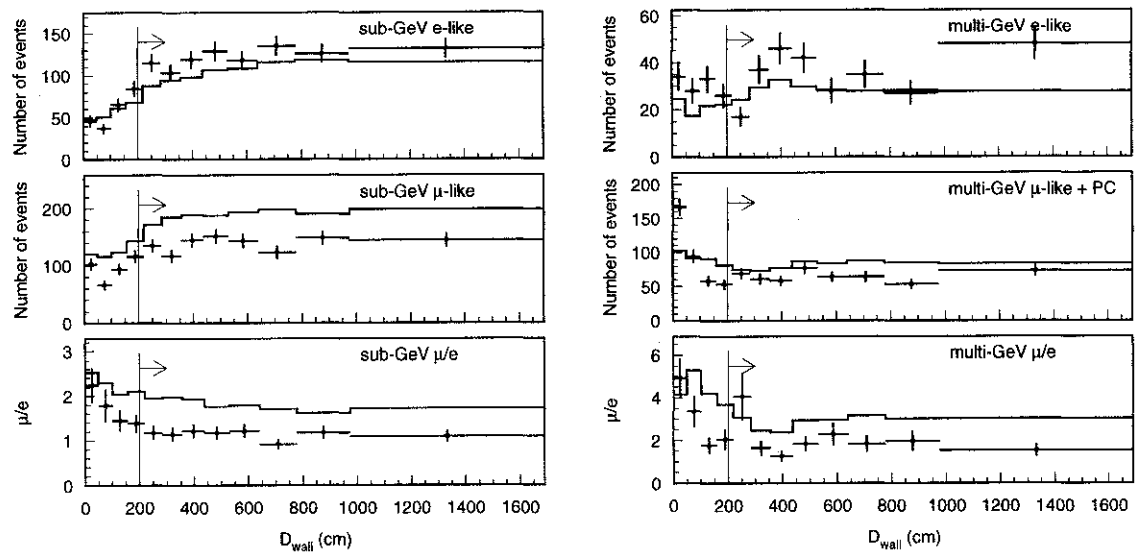

Figure 7.5: D_{wall} distribution of the atmospheric sub-GeV (left) and multi-GeV (right) samples. D_{wall} is defined as the distance of vertex position from the nearest inner detector wall. Monte Carlo is normalized to the data livetime. The detector volume of each bin is taken to be equal.

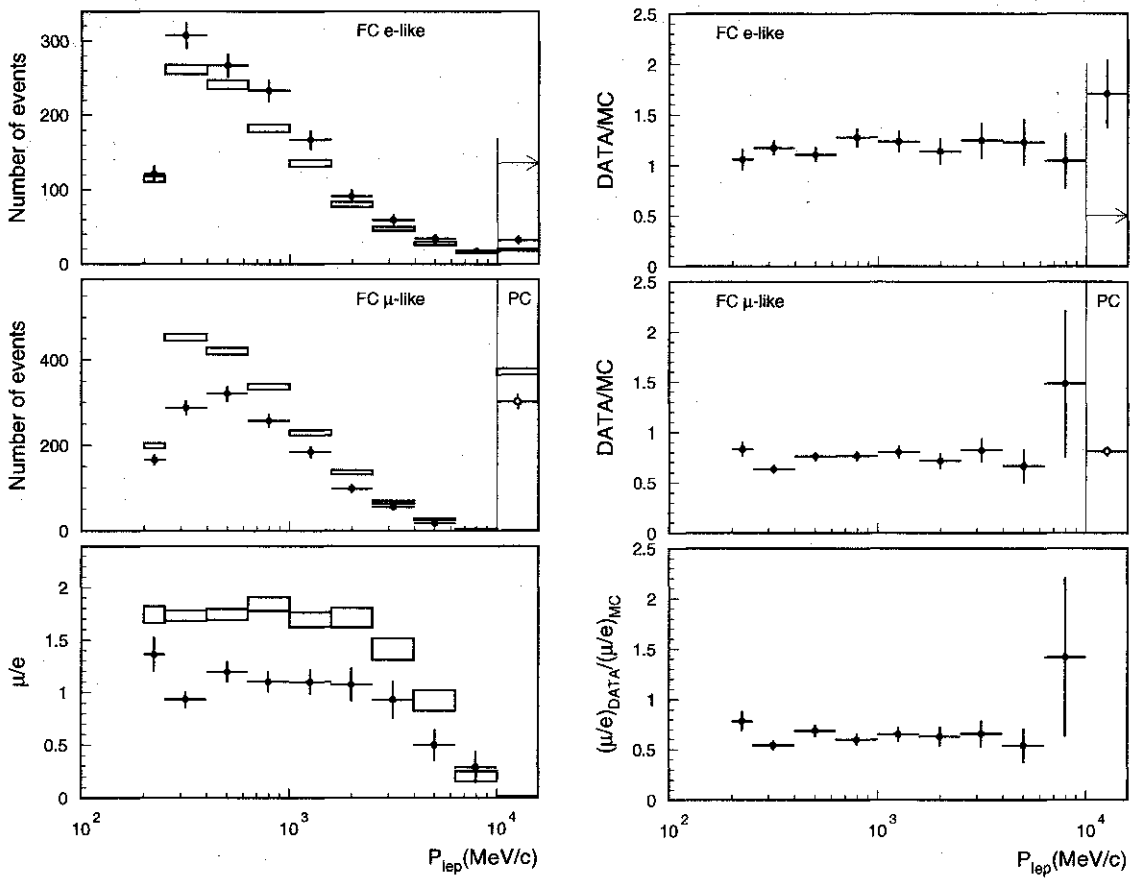

Figure 7.6: Momentum distribution for FC e-like and μ-like events, the μ/e ratio, the Data/MC ratio and the R distribution as a function of momentum. Box histogram shows the Monte Carlo prediction with the statistical error. PC events is also shown for comparison.

	sub-GeV	multi-GeV FC+PC
Reduction	$\ll 1$	3
$(\nu_\mu + \bar{\nu}_\mu)/(\nu_e + \bar{\nu}_e)$ neutrino flux	<5	<5
Energy spectrum of cosmic ray	0.6	1.6
PID	2	3
Single-Ring/multi-ring separation	3	6
Vertex position	0.6	2.4
Energy calibration	1	4
Non-neutrino background		
flashing PMT	<0.5	<0.5
cosmic ray muon	<0.1	0.6
e-like background	<0.1	0.1
Cross section	2.0	3.7
Hadron Simulation	0.5	1
FC/PC separation	<0.1	0.5
Total (%)	7	11
Monte Carlo statistical error (%)	1.5	2.9

Table 7.3: Summary of systematic error in R. Unit is (%).

- Reduction :

  The validity of the FC reduction was checked in the early days of the experiment by two independent reduction, one of which was based on the reduction method presented in this thesis. Comparing both final data sets, no events of the present data set in the fiducial volume were lost, therefore the systematic error in the FC reduction is expected to be very small ($\ll$1 %). As for PC reduction, the systematic uncertainty is estimated to be 5 % by changing the tuning of the outer detector simulation parameters. It contributes only about half of the muons in the multi-GeV sample, thus the systematic error in R_{FC+PC} is estimated to be 3%.

- $(\nu_\mu + \bar{\nu}_\mu)/(\nu_e + \bar{\nu}_e)$ neutrino flux :

  The uncertainties in the absolute electron and muon neutrino flux are estimated to be both about 20%, which comes mostly from that of primary cosmic-ray flux, however they are correlated each other and canceled largely when the ratio is taken. The uncertainly of $(\nu_\mu + \bar{\nu}_\mu)/(\nu_e + \bar{\nu}_e)$ is estimated to be <5%.

- Energy spectrum of cosmic ray :

  The spectrum of primary cosmic rays is well fit to a power law $E^{-\gamma}$ with spectral index $\gamma = 2.71 \pm 0.05$. The error of the spectral index affects the spectrum of the neutrino energy. The systematic uncertainty is estimated by changing the neutrino spectral index by $\pm$ 0.05. In practice, this was done by weighting each Monte Carlo events by the factor of $(E_\nu/2GeV)^{\pm 0.05}$, where 2 GeV corresponds to the approximate mean energy of the atmospheric neutrino events. R in sub-GeV (multi-GeV) is changed by 0.6% (1.6%) due to this effect.

- Particle Identification (PID) :

  The uncertainty in R caused by PID was estimated by the misidentification of the charged current quasi-elastic events. According to the Monte Carlo study, the misidentification probability is estimated as shown in Table 7.4. The error in PC events was considered to be 0 due to no application of the PID algorithm. The particle misidentification changes the μ/e ratio by up to twice as large as the misidentification probability, therefore the uncertainty is estimated to be 2% (3%) in the sub-GeV (multi-GeV) sample.

	$\mu \rightarrow$ e	e $\rightarrow \mu$	δR
sub-GeV	0.4 %	0.6 %	2 %
multi-GeV	1.4 %	0.3 %	3 %

Table 7.4: Misidentification probability of PID for the charged current quasi-elastic events, estimated by the atmospheric neutrino Monte Carlo simulation.

- Single-ring/multi-ring separation :

  Only the events with single Čerenkov ring were selected for the FC e-like and μ-like events. The number of rings in an events is obtained automatically by the Ring-counting program. In order to estimate the systematic uncertainty of the Ring-counting, the result was compared with that of a different version of the Ring-counting program and that of the human eye-scanning. The differences in sub-GeV and multi-GeV are estimated to be 3 % and 6 %, respectively, where the error for PC events is considered to be 0.

- Vertex position :

  The possible bias of the fiducial volume should be considered as the source of the systematic error. The final vertex position for FC events is determined by MS-fit. The uncertainty was estimated by comparing the result with that from the vertex position of TDC-fit. As for PC events, the vertex position of TDC-fit was adopted. The uncertainty was estimated by comparing the result with that of the interactive vertex fitter on a visual display. As a result, the differences in sub-GeV and multi-GeV R are estimated to be 0.6 % and 2 %.

- Energy calibration :

  The systematic uncertainties of the absolute energy scale was estimated by using the several calibration source, electron LINAC, muon-decay electron, atmospheric π^0 events and cosmic-ray muons. We concluded that the energy scale is understood to be within $\pm$ 2.5% uncertainty (see section 3.5). The uncertainty in R is estimated to be 1 % in sub-GeV and 4 % in multi-GeV, by shifting the energy scale within $\pm$ 2.5 %. As for PC events, the uncertainty is expected to be very small because the events of PC sample in the fiducial volume with less than 3000 p.e. is estimated to be <0.1 % of the total by the Monte Carlo simulation.

- Non-neutrino background :

We considered the effect of the flashing PMT events, cosmic-ray muons and e-like events induced by neutrons as the possible background.

We applied the FC 4th reduction for removing the flashing PMT events and furthermore checked by visual scanning. Therefore the contamination of the flashing PMT events is expected to be very small. We adopted <0.5% error conservatively for both sub-GeV and multi-GeV R.

We considered cosmic-ray muons as the background source of FC μ-like and PC events, and estimated the amount of cosmic-ray muon background using "Fromwall" distribution. Fromwall is defined as the distance of the vertex position from the inner detector wall along the particle direction, as shown in Fig 7.7. The Fromwall value should be small for cosmic-ray muons because the reconstructed vertex position of cosmic-ray muon should near the inner wall and the direction should face inward. Fig 7.8 shows the Fromwall distributions for sub-GeV μ-like, multi-GeV μ-like and PC events observed in the whole inner detector volume. The upper figure of each sample shows the data and Monte Carlo events. The peak near zero for multi-GeV μ-like events is due to the cosmic-ray muons which could not be eliminated by the reduction program because of the inefficiency of the outer detector. The middle figure shows the distribution for the cosmic-ray muons. In case of FC sample, most of these background are excluded from the fiducial volume because of the good vertex resolution (σ ~30cm), and the probability of missfitted in the fiducial volume is estimated to be 0.2%. On the other hand, due to the poorer vertex resolution, 20% of the background for PC sample could be missfitted in the fiducial volume. We estimated the amount of the background by a χ^2 test. The χ^2 value was calculated by comparing data with the combined distribution of the atmospheric neutrino Monte Carlo and background events. The 90% confidence level (C.L.) upper limit was regarded as the amount of the background. The lower figure of each sample shows the distribution at the 90% C.L. upper limit and the mesh region corresponds to the contribution of background. For sub-GeV and multi-GeV μ-like sample, most of them are out of the fiducial region, and the background contamination in the fiducial volume is estimated to be less than 0.1%. For PC sample, 1% of the background contamination is estimated by this method. Thus, the total background contamination in the multi-GeV μ-like and PC sample is estimated

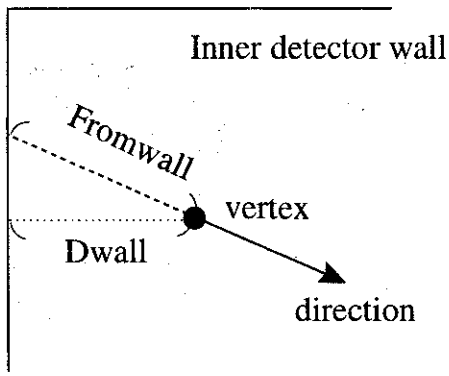

Figure 7.7: Definition of Fromwall.

to be less than 0.6%. As a result, the uncertainty of cosmic-ray muons affects on R by less than 0.1 (0.6) % for sub-GeV (multi-GeV) sample.

We also estimated the e-like background induced by neutrons which is produced by high energy cosmic-ray muons in the rock surrounding the detector. According to the Monte Carlo simulation of these neutrons, the attenuation length of the neutron-induced events was estimated to be about 44 (64) cm for sub-GeV (multi-GeV) sample. We estimated the neutron background contamination by using D_{wall} distribution instead of Fromwall distribution since the directional correlation between neutrons and secondary particles are rather poor (especially at low energies). The D_{wall} distribution of e-like events was fitted by a combined distribution of the neutrino-induced and neutron-induced events by a χ^2 method. From the χ^2 test, the contamination was estimated to be $\leq$0.1 % in sub-GeV and $\sim$0.1 % in multi-GeV.

- neutrino cross section :

  The uncertainties in R due to neutrino interaction cross section uncertainties were estimated for each interaction mode as follows: For quasi-elastic events, the effect on R was tested by changing the axial vector mass M_A by $\pm$ 10%, the Fermi motion P_F and the nuclear potential. For single-pion, multi-pion, coherent-pion production mode, the absolute cross section was varied by $\pm$ 30%, $\pm$ 40%, $\pm$ 30%, respectively. The relative error of neutral current cross section to charged current cross section is considered to be $\pm$ 20%. Table 7.5 shows the summary of the differences and the effect on R. In total, the

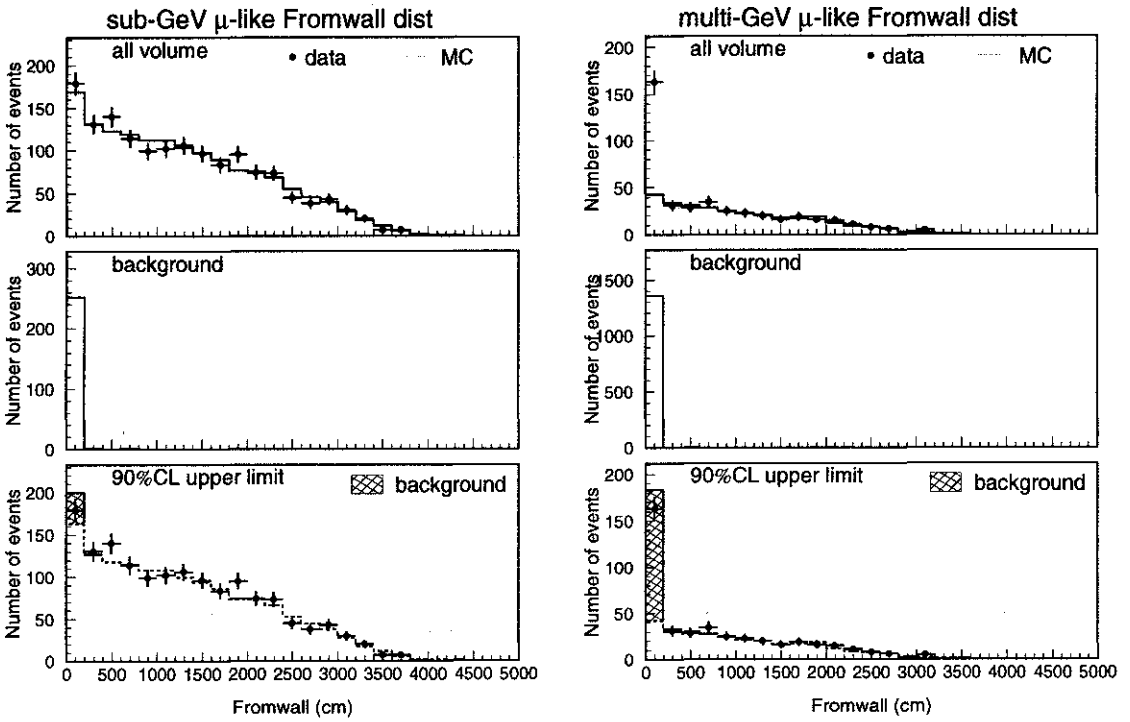

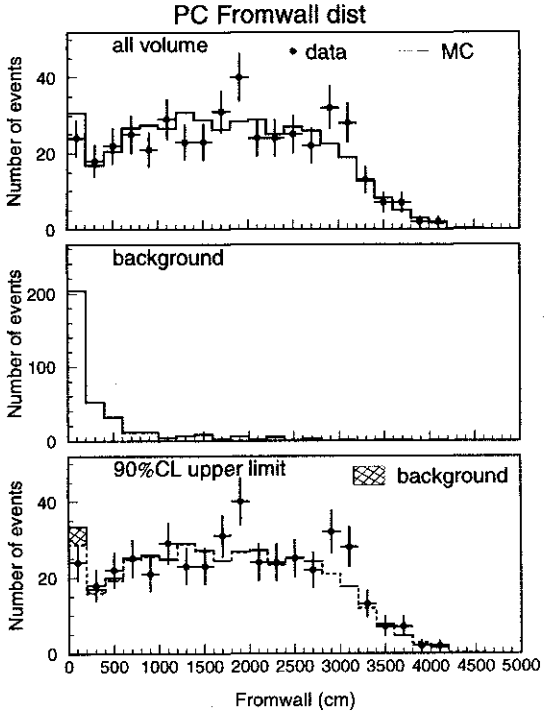

Figure 7.8: Fromwall distributions for sub-GeV μ-like (left upper), multi-GeV μ-like (right upper) and PC events (left lower). The upper figure of each sample shows the atmospheric neutrino data and Monte Carlo events in all volume. The middle figure shows the distribution for cosmic-ray muon background. The lower figure shows the combined distribution of atmospheric neutrino Monte Carlo and background at the 90% C.L. upper limit. The mesh area corresponds to the contribution of background.

	sub-GeV			multi-GeV		
	δ(e-like)	$\delta(\mu$-like)	δR	δ(e-like)	$\delta(\mu$-like)	δR
$M_A \pm 10\%$	$\pm$5.0%	$\pm$5.5%	$\pm$0.5%	$\pm$3.5%	$\pm$3.1%	$\pm$0.5%
$P_{fermi}(250 \rightarrow 180$ MeV)	+7.9%	+8.3%	-0.4%	+2.3%	+2.0%	-0.3%
V_{nucl} (off $\rightarrow$ on) ($P_{fermi} = 217$)	-1.2%	-1.3%	+0.1%	-0.4%	-0.3%	+0.1%
σ(single-π) $\pm$30%	$\pm$5.3%	$\pm$4.9%	$\pm$0.5%	$\pm$5.2%	$\pm$5.0%	$\pm$0.3%
σ(coherent-π) $\pm$30%	$\pm$1.2%	$\pm$0.7%	$\pm$0.5%	$\pm$1.3%	$\pm$0.7%	$\pm$0.6%
σ(multi-π) $\pm$40%	$\pm$3.5%	$\pm$2.1%	$\pm$1.4%	$\pm$15.6%	$\pm$18.6%	$\pm$3.2%
σ(NC)/σ(CC) $\pm$20%	$\pm$1.9%	$\pm$0.8%	$\pm$1.1%	$\pm$1.7%	$\pm$0.1%	$\pm$1.6%
total	$\pm$11.4%	$\pm$11.4%	$\pm$ 2.0%	$\pm$17.1%	$\pm$19.6%	$\pm$ 3.7%

Table 7.5: Summary of the systematic errors caused by the charged current and neutral current cross section uncertainties.

uncertainty in R was estimated to be 2.0 % for sub-GeV and 3.7 % for multi-GeV.

- Hadron simulator :

  We changed the hadron simulator package from CALOR to FLUKA and checked the effect on R to be 0.5% (1%) for sub-GeV (multi-GeV).

- FC/PC separation :

  The separation of FC and PC sample is based on the number of PMT hits in the outer detector hits (N_{hitac}) and made at 10 hits, as shown in Fig 7.1. The uncertainty was estimated to be <0.1 (0.5) % in sub-GeV (multi-GeV) sample by changing this separation point by $\pm$ 20 %.

Adding all of these errors in quadrature, the total systematic error in R is estimated to be 7 and 11 % for sub-GeV and multi-GeV samples, respectively. The Monte Carlo statistical error of 1.5 (2.9) % in sub-GeV (multi-GeV) sample was also included in the systematic error.

7.4 Zenith angle distribution

As mentioned in the introduction, the propagation length of the atmospheric neutrinos varies $15 \sim 13000$ km depending on the zenith angle of the neutrino direction, as shown in Fig 1.3. Therefore, if we know the direction of the incident neutrino, we can examine the neutrino oscillation which varies the oscillation probability as a function of the propagation length.

However, the direction of the leptons does not coincide with the incident neutrino direction exactly due to the momentum transfer to nucleons. Fig 7.9 shows the scattering angle of outgoing leptons as a function of the lepton momentum, for the Monte Carlo events induced via the charged current quasi-elastic interactions. From this figure, in the energy region of $\lesssim 0.5$ GeV/c, the charged lepton is scattered larger than 60°. But the correlation is better for the events with the higher lepton momentum. For the events of the lepton momentum, $P_{lep} \gtrsim 1$ GeV/c, we can estimate the neutrino direction within 30° from that of the lepton.

Fig 7.10 shows the zenith angle distribution for the sub-GeV and multi-GeV samples. The horizontal axis shows the cosine of the zenith angle of the particle direction, so that the solid angle of each bin is equal and the distribution should be flat when the neutrino flux is isotropic. $\cos\theta = -1$ shows upward-going particle and $\cos\theta = 1$ shows downward-going. Box histogram shows the Monte Carlo prediction. In the sub-GeV energy region, the neutrino flux is affected by the rigidity cutoff of the primary protons due to the geomagnetic field, as shown in Fig 1.4. But, because of the large correlation angle between neutrinos and leptons at low energies, up-down asymmetry cannot be seen clearly in the sub-GeV Monte Carlo events. The excess in the horizontal direction of multi-GeV sample is mostly due to the higher flux, which is due to the higher probability of decay in flight of high energy muons in the atmosphere for horizontal directions.

Comparing data with Monte Carlo, the deficit of the upward-going μ-like events is noticeable, especially in the multi-GeV sample. This effect can be seen more clearly in the ratio of data to Monte Carlo, as shown in Fig 7.11. As for the sub-GeV and multi-GeV e-like, the ratio is almost independent of the zenith angle. χ^2/d.o.f. values of a comparison of the data and a straight line are 6.8/4 for sub-GeV and 2.8/4 for multi-GeV. However, in the μ-like sample, the ratio for the upward direction is almost half of that for the downward direction. χ^2/d.o.f. values of the same test are 22.6/4 for sub-GeV and 29.5/4 for multi-GeV, whose probabilities are both less

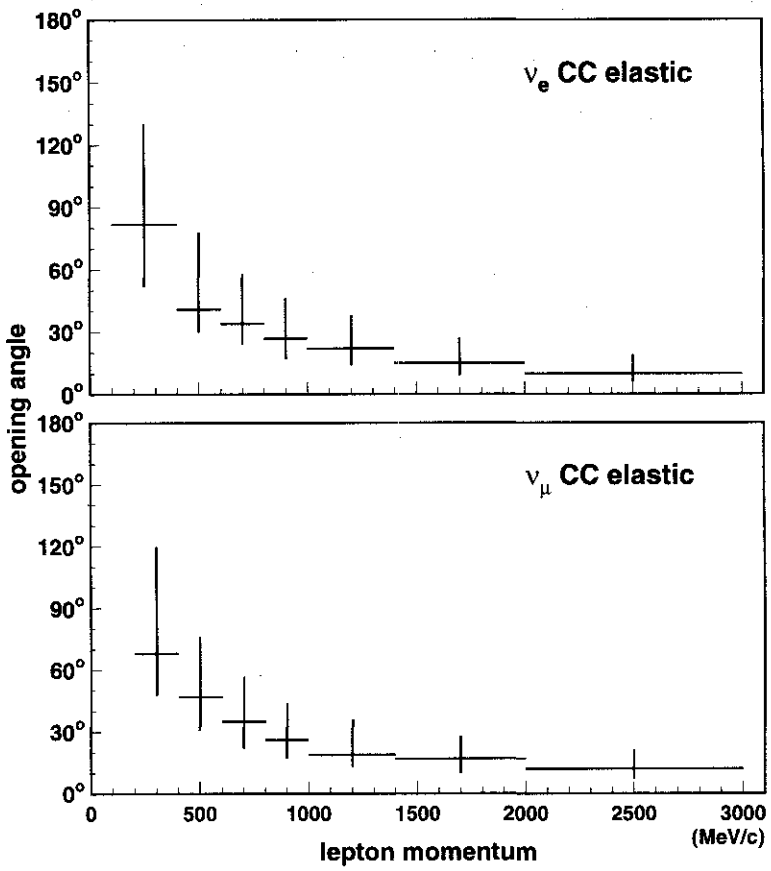

Figure 7.9: Distributions of the scattering angle of lepton with respect to the incident neutrino direction as a function of the lepton momentum, estimated by the Monte Carlo simulation. Only the charged current quasi-elastic interaction events are selected. The cross point shows the peak of the distribution at the corresponding momentum bin and error bar shows the region which contains the 68 % of the distribution.

than 0.1 %. The μ/e ratio and R as a function of the zenith angle are also shown in Fig 7.11. The values of χ^2/d.o.f. with respect to a flat line at the mean are 16.7/4 (sub-GeV) and 6.1/4 (multi-GeV).

Fig 7.12 shows the up-down asymmetry, (U-D)/(U+D), as a function of the lepton momentum. "U" is defined as the number of upward-going (-1< $\cos\theta$ <-0.2) events and "D" is the number of downward-going (0.2< $\cos\theta$ <1) events. Horizontal-going (-0.2< $\cos\theta$ <0.2) evens were excluded. As for e-like, the data is consistent with expectation in all energy region. However, for μ-like and PC sample, the up-down asymmetry is larger in the high momentum region and there is an obvious discrepancy between the data and Monte Carlo.

Table 7.6 shows the summary of the number of upward-going (U) and downward-going (D) events, up/down ratio, U/D and up-down asymmetry (U-D)/(U+D). The asymmetry for e-like events is consistent with expectations for both sub-GeV and multi-GeV, however, a significant asymmetry exists for μ-like events. The statistical significance of the asymmetry for μ-like is more than 3 σ for sub-GeV and 6 σ for multi-GeV.

7.5 Systematic uncertainty for up/down ratio

Most of the systematic errors are canceled when the up/down ratio is taken. We considered the up-down difference of the neutrino flux, non-neutrino background and energy scale as the possible sources of the systematic error for up/down ratio. Table 7.7 shows the summary of the systematic errors in the up/down ratio, U/D.

In order to estimate the uncertainty in the up/down ratio due to the neutrino flux, two calculated fluxes, Honda [30] and BGS [32] were compared. Additionally, the effect of 1 km mountain over Super-Kamiokande detector was included. The mountain stops muons before they can decay in flight and reduces the downward-going neutrino flux.

We measured the up-down energy scale difference of the detector using the muon-decay electrons. Muon-decay electrons whose direction is perpendicular to muon's were selected in order not to be affected by the polarization of muons. Fig 7.13 shows the mean momentum of the decay electrons as a function of the zenith angle of electron direction. $\pm$0.6 % difference of the energy-scale was measured between upward-going and downward-going electrons. It affects up/down ratio by $\pm$0.1 % ($\pm$0.9 %) for sub-GeV (multi-GeV) e-like events and $\pm$0.2 % ($\pm$0.7

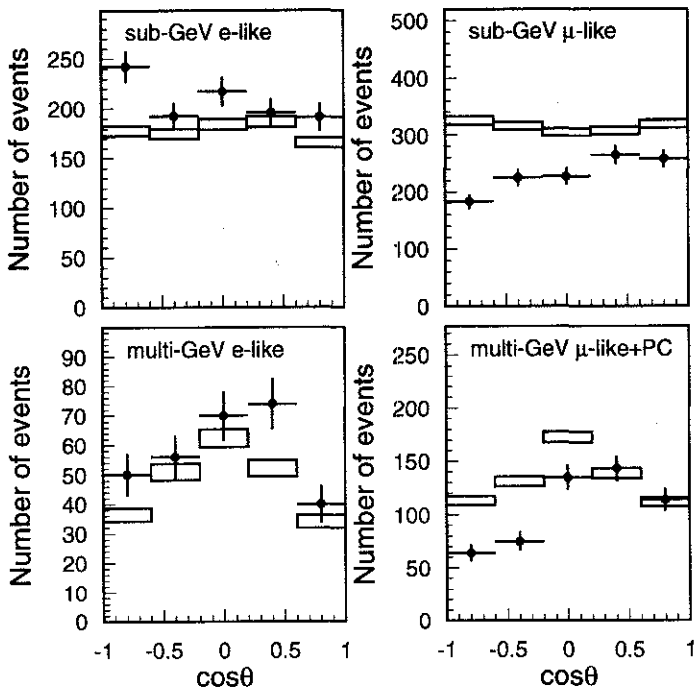

Figure 7.10: Zenith angle distribution for the atmospheric neutrino data (points) and Monte Carlo (box histogram) events. The horizontal axis shows the cosine of the zenith angle of the particle. $\cos\theta = -1$ shows the upward-going particle. The height of the box histogram shows the statistical error of Monte Carlo events.

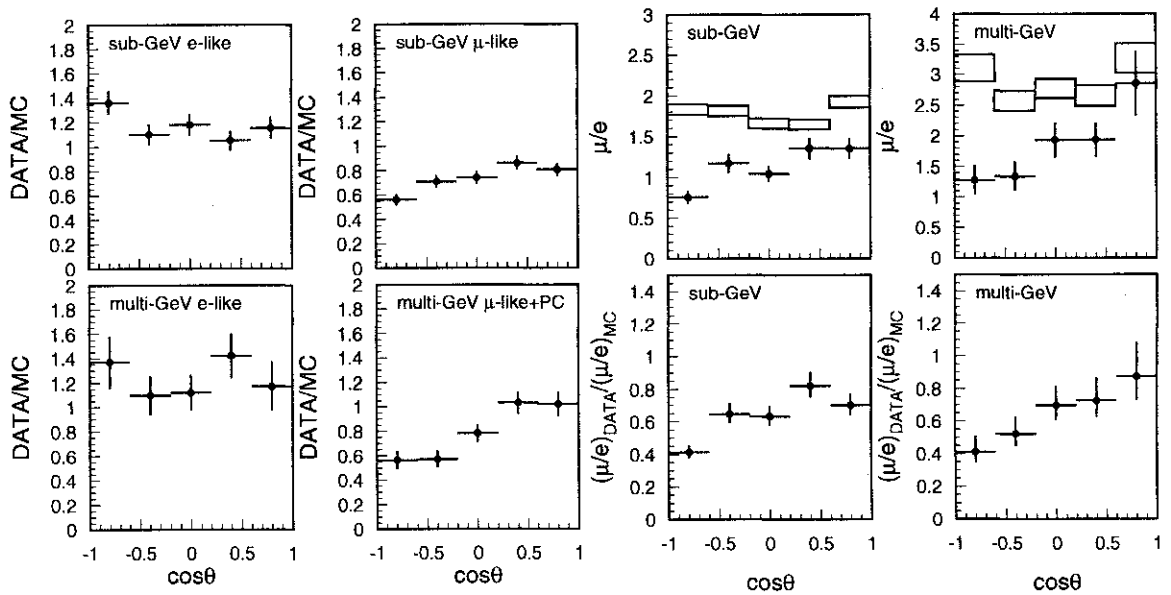

Figure 7.11: Ratio of data to Monte Carlo, μ/e ratio and R as a function of zenith angle. Box histogram in the μ/e ratio shows the Monte Carlo prediction.

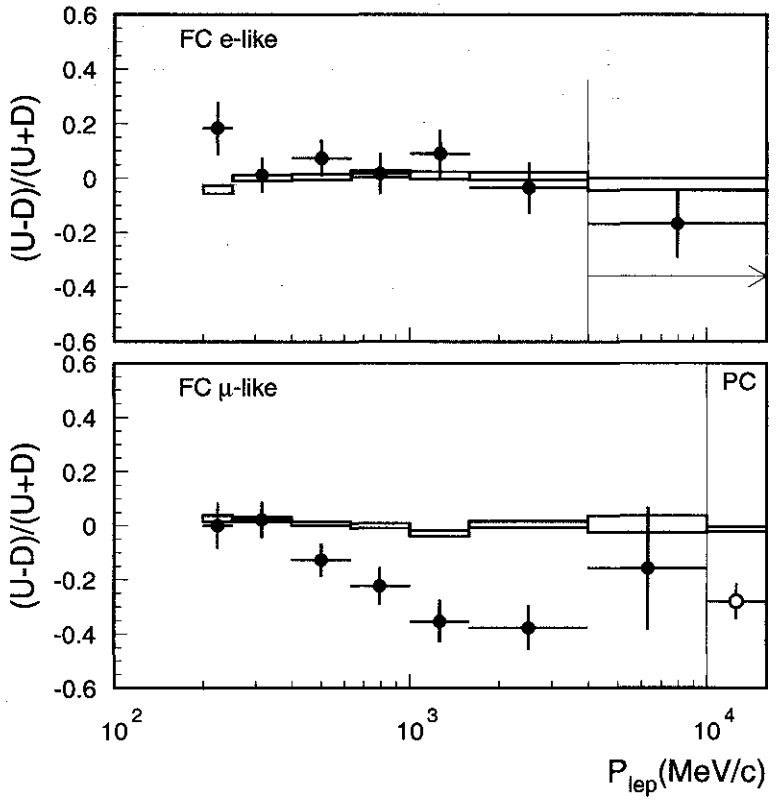

Figure 7.12: Up-down asymmetry as a function of the lepton momentum for the atmospheric neutrino data (points) and Monte Carlo (box histogram) events. "U" is defined as the number of upward-going (-1< $\cos\theta$ <-0.2) events and "D" is the number of downward-going (0.2< $\cos\theta$ <1) events. The height of the box shows the statistical error. PC events are also shown in this figure for comparison.

		U	D	U/D	(U-D)/(U+D)
sub-GeV					
data	e-like	424	363	$1.14^{+0.09}_{-0.08} \pm 0.01$	$0.067 \pm 0.035 \pm 0.01$
	μ-like	409	521	$0.78^{+0.05}_{-0.05} \pm 0.01$	$-0.123 \pm 0.033 \pm 0.01$
Monte Carlo	e-like	341.9	345.6	$0.99^{+0.03}_{-0.03} \pm 0.03$	$-0.005 \pm 0.015 \pm 0.01$
	μ-like	633.9	621.3	$1.02^{+0.02}_{-0.02} \pm 0.02$	$0.010 \pm 0.011 \pm 0.01$
multi-GeV					
data	e-like	106	114	$0.93^{+0.13}_{-0.12} \pm 0.01$	$-0.036 \pm 0.067 \pm 0.01$
	μ-like (FC+PC)	140	262	$0.53^{+0.06}_{-0.05} \pm 0.01$	$-0.303 \pm 0.048 \pm 0.01$
Monte Carlo	e-like	87.3	86.3	$1.01^{+0.06}_{-0.06} \pm 0.03$	$0.006 \pm 0.029 \pm 0.01$
	μ-like (FC+PC)	248.8	252.3	$0.99^{+0.03}_{-0.03} \pm 0.02$	$-0.007 \pm 0.017 \pm 0.01$

Table 7.6: Summary of the number of the upward-going and downward-going events and the up/down ratio. Upward-going (downward-going) events are those with zenith angle -1< $\cos\theta$ <-0.2 (0.2< $\cos\theta$ <1). The up-down asymmetries (U-D)/(U+D) are also shown with their statistical and systematic errors.

	sub-GeV			multi-GeV		
	e-like	μ-like	μ/e	e-like	μ-like	μ/e
Theoretical						
Neutrino flux	$\pm$2.5	$\pm$2.1	$\pm$0.4	$\pm$2.6	$\pm$1.8	$\pm$1.7
Total	$\pm$2.5	$\pm$2.1	$\pm$0.4	$\pm$2.6	$\pm$1.8	$\pm$1.7
Experimental						
Energy scale	$\pm$0.1	$\pm$0.2	$\pm$0.2	$\pm$0.9	$\pm$0.7	$\pm$0.3
Non-neutrino background	$\pm$1.0	$\pm$0.1	$\pm$1.0	$\pm$0.5	$\pm$1.2	$\pm$1.3
Total	$\pm$1.0	$\pm$0.2	$\pm$1.0	$\pm$1.0	$\pm$1.4	$\pm$1.3

Table 7.7: Summary of the systematic errors for the up/down ratio, U/D. Unit is percent(%).

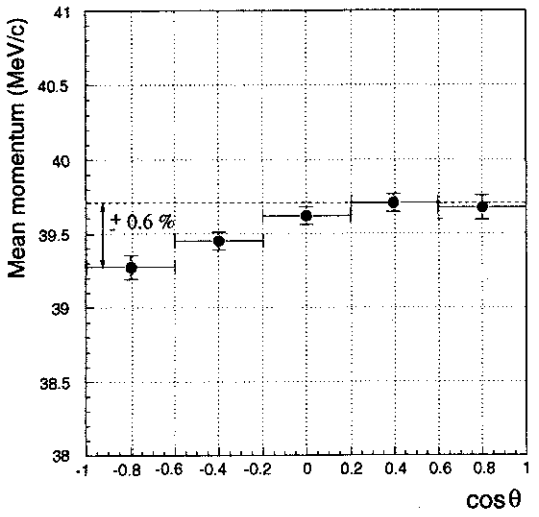

Figure 7.13: Mean momentum of the muon-decay electron as a function of the zenith angle of the electron direction.

%) for μ-like events. PC events was affected by less than 0.1 % for the up-down energy scale difference due to the loose cut on total photoelectrons.

The non-neutrino background such as cosmic-ray muons could be considered to contaminate mostly the downward-going neutrino events. Therefore we estimated its uncertainty by assuming that all these events are contaminated in either downward-going or upward-going direction.

Chapter 8

Oscillation analysis

The deficit of the upward-going muons in the multi-GeV energy region is obvious by the discussion of the previous section. Considering the fact that the up-down asymmetry of multi-GeV e-like events agrees with the expectation, the $\nu_\mu \leftrightarrow \nu_\tau$ oscillation mode seems to be dominant for the atmospheric neutrinos. However, as described in the introduction, there is some possibility of existing other sub-channels if the mixing angle θ_{13} is not 0. In this section, we will perform the 2-flavor oscillation analysis ($\nu_\mu \leftrightarrow \nu_\tau$) and the 3-flavor oscillation analysis using the atmospheric neutrino data and attempt to determine the oscillation parameters (Δm^2, θ_{23}, θ_{13}).

8.1 Analysis method

We have divided the data into 65 and 5 bins for FC and PC events (70 bins total), respectively, according to the lepton momentum, P, and zenith angle, $\cos\theta$, as shown in Fig 8.1.

The oscillation analysis is based on a χ^2 examination of these distributions. χ^2 is defined as follows:

$$\chi^2 = \sum_{\cos\theta,p} \frac{(N_{DATA} - N_{MC})^2}{\sigma^2} + \sum_j \frac{\epsilon_j^2}{\sigma_j^2} \tag{8.1}$$

where N_{DATA} is the measured number of events in each ($\cos\theta$, P) bin, and σ is the statistical error of both the data and Monte Carlo. ϵ_j, σ_j are the Monte Carlo parameters related to the measurement systematic errors and its uncertainties, respectively. The assigned meaning and uncertainties are summarized in Table 8.1.

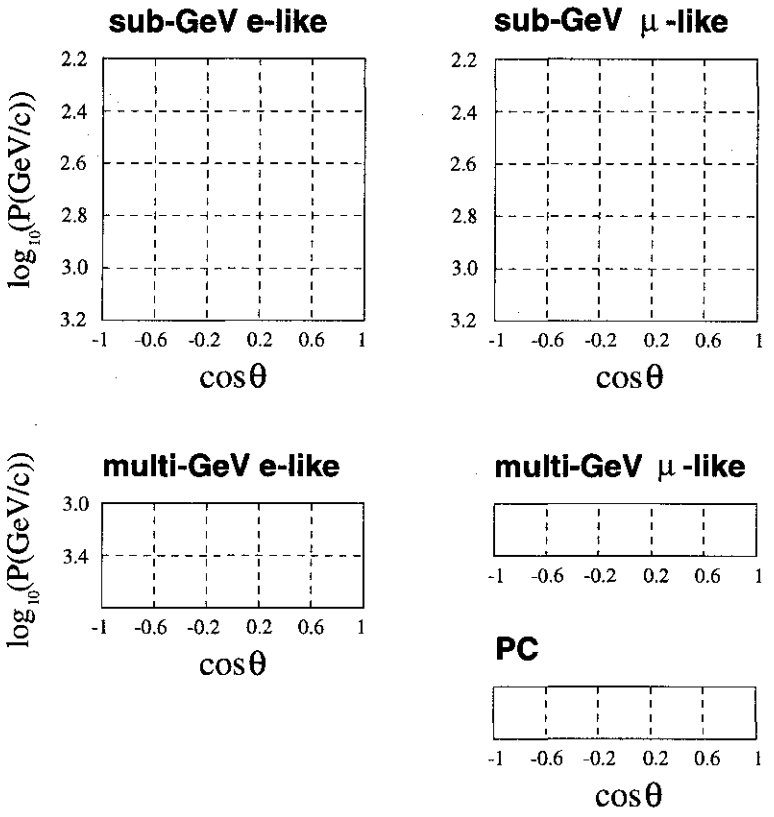

Figure 8.1: Definition of the bins for the oscillation analysis. They are divided according to the momentum, P, and zenith angle, $\cos\theta$. 35 bins for FC e-like events, 30 bins for FC μ-like events and 5 bins for PC events, in total 70 bins are prepared.

	Monte Carlo Fit Parameters (ϵ_j)	Uncertainty (σ_j)
α	overall normalization	free (25%)
β_s	sub-GeV μ/e ratio	7%
β_m	multi-GeV μ/e ratio	11%
δ	E_ν spectral index	0.05%
ρ	relative normalization of PC to FC	8%
η_s	sub-GeV zenith shape	2.5%
η_m	multi-GeV zenith shape	2.7%

Table 8.1: Summary of Monte Carlo parameters. The meaning and uncertainty is given for each parameter.

N_{MC} is the expected number of events for the specified oscillation parameters (Δm^2, θ_{23}, θ_{13}), including the weight caused by the systematic uncertainties. It is given by

$$N_{MC} = (1+\alpha)(\frac{E_\nu^i}{E_0})^\delta(1+\frac{\eta_{s,m}}{2})\frac{\mathcal{L}_{data}}{\mathcal{L}_{MC}}N_{exp}(\Delta m^2,\theta_{23},\theta_{13})$$

$$\times\begin{cases}(1-\frac{\beta_s}{2}) & \text{sub-GeV e-like}\\ (1+\frac{\beta_s}{2}) & \text{sub-GeV } \mu\text{-like}\\ (1-\frac{\beta_m}{2}) & \text{multi-GeV e-like}\\ (1+\frac{\beta_m}{2})(1-\frac{\rho}{2}\frac{N_{PC}}{N_\mu}) & \text{multi-GeV } \mu\text{-like}\\ (1+\frac{\beta_m}{2})(1+\frac{\rho}{2}) & \text{PC}\end{cases}$$

where α, β_s, β_m, δ, ρ, η_s, η_m are the Monte Carlo parameters listed in Table 8.1. E_ν^i is the mean neutrino energy for the corresponding momentum bin and E_0 is 2 GeV as the mean neutrino energy of the whole events. $\mathcal{L}_{data}$ and $\mathcal{L}_{MC}$ are the livetime of the data and Monte Carlo, respectively. $N_{exp}(\Delta m^2,\theta_{23},\theta_{13})$ is the expected number of events without the systematic uncertainties and given by

$$N_{exp}(\Delta m^2, \theta_{23}, \theta_{13}) = \begin{cases} \sum_{\mathrm{NC,FCe}} + \sum_{\mathrm{CC,FCe}} \mathrm{P}(\nu_e \to \nu_e) + \sum_{\mathrm{CC,FC}\mu\mathrm{,PC}} \frac{\varepsilon_{\mathrm{FCe}}}{\varepsilon_{\mathrm{FC}\mu} + \varepsilon_{\mathrm{PC}}} \mathrm{P}(\nu_\mu \to \nu_e) & \text{(FC e-like)} \\ \sum_{\mathrm{NC,FC}\mu} + \sum_{\mathrm{CC,FC}\mu} \mathrm{P}(\nu_\mu \to \nu_\mu) + \sum_{\mathrm{CC,FCe}} \frac{\varepsilon_{\mathrm{FC}\mu}}{\varepsilon_{\mathrm{FCe}}} \mathrm{P}(\nu_e \to \nu_\mu) & \text{(FC } \mu\text{-like)} \\ \sum_{\mathrm{NC,PC}} + \sum_{\mathrm{CC,PC}} \mathrm{P}(\nu_\mu \to \nu_\mu) + \sum_{\mathrm{CC,FCe}} \frac{\varepsilon_{\mathrm{PC}}}{\varepsilon_{\mathrm{FCe}}} \mathrm{P}(\nu_e \to \nu_\mu) & \text{(PC)} \end{cases}$$

where NC(CC) shows the neutral current (charged current) events and FCe (FCμ) shows the fully-contained e-like (μ-like) events. $\mathrm{P}(\nu_\alpha \to \nu_\beta)$ is the oscillation probability that ν_α oscillates to ν_β in each event, as function of neutrino energy E_ν, flight length L and the oscillation parameters $(\Delta m^2, \theta_{23}, \theta_{13})$. $\varepsilon_{\mathrm{FCe}}$, $\varepsilon_{\mathrm{FC}\mu}$ and $\varepsilon_{\mathrm{PC}}$ show the detection efficiency of FC e-like, FC μ-like and PC events as a function of the incident neutrino energy E_ν, as shown in Fig 8.2. It is introduced to correct for the difference of efficiency in each sample. The distribution of the production height calculated in Ref [73] is used for the neutrino flight length L.

The effect of matter on the neutrino oscillation is included in this oscillation analysis. We used the five step function for the density profile of matter inside the Earth, as shown in Fig 8.3.

The region of the tested oscillation parameters were $10^{-4} < \Delta m^2 < 0.1$, $0 < \sin^2\theta_{23,31} < 1$. 61 $\times$ 41 $\times$ 41 points were picked up from this region. At each point, χ^2 value was minimized by changing the Monte Carlo parameters ϵ_j.

8.2 2-flavor oscillation analysis ($\nu_\mu \leftrightarrow \nu_\tau$)

First of all, we carried out the pure $\nu_\mu \leftrightarrow \nu_\tau$ oscillation analysis. Fig 8.4 shows the allowed region of the oscillation parameters. The pure $\nu_\mu \leftrightarrow \nu_\tau$ is realized at θ_{13}=0 in 3-flavor oscillation. θ_{23} became the only mixing angle and replaced with θ. The MSW effect is not relevant in this oscillation mode because electron neutrinos does not take part in the oscillation. The horizontal axis is expressed by $\sin^2 2\theta$, similar to the usual 2-flavor oscillation analysis.

χ^2 minimum is 69.7/67 d.o.f. at $(\Delta m^2, \sin^2 2\theta) = (2.1 \times 10^{-3}, 0.97)$. The 90 % (99 %) confidence level (C.L.) allowed region is defined as the region whose χ^2 difference from the minimum χ^2 value is less than 4.6 (9.2). The region of $8 \times 10^{-4} < \Delta m^2 < 6 \times 10^{-3}$ eV^2 and $\sin^2 2\theta > 0.79$ is allowed at 90 % C.L..

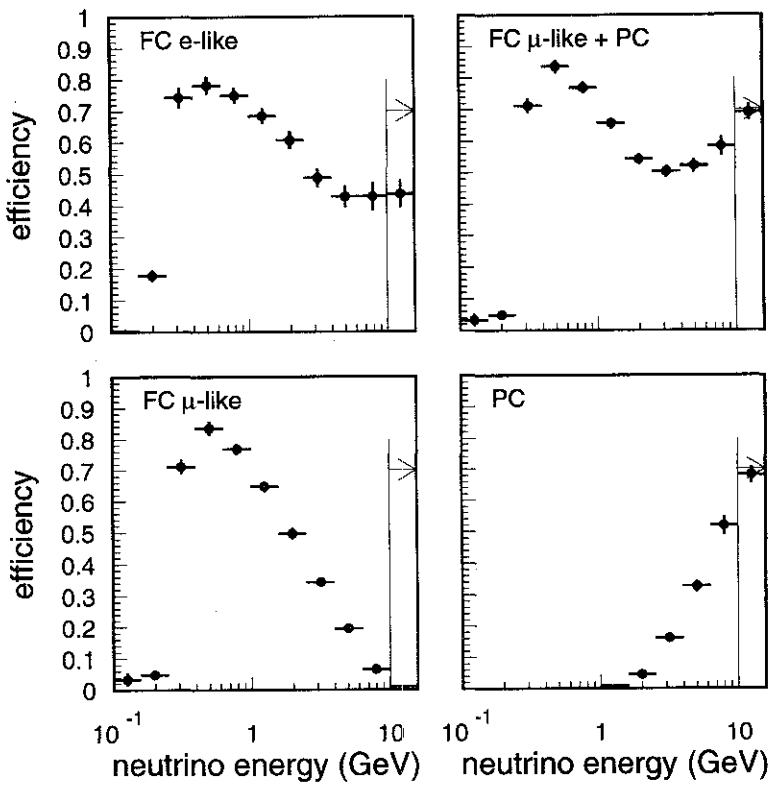

Figure 8.2: Detection efficiency of FC e-like, FC μ-like and PC events as a function of the incident neutrino energy, estimated by the Monte Carlo simulation. Only events induced by the charged current ν_e (FC e-like) and ν_μ (FC μ-like, PC) interactions are used.

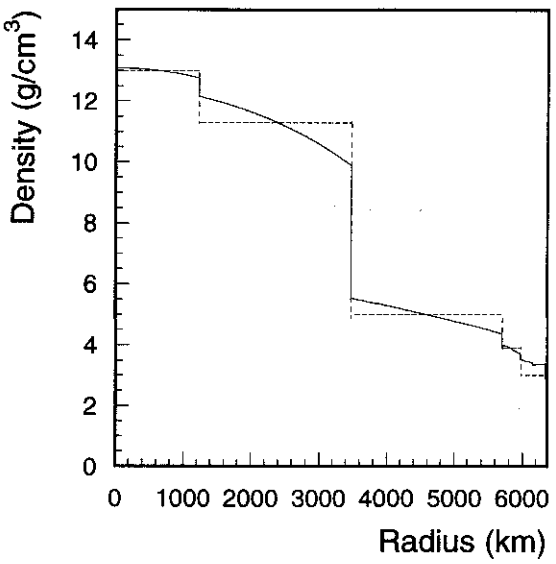

Figure 8.3: Matter density inside the Earth as a function of the radius. Solid line was taken from Ref [74] and dashed line shows the five step functions used in the oscillation analysis.

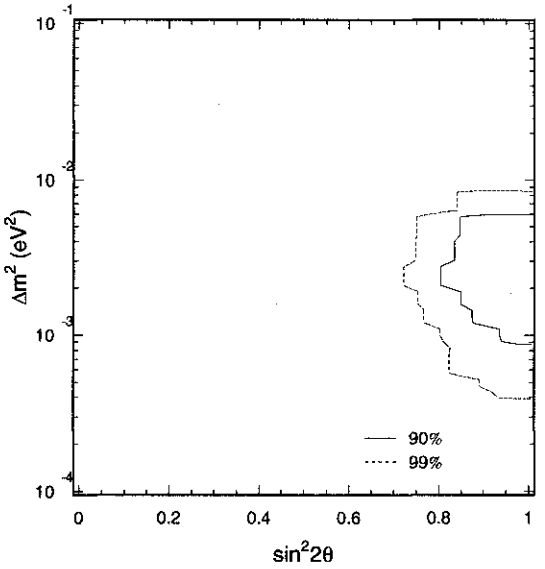

Figure 8.4: Allowed region for oscillation parameters, (Δm^2,$\sin^2 2\theta$), in $\nu_\mu \leftrightarrow \nu_\tau$ oscillation mode. The region inside the solid (dashed) line is allowed at 90 % (99 %) confidence level (C.L.).

8.3 3-flavor oscillation analysis with one mass scale dominance

The 3-flavor oscillation analysis is much complicated than the $\nu_\mu \leftrightarrow \nu_\tau$ 2-flavor analysis. Though we assume one mass scale dominance for simplicity, all oscillation channels of $\nu_e \leftrightarrow \nu_\mu$, $\nu_\mu \leftrightarrow \nu_\tau$ and $\nu_e \leftrightarrow \nu_\tau$ are open with the two mixing angle, θ_{23} and θ_{13}. Furthermore, the MSW effect should be considered.

Fig 8.5 shows the allowed region of oscillation parameters. The allowed region in 3-flavor oscillation is a function of 3 parameters, $(\Delta m^2, \theta_{23}, \theta_{13})$, therefore the allowed region is expressed by the projection onto $(\sin^2\theta_{23},\Delta m^2)$ and $(\sin^2\theta_{13},\Delta m^2)$ planes, as shown in Fig 8.5. The horizontal axis is expressed by $\sin^2\theta$, not $\sin^2 2\theta$, because the asymmetry of the oscillation probability for $\theta_{23,13} \leftrightarrow \pi/2 - \theta_{23,13}$ is broken in 3-flavor oscillation.

The 90 % (99 %) allowed region is defined that the χ^2 difference from the minimum χ^2 is less than 6.3 (11.3) because the number of free parameters is three. The minimum χ^2 value, χ^2_{min}, is 65.7/66 d.o.f. at $(\Delta m^2,\ \sin^2\theta_{23},\ \sin^2\theta_{13}) = (2.2\times10^{-3},\ 0.68,\ 0.20)$. The region of $0.33 < \sin^2\theta_{23} < 0.87$ is allowed at 90 % C.L., which corresponds to $0.45 < \sin^2 2\theta_{23} < 1.0$. It is found that the constraint on θ_{13} is weak and the large region of θ_{13} is allowed ($\sin^2\theta_{13} < 0.75$ at 90 % C.L.). Corresponding to the large θ_{13}, a large Δm^2 region, relative to the 2-flavor $\nu_\mu \leftrightarrow \nu_\tau$ oscillation region, is allowed ($9 \times 10^{-4} < \Delta m^2 < 2.5 \times 10^{-2}$ eV^2 at 90 % C.L.). The allowed region in large Δm^2 will be discussed later.

Fig 8.6 shows the χ^2-χ^2_{min} as a function of the mixing angle. Pure $\nu_\mu \leftrightarrow \nu_\tau$ oscillation is realized at $\sin^2\theta_{13} = 0$ and its minimum χ^2 is 69.7, as described in the previous section. The χ^2 difference between the global minimum and the minimum at $\theta_{13} = 0$ is 4.0, which corresponds to the probability of 26 %. Therefore pure $\nu_\mu \leftrightarrow \nu_\tau$ oscillation is consistent with 3-flavor oscillation within 90 % C.L.. 3-flavor oscillation corresponds to pure $\nu_\mu \leftrightarrow \nu_e$ when $\sin^2\theta_{23} = 1$ is taken. The χ^2 minimum for this oscillation is 90.1/66 d.o.f., which is larger than the global χ^2 minimum by 24.4, less than 0.01 % probability. Therefore pure $\nu_\mu \leftrightarrow \nu_e$ oscillation is excluded more than 99.99 % C.L..

Fig 8.7 shows the zenith angle and up-down asymmetry distributions with the expected distributions at the χ^2 minimum points in 2-flavor ($\nu_\mu \leftrightarrow \nu_\tau$) and 3-flavor oscillation analysis. For μ-like, the expected distribution explains the deficit of upward-going muon events excellently. Therefore it gives the strong evidence of the muon neutrino oscillations. For e-like, the slight

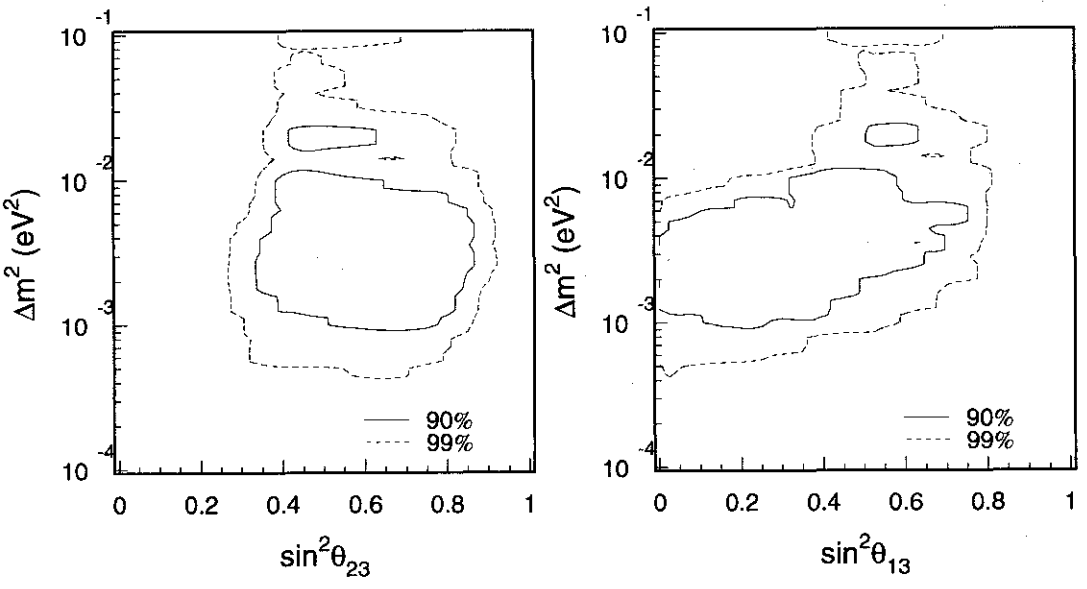

Figure 8.5: Figures of the allowed region projected onto ($\sin^2\theta_{23}$,Δm^2) (left) and ($\sin^2\theta_{13}$,Δm^2) (right). The regions inside solid (dashed) lines are allowed from the result of the atmospheric neutrinos at 90% (99%) confidence level.

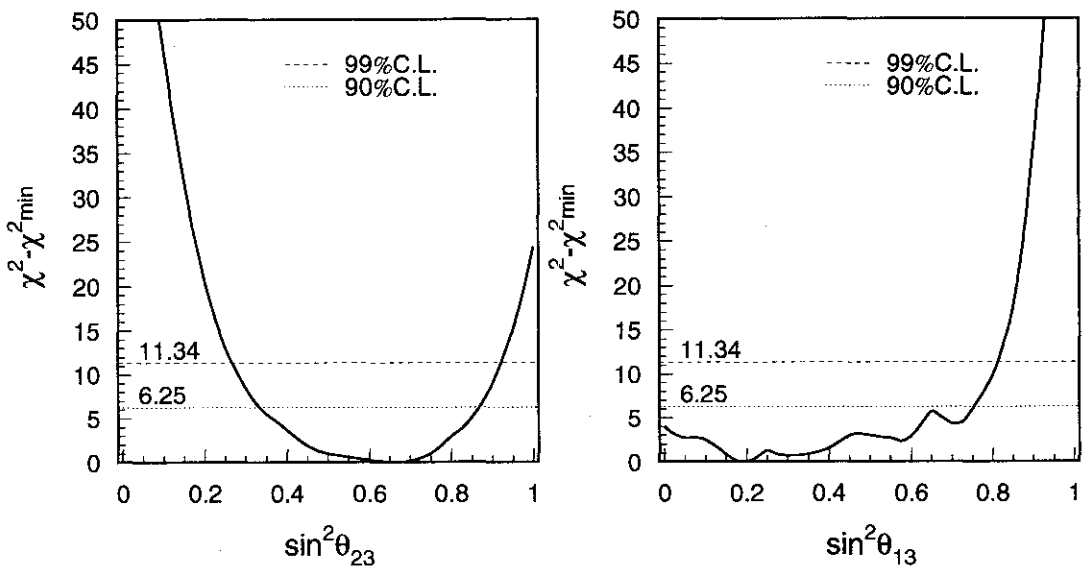

Figure 8.6: χ^2-χ^2_{min} as a function of $\sin^2\theta_{23}$ (left) or $\sin^2\theta_{13}$ (right). $\sin^2\theta_{13} = 0$ ($\sin^2\theta_{23} = 1$) corresponds to pure $\nu_\mu \leftrightarrow \nu_\tau$ ($\nu_\mu \leftrightarrow \nu_e$). The minimum χ^2 value is taken for each $\sin^2\theta_{23}/\sin^2\theta_{13}$ with the other oscillation parameters unconstrained. Dotted (dashed) line shows the 90% (99%) C.L. level.

excess of upward-going events is seen in the expectation of 3-flavor oscillation result. It is caused by the sub-channel of $\nu_\mu \leftrightarrow \nu_e$ oscillation due to the non-zero value of θ_{13}. But, according to the up-down asymmetry of the observed e-like events there is no strong evidence for non-zero θ_{13}.

Fig 8.8 shows the $(\chi^2 - \chi^2_{min})$ values , as a function of the mass square difference, Δm^2, for 3-flavor and 2-flavor $\nu_\mu \leftrightarrow \nu_\tau$ oscillation analysis. The minimum χ^2 value for each Δm^2 is searched for by scanning the mixing angles. For 2-flavor oscillation, there is a large wall of χ^2 value in the region of $\Delta m^2 > 10^{-2}$ eV^2 and this region is excluded with more than 99 % C.L.. On the other hand, for 3-flavor oscillation, the region of $10^{-2} < \Delta m^2 < 10^{-1}$ eV^2 is allowed at 99 % C.L..

Fig8.9 shows the expected up-down asymmetry, as a function of Δm^2 for 3-flavor oscillation and 2-flavor $\nu_\mu \leftrightarrow \nu_\tau$ oscillation. For e-like, the increase of up-down asymmetry in 3-flavor oscillation is caused by the excess of upward-going events due to the sub-channel of $\nu_\mu \leftrightarrow \nu_e$ oscillation. Furthermore, the MSW effect enhanced the $\nu_\mu \leftrightarrow \nu_e$ oscillation in multi-GeV energy region since the neutrino of the energy 1~10 GeV is affected by the MSW effect in $10^{-3} < \Delta m^2 < 10^{-2}$ eV^2 according to the MSW condition $\Delta m^2 \sim A$ (see section 1.4.2).

For μ-like, the behavior of up-down asymmetry in the large region of $\Delta m^2 > 10^{-2}$ eV^2 is significantly different between 3-flavor and 2-flavor oscillation. In 2-flavor $\nu_\mu \leftrightarrow \nu_\tau$ oscillation, the up-down asymmetry is closer to 0 in the large Δm^2 region because the downward-going muon neutrinos also oscillate to tau neutrinos due to the shorter oscillation length. This effect does not allow the large Δm^2 region of $> 10^{-2}$ eV^2 in 2-flavor $\nu_\mu \leftrightarrow \nu_\tau$ oscillation. In 3-flavor oscillation, the expected up-down asymmetry is consistent with the measured value within the error in the large Δm^2 region. This is caused by the fact that the probability of the $\nu_\mu \rightarrow \nu_\mu$ transition can be less than 0.5 for the upward-going muon neutrinos due to the 3-flavor matter oscillation in the condition of $\Delta m^2 \gg A$. (see section 1.4.3). This effect keeps the large up-down asymmetry for sub-GeV and multi-GeV μ-like events and allows the $\Delta m^2 > 10^{-2}$ region with a slightly lower probability (i.e., allowed at 99 % C.L.).

8.4 Comparison with other experiments

Fig 8.10 shows the allowed region expressed by $\sin^2 2\theta$ for (a) $\nu_e \rightarrow \nu_e$, (b) $\nu_\mu \rightarrow \nu_\mu$, (c) $\nu_\mu \rightarrow \nu_e$ and (d) $\nu_\mu \rightarrow \nu_\tau$ transition at 90 % C.L.. Each $\sin^2 2\theta$ is given by the following equations

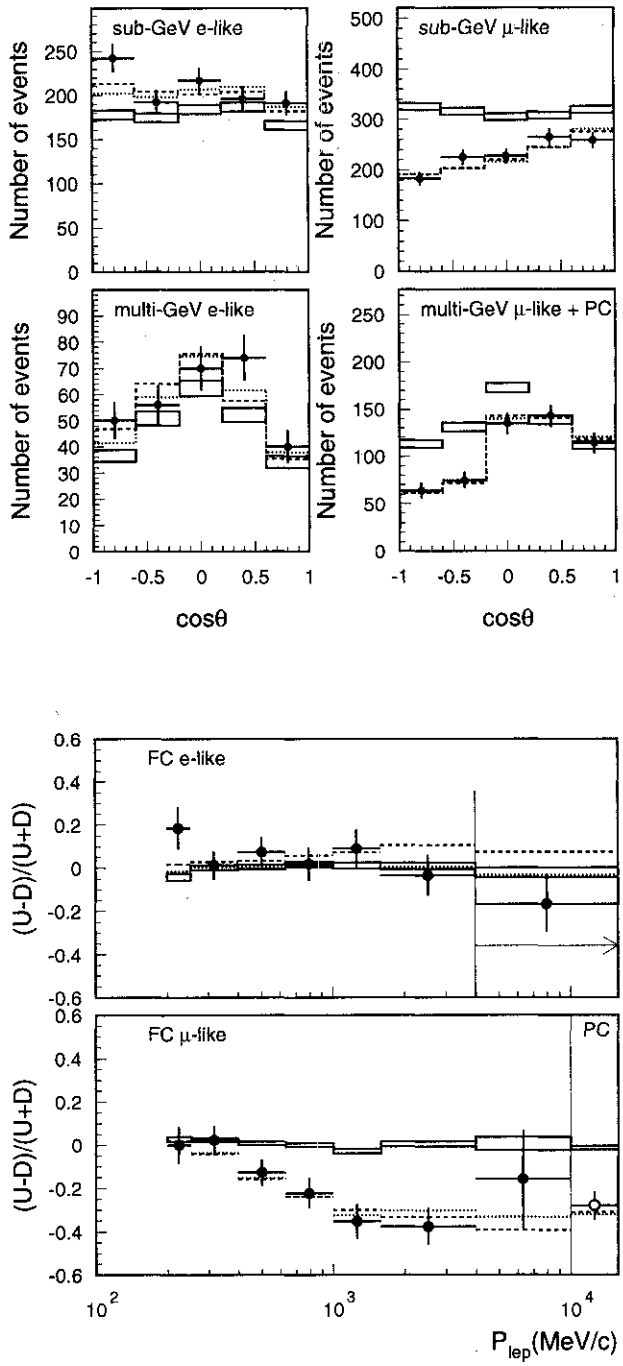

Figure 8.7: Distributions of zenith angle and up-down asymmetry with expectation. Dashed line shows the expectation in 3-flavor oscillation at the global χ^2 minimum point (Δm^2, $\sin^2\theta_{23}$, $\sin^2\theta_{13}$) = (2.2×10^{-3}, 0.68, 0.20). Dotted line shows that of 2-flavor $\nu_\mu \leftrightarrow \nu_\tau$ at the χ^2 minimum point (Δm^2, $\sin^2 2\theta$) = (2.1×10^{-3}, 0.97).

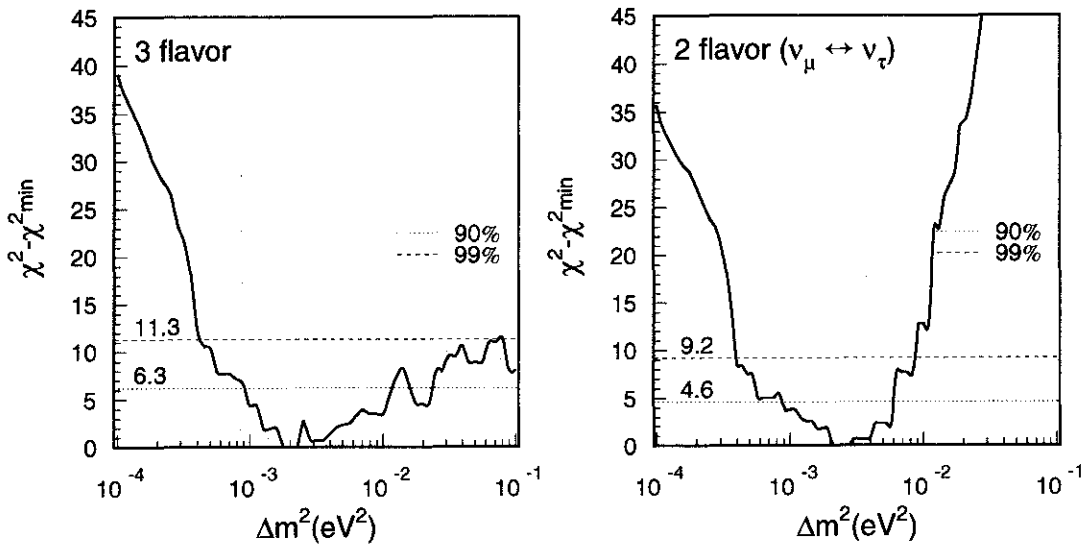

Figure 8.8: $\chi^2 - \chi^2_{min}$ as a function of the mass square difference Δm^2, for 3-flavor (left) and 2-flavor $\nu_\mu \leftrightarrow \nu_\tau$ (right) oscillation. The minimum χ^2 value is taken for each Δm^2 with the mixing angles unconstrained.

according to (1.22) and (1.23):

$$\begin{aligned}
\sin^2 2\theta_{ee} &= \sin^2 2\theta_{13} \\
\sin^2 2\theta_{\mu\mu} &= \cos^2\theta_{13}\sin^2 2\theta_{23} + \sin^2 2\theta_{13}\sin^4\theta_{23} \\
\sin^2 2\theta_{\mu e} &= \sin^2\theta_{23}\sin^2 2\theta_{13} \\
\sin^2 2\theta_{\mu\tau} &= \cos^4\theta_{13}\sin^2 2\theta_{23}
\end{aligned}$$

The allowed regions of the large $\sin^2 2\theta_{ee}$, $\sin^2 2\theta_{\mu e}$ and small $\sin^2 2\theta_{\mu\tau}$ are due to the large allowed θ_{13} in 3-flavor oscillation analysis.

The information from the other neutrino oscillation experiments using accelerator and reactor can be compared with these allowed regions. In $\nu_e \to \nu_e$ transition, CHOOZ [75], which observed the $\bar{\nu}_e$ from reactor, excluded $\sin^2 2\theta_{ee} \gtrsim 0.2$ at large Δm^2 and $\Delta m^2 \gtrsim 10^{-3}$ eV^2 at $\sin^2 2\theta_{ee} = 1.0$, as shown in Fig 8.10(a). According to it, the region of $\sin^2\theta_{13} > 0.05$ in the large Δm^2 is excluded because $\sin^2 2\theta_{ee}$ is a function of θ_{13}. However, around $\Delta m^2 \sim 10^{-3}$ eV^2, there still remains a

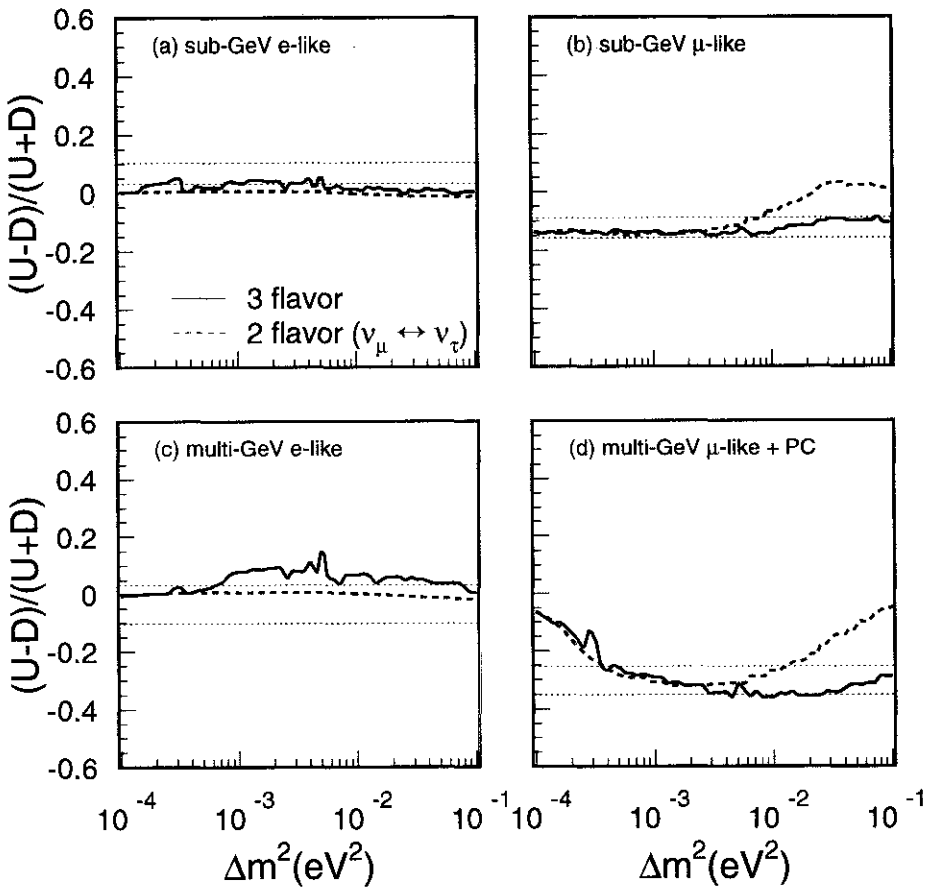

Figure 8.9: Expected sub-GeV (left) and multi-GeV (right) up-down asymmetry, (U-D)/(U+D), as a function of the mass square difference, Δm^2. Solid (dashed) lines show these in 3-flavor (2-flavor $\nu_\mu \leftrightarrow \nu_\tau$) oscillation. Expected values are taken at the χ^2 minimum point for each Δm^2 with the mixing angles unconstrained. The regions between two dotted lines show the measured up-down asymmetry value with statistical and systematic errors.

large allowed region in θ_{13}. Bugey [76] and Gösgen [77] experiments also exclude $\sin^2 2\theta_{ee} \gtrsim 0.05$ at $\Delta m^2 > 10^{-2}$ and $\Delta m^2 \gtrsim 10^{-2}$ at $\sin^2 2\theta_{ee} = 1$.

The exclude region on θ_{13} by CHOOZ can be applied to $\sin^2 2\theta_{\mu e}$ and $\sin^2 2\theta_{\mu\tau}$. According to the allowed region on $\sin^2\theta_{23}$ by 3-flavor oscillation analysis ($0.33 < \sin^2\theta_{23} < 0.87$, $0.45 < \sin^2 2\theta_{23} < 1$), the regions of

$$\begin{aligned} \sin^2 2\theta_{\mu e} &= \sin^2\theta_{23}\sin^2 2\theta_{13} < 0.87\sin^2 2\theta_{13}^{\mathrm{CHOOZ}} \\ \sin^2 2\theta_{\mu\tau} &= \cos^4\theta_{13}\sin^2 2\theta_{23} < 0.45\cos^4\theta_{13}^{\mathrm{CHOOZ}} \end{aligned}$$

are considered to be excluded at 90 % C.L. These exclude regions are shown in Fig 8.10 (c) and (d) and the regions of $\sin^2 2\theta_{\mu e} \gtrsim 0.17$ and $\sin^2 2\theta_{\mu\tau} \lesssim 0.4$ in the large Δm^2 region are excluded.

In near future, the long baseline experiment with ν_μ beam from accelerators, such as K2K [78] and MINOS [79], will start and search ν_μ disappearance and ν_e and ν_τ appearance. The explorable regions by K2K and MINOS are shown in Fig 8.10(b) (ν_μ disappearance), (c) (ν_e appearance) and (d) (ν_τ appearance). The regions to the right of the line will be expected to be sensitive by the appearance or disappearance methods. For $\nu_\mu \to \nu_\mu$ transition, K2K and MINOS cover the region of $\Delta m^2 \gtrsim 2\times 10^{-3}$ by ν_μ disappearance, and for $\nu_\mu \to \nu_e$ and $\nu_\mu \to \nu_\tau$ transitions, most of the allowed region will be expected to be explored by the future experiments.

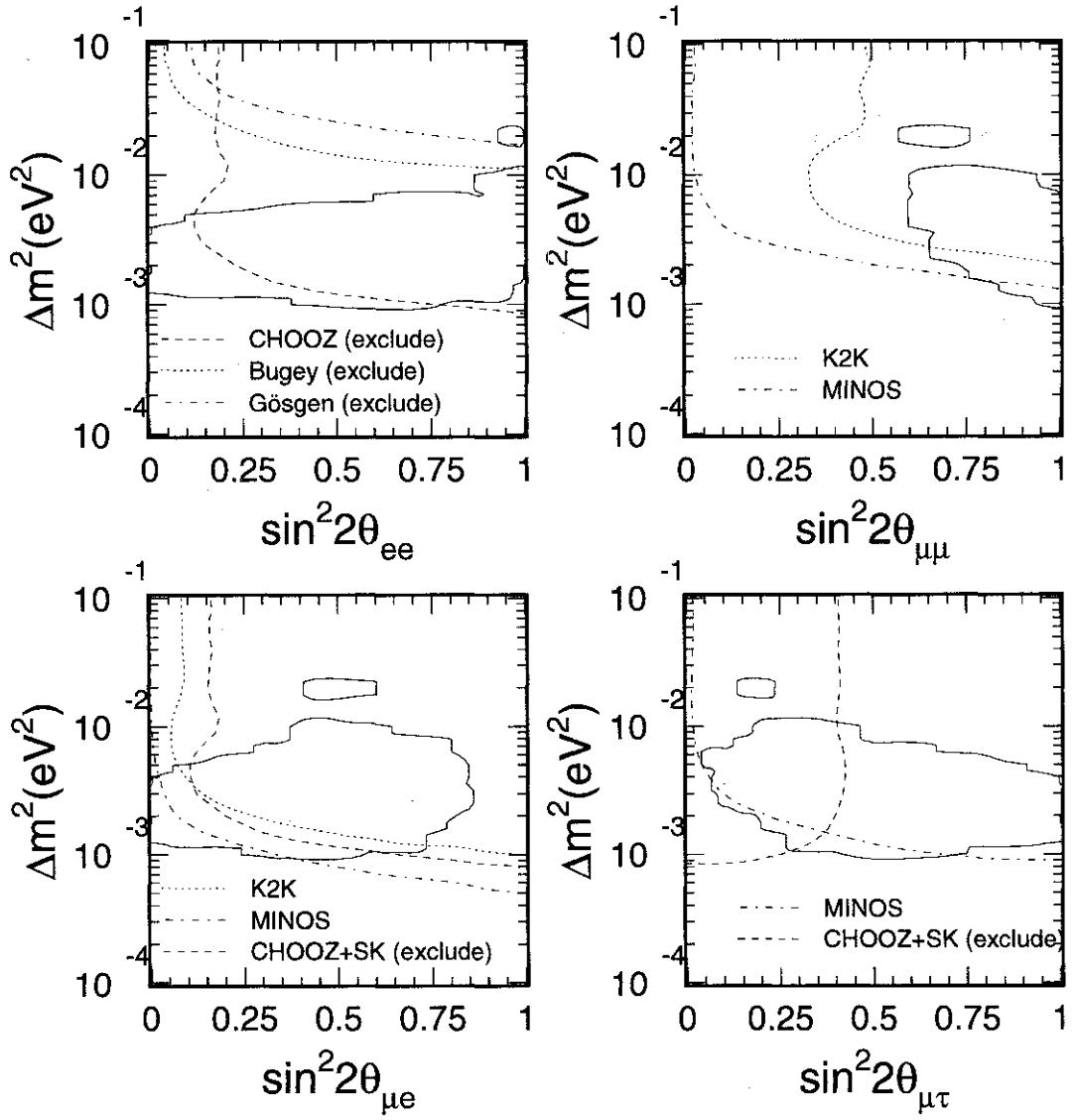

Figure 8.10: Allowed region for (a) $\nu_e \to \nu_e$, (b) $\nu_\mu \to \nu_\mu$, (c) $\nu_\mu \to \nu_e$ and (d) $\nu_\mu \to \nu_\tau$ transition, obtained by the atmospheric neutrino 3-flavor oscillation analysis. The regions inside of solid lines are allowed at the 90% C.L.. The excluded regions by CHOOZ ($\nu_e \to \nu_e$) and the sensitivity of the future neutrino experiments (K2K and MINOS) are also shown. The excluded region by CHOOZ+SK data in $\nu_\mu \to \nu_e$ and $\nu_\mu \to \nu_\tau$ are also shown.

Chapter 9

Conclusion

We have measured atmospheric neutrinos with the 33.0 ktonyr exposure of the Super-Kamiokande detector and obtained 4474 fully-contained (FC) events and 301 partially-contained (PC) events.

- The R, μ/e ratio compared to the Monte Carlo prediction, was measured to be

$$\begin{aligned} R &= 0.63 \pm 0.03\ (\text{stat.}) \pm 0.04\ (\text{syst.}) && (\text{sub-GeV}) \\ R_{FC+PC} &= 0.65 \pm 0.05\ (\text{stat.}) \pm 0.08\ (\text{syst.}) && (\text{multi-GeV}) \end{aligned}$$

  and significantly smaller than 1 for both sub-GeV and multi-GeV energy regions. No strong momentum dependence of R was observed.

- The significant deficit of the upward-going events was observed for FC μ-like and PC events. The up/down ratio for sub-GeV and multi-GeV μ-like events was found to be

$$\begin{aligned} U/D &= 0.78\ ^{+0.05}_{-0.05}\ (\text{stat.}) \pm 0.01\ (\text{syst.}) && (\text{sub-GeV } \mu\text{-like data}) \\ U/D &= 0.53\ ^{+0.06}_{-0.05}\ (\text{stat.}) \pm 0.01\ (\text{syst.}) && (\text{multi-GeV } \mu\text{-like data}) \end{aligned}$$

  where the unity was expected by the Monte Carlo prediction. The up/down ratio for e-like events was consistent with the expectation for both sub-GeV and multi-GeV.

- We have performed the 2-flavor oscillation analysis and the 3-flavor oscillation analysis with one mass scale dominance using the atmospheric neutrino data.

  From the 2-flavor $\nu_\mu \leftrightarrow \nu_\tau$ oscillation analysis, the best fit point was at $(\Delta m^2, \sin^2 2\theta) = (2.1 \times 10^{-3}\ \text{eV}^2, 0.97)$ and the region $8 \times 10^{-4} < \Delta m^2 < 6 \times 10^{-3}\ \text{eV}^2$ and $\sin^2 2\theta > 0.79$ was allowed at 90 % C.L..

From the 3-flavor oscillation analysis, the minimum χ^2 value was 65.7/66 d.o.f at (Δm^2, $\sin^2\theta_{23}$,$\sin^2\theta_{13}$) = (2.2×10^{-3} eV^2, 0.68, 0.20). The 90 % C.L. allowed Δm^2 region was $9\times10^{-4} < \Delta m^2 < 2.5\times10^{-2}$ eV^2. The 90 % allowed $\sin^2\theta_{23}$ region was $0.33 < \sin^2\theta_{23} < 0.87$. We found that the constraint on θ_{13} was relatively week ($\sin^2\theta_{13} < 0.75$ at 90 % C.L.) due to the MSW effect. Pure $\nu_\mu \leftrightarrow \nu_\tau$ oscillation (θ_{13}=0) was consistent with data within 90 % confidence level (C.L.). On the other hand, pure $\nu_\mu \leftrightarrow \nu_e$ oscillation ($\theta_{23}=\pi/2$) is excluded at more than 99.99 % C.L.. We conclude that the present data give evidence for oscillation of muon neutrinos.

Bibliography

[1] K.Hirata et al., Phys. Rev. Lett. **65** 1297 (1990);
K.Hirata et al., Phys. Rev. **D44** 2241 (1991)

[2] K.Hirata et al., Phys. Rev. Lett. **58** 1490 (1987);
K.Hirata et al., Phys. Rev. **D38** 448 (1988)

[3] S.Ahlen et al., Phys. Lett. **B357** 481 (1995)

[4] K.Hirata et al., Phys. Lett. **B205** 416 (1988);
K.Hirata et al., Phys. Lett. **B280** 146 (1992)

[5] Y.Fukuda et al., Phys. Lett. **B335** 237 (1994)

[6] R.Becker-Szendy et al., Phys. Rev. **D46** 3720 (1992);
D.Casper et al., Phys. Rev. Lett. **66** 2561 (1991);

[7] R.Clark et al., Phys. Rev. Lett. **79** 345 (1997)

[8] W.Allison et al., Phys. Lett. **B391** 491 (1997)

[9] K.Daum et al., Z. Phys. **C66** 417 (1995);
C.Berger et al., Phys. Lett. **B245** 305 (1990);
C.Berger et al., Phys. Lett. **B227** 489 (1989)

[10] M.Aglietta et al., Europhys. Lett. **8** 611 (1989)

[11] S.Kasuga et al., Phys. Lett. **B374** 238 (1996);
A.Sakai, Doctor thesis University of Tokyo (1996)

[12] O.G.Ryazaskaya, JETP Lett. **60** 617 (1994);
O.G.Ryazaskaya, JETP Lett. **61** 237 (1995)

[13] Y.Fukuda et al., Phys. Lett. **B388** 397 (1996)

[14] V.Barger et al., Phys. Rev. **D22** 2718 (1980)

[15] H.W.Zaglauer et al., Z. Phys. **C40** 273 (1988)

[16] L.Wolfenstein, Phys. Rev. **D17** 2369 (1978); **D20** 2634 (1979)

[17] S.P.Mikheyev and A.Yu.Smirnov, Yad. Fiz. **42** 1441 (1985)

[18] G.L.Fogli et al., Phys. Rev **D55** 4385 (1997)

[19] C.Giunti et al., hep-ph/9709439

[20] J.Pantaleone, Phys. Rev. **D49** R2152 (1994)

[21] H.Kume et al., Nucl. Instr. and Meth., **205**, 299 (1983)

[22] A.Suzuki et al., Nucl. Instr. and Meth., **A329** 299 (1993)

[23] C.McGrew PhD thesis, University of California at Irvine, 1994

[24] KEK Data Acquisition Development Working Group,
"TKO Specification", KEK Report 85-10 (1985)

[25] T.Tanimori, H.Ikeda, M.Mori, K.Kihara, H.Kitagawa and Y.Haren,
IEEE Trans. Nucl. Sci., bf NS-36, 497 (1989)

[26] Y.Kitaguchi, master thesis, Niigata Univ. (1997) (unpublished)

[27] P.Hüggi, R.D.Viollier, U.Raff and K.Alder, Phys. Lett. **51B** 119 (1974)

[28] M.Nakahata et al., accepted for publication in Nucl. Instr. and Meth. **A**

[29] M.Honda et al., Phys. Rev. **D52** 4985 (1995)

[30] M.Honda et al., Phys. Lett. **B248** 193 (1990)

[31] T.K.Gaisser, T.Stanev and G.Barr, Phys. Rev. **D38** 85 (1988)

[32] G.Barr, T.K.Gaisser and T.Stanev, Phys. Rev. **D39** 3532 (1989)

[33] E.V.Gugaev et al., Phys. Lett. **B232** 391 (1989)

[34] H.Lee and Y.Koh, Nuovo Cimento **B105** 884 (1998)

[35] M.Nakahata et al., J.Phys. Soc. Jpn. **55** 884 (1986)

[36] C.H.Llewellyn Smith, Phys. Rep. **3C** 261 (1972)

[37] K.L.Miller et al., Phys. Rev. **D26** 537 (1982)

[38] S.Hiramatsu et al., Proceedings of the Int. Conf. on Nuclear Structure Studies Using Electron Scattering and Photoreaction, Sendai, 1972, P429

[39] K. Furuno et al., to be submitted

[40] S.J.Barish et al., Phys. Rev. **D16** (1977) 3103

[41] S.Bonetti et al., Nuovo Cimento **A38** (1977) 260

[42] S.V.Belikov et al., Z. Phys. **A320** 625

[43] K.Abe et al., Phys. Rev. Lett. **56** (1986) 1107

[44] C.H.Albright et al., Phys. Rev. **D14** (1976) 1780

[45] D.Rein and L.M.Sehgal, Ann. of Phys. **133** (1981) 1780;
D.Rein, Z. Phys. **C35** (1987) 43

[46] H.Deden et al., Nucl. Phys. **B85** (1975) 269

[47] E.Oltman et al., Z. Phys. **C53** (1992) 51

[48] S.J.Barish et al., Phys. Rev. **D17** (1978) 1

[49] H.Sarikko *Neutrino 1979* (1979) 507

[50] S.J.Barish et al., Phys. Rev. **D19** (1979) 2521

[51] P.Musset and J.P.Vialle, Phys. Rep. **C39** (1978) 1

[52] J.E.Kim et al., Rev. Mod. Phys. **53** (1981) 211

[53] D.Rein and L.M.Sehgal, Nucl. Phys. **B223** (1983) 29

[54] H.Faissner et al., Phys. Lett. **B125** (1983) 230

[55] H.H.Grabosch Z. Phys. **C31** (1986) 203

[56] F.Bergsma Phys. Lett. **B157** (1985) 469

[57] S.Adler, Phys. Rev. **B135** (1964) 963;
C.Piketty and L.Stodolsky, Nucl. Phys. **B15** (1970) 571

[58] L.L.Salcedo and E.Oset et al., Nucl. Phys. **A484** (1998) 79

[59] G.Rowe et al., Phys. Rev **C18** (1978) 584

[60] D.Ashery et al., Phys. Rev. **C23** (1981) 2173

[61] C.H.Ingram et al.,Phys. Rev. **C27** (1983) 1578

[62] T.Fujii et al., Nucl. Phys. **B120** (1977) 395

[63] K.Ukai et al., INS-T-550 (1997)

[64] K.Baba et al., Nucl. Phys. **A306** (1978) 292

[65] J.Arends et al., Nucl. Phys. **A526** (1991) 479

[66] T.A.Gabriel et al., IEEE Trans. Nulc. Sci 36,1 (1989) 14

[67] K.Fujita, Master Thesis Tohoku University (1995)

[68] A.S.Carrol et al., Phys. Rev. **C14** (1976) 635

[69] E.Bracci et al., CERN/HERA 72-1 (1971)

[70] E.Eichler, JADE-Note 65 (1980)

[71] A.Morel et al., Limnology and Oceanography 22 (1977) 709

[72] S.Kasuga, Doctor thesis University of Tokyo (1998)

[73] T.K.Gaisser and T.Stanev, Phys. Rev. **D57** 1977 (1998)

[74] Dziewonski, and Anderson, Phys. Earth Planet. Inter., 25(1981)297

[75] M.Apollonio et al, Phys. Lett. **B420** 397 (1998)

[76] B.Achkar et al., Nucl. Phys. **B434** 503 (1995)

[77] G.Zacek et al., Phys. Rev. **D34** 2621 (1986)

[78] Y.Oyama et al, hep-ex/9803014 (1998)

[79] MINOS experiment, http://www.hep.anl.gov/NDK/HyperText/numi.html